

Mission and Science Instruments: Chandrayaan-1 perspective

By

**Arup Roy Chowdhury
SEG, SEDA, SAC**

Email: arc@sac.isro.gov.in

Mission and Science Instruments: Chandrayaan-1 perspective

Arup Roy Chowdhury
Instrument Scientist, Chandrayaan-1
Head SCPD/SEDA, Space Applications Centre
arc@sac.isro.gov.in

Introduction

Moon, our closest celestial body has aroused curiosity in our mind much more than any other objects in the sky. The most acceptable hypothesis on formation of Moon is the giant impact of a planetesimal, as large as Mars, with Earth that ejected enormous amount of material to form the Moon. Immediately afterwards Moon went through stages of partial melting which formed a magma ocean, solidification of crust, delayed impacts of large number of interplanetary bodies which created impact basins on crust and volcanism which resulted in filling of these basins.



There are thus two distinct features on Moon - dark lowland or maria and the brighter highlands or terrae. The highlands represents the ancient lunar crust. The mare region represents large basins formed by impact of very large objects and were later filled by magmas from deeper interior. Meteoroids, the largest being Copernicus and Tycho's (dia 85-90 Km) resulted in formation of lunar regolith, a layer of dust and rocky fragments 5-10m thick on level areas.

Interest on Moon

The Moon and Earth were formed within few million years, 4 billion years ago. Being connected with origin of Earth (giant impact theory) it holds the key to the understanding of the origin and early history of Earth.

The Moon is almost completely devoid of atmosphere, life and intrinsic magnetic field which means the surface is in direct contact with interplanetary medium (meteoroids, solar wind, solar and galactic cosmic rays). Thus Moon can serve as a monitor of the solar activity in direct vicinity of earth.

Moon has abundant resources of hydrogen (hence possibility of water), nitrogen, carbon, helium and other solar wind gases trapped in its regolith. Earlier studies showed that Moon has a relative abundance of Helium-3 compared to Earth. He-3 can be used as fusion element and thus considered as an important fuel for power generation in future.

The other interest is the possible presence of water-ice in permanently shadowed regions (craters in poles). The lunar ice is thought to have come from comets that collided with it. This raises the prospects of establishing self-sustaining lunar colony.

Also interest on study of Moon is for landing sites, space observatory and future colonization.

There are still gaps in the knowledge about Moon despite the popular belief that the Apollo and Luna missions of the 1960s and early 1970s had gathered all the information from Moon. There is a renewed interest internationally for the exploration of Moon.

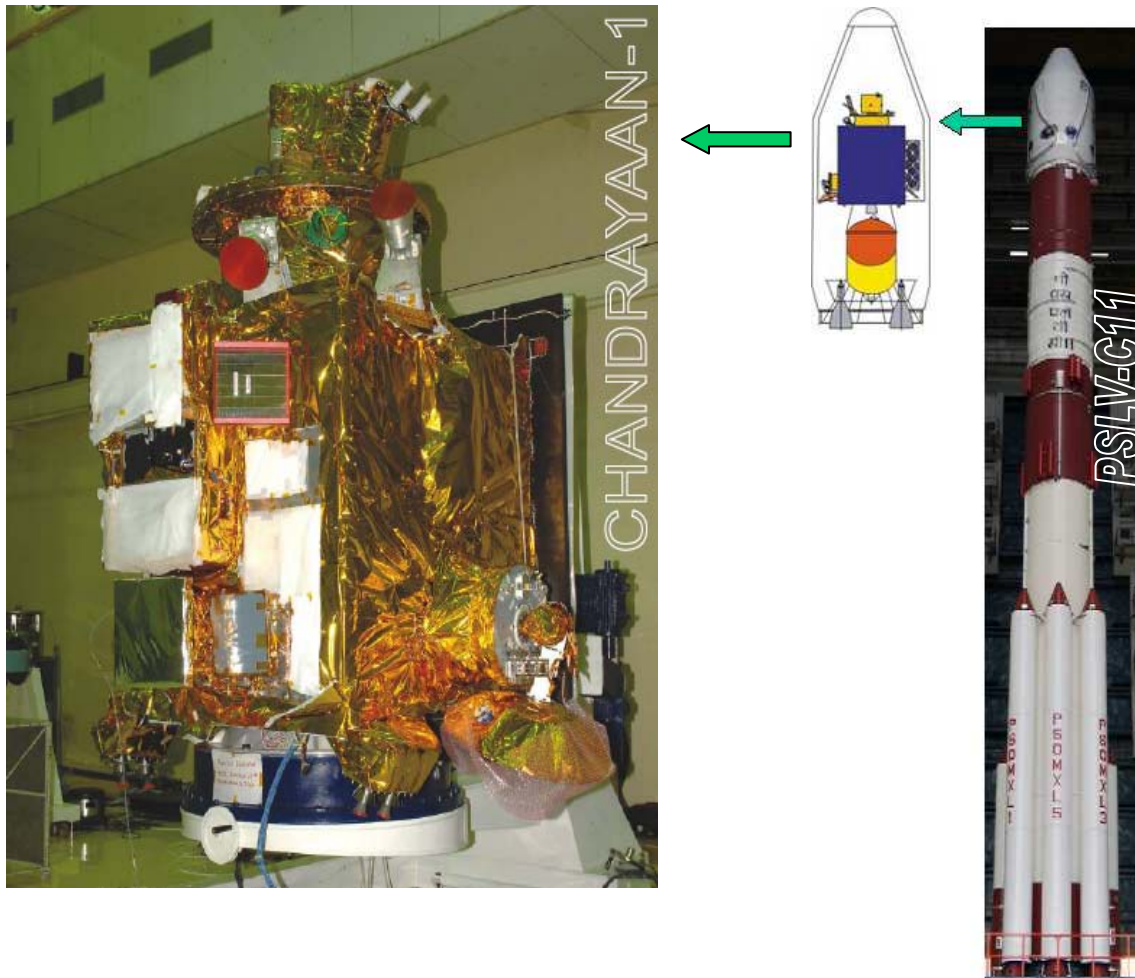
India decided to send a mission to Moon in view of the renewed international interest and considering that such a mission will provide the needed thrust to basic science and engineering research in the country. Thus Chandrayaan-1, which means 'Moon vehicle' in Sanskrit, thus became India's first planetary mission.

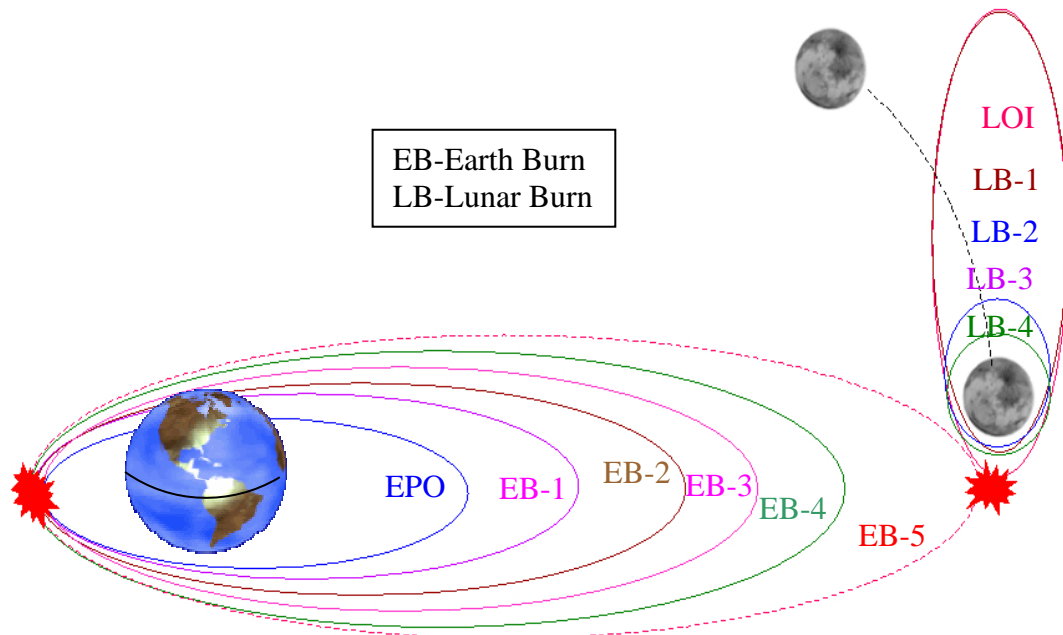
The primary objectives of Chandrayaan-1 are:

1. To expand scientific knowledge about the moon
2. To upgrade India's technological capability
3. To provide challenging opportunities for planetary research to the younger generation of Indian scientists

Chandrayaan-1

The Chandrayaan-1 is India's first instrumented mission to moon. The Spacecraft is cube shaped (approx 1.5m side), weighing 1380kg at launch, including propellant mass (820kg), and accommodating eleven science payloads. The PSLV-XL (PSLV-C11) rocket was used to inject the 1380 kg mass spacecraft into a 256 x 22866 km Elliptical Parking Orbit (EPO) on 22nd October 2008. The 440N liquid motor of the spacecraft was then used for injection into the Lunar Transfer Trajectory (LTT) and for Lunar Orbit Insertion (LOI). Chandrayaan-1 was finally placed in the 100km circular polar orbit around moon on 12th November 2008. On 14th November the Moon Impact Probe (MIP) was released from Chandrayaan to impact on Moon, it became the first Indian object to touch lunar surface.





Chandrayaan-1 : Spacecraft

- 3-axis stabilized, cube shaped (approx 1.5m side)

- 1380kg at launch, including propellant mass (820kg)

- Single-sided solar array, generates 700W of power

- During eclipse, powered by 36AH Li-Ion battery

- Recorder for payload data

- Transmission in X-band,

- 0.7m parabolic antenna with dual gimbal mechanism to track earth

- Star sensor & miniaturized gyros for attitude references

- Coarse Analog Sun Sensor for sun search/acquisition

- Accelerometers to estimate velocity change

- Telemetry, Tracking & Command (TTC) in S-band

- Passive thermal control systems

PSLV-C11 : The Launcher

44.4m, weighing 316 tonnes at lift off
4 stages, solid and liquid propulsion alternately
6 strap-on motors augment the first stage thrust

Chandrayaan-1 : Ground segment

The Ground Segment of Chandrayaan-1 performed the crucial task of receiving the signals sent by the spacecraft. It also transmitted the commands to be sent to the spacecraft during different phases of mission. Besides, it processes and safe keeps the scientific information sent by Chandrayaan-1. The Ground Segment of Chandrayaan-1 consists of:

- Indian Deep Space Network (IDSN), the communication link with Chandrayaan
- Spacecraft Control Centre (SCC), responsible for all spacecraft operations
- Indian Space Science Data Centre (ISSDC), initial payload data processing and custodian of science data

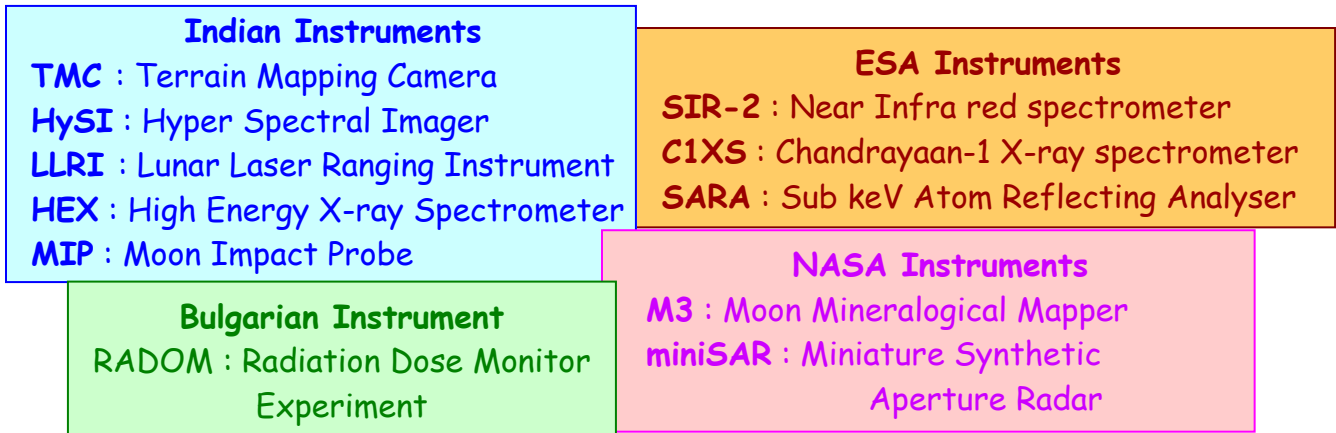
IDSN consists of two large parabolic antennas, one with 18 m and the other 32 m diameter.



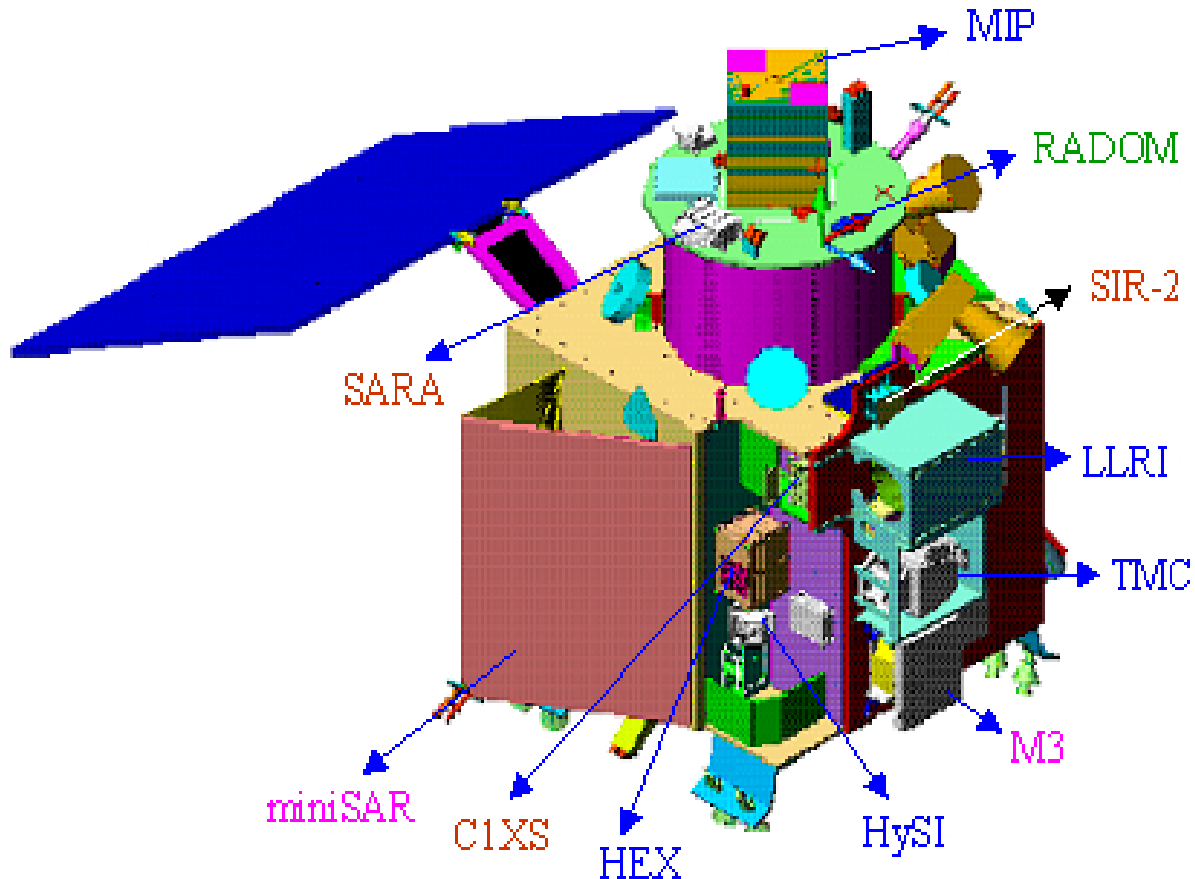
Chandrayaan-1 : Payloads

Chandrayaan-1 carried 11 science payloads to meet the science objective of the mission.

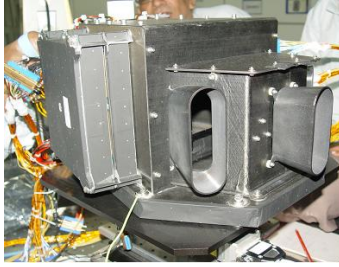
- ❖ Five of these are indigenous ISRO payloads
- ❖ Six are from International communities, in response to ISRO's Announcement of Opportunity (AO). Two of these has ISRO's collaboration.



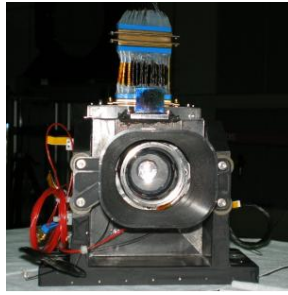
Payload placement on Chandrayaan-1



Chandrayaan-1 : Payload details



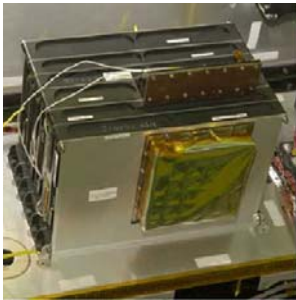
TMC : Stereoscopic camera for Topographic mapping with high spatial and altitude sampling.



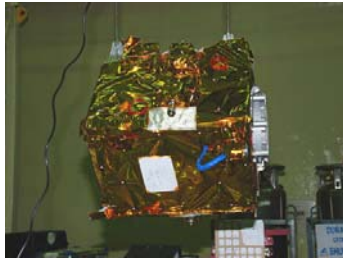
HySI : Imager for Mineralogical mapping in large number of bands with high spectral resolution in visible and near infra-red band.



LLRI : Laser altimeter with altitude resolution of < 10m. Slope information in addition to range information.



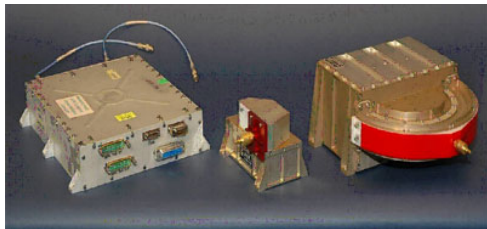
HEX : Spectral study in X-ray region of 10keV to 270keV with spatial resolution of 33km.



MIP : impacted on Moon at the start of the mission. The impactor has three instruments viz. Moon Imaging system, Radar altimeter and Mass spectrometer.



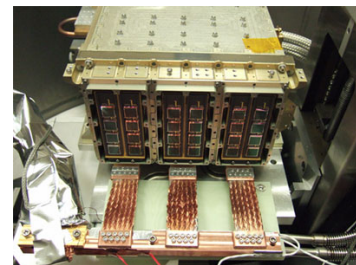
RADOM : characterise the radiation environment in near lunar space.



SARA : Moon imaging using low energy neutral atoms as diagnostics in the energy range 10eV to 3.2keV for studying interaction of solar wind on lunar surface



SIR2 : NIR point spectrometer for determination of the chemical composition of crust and mantle



C1XS : X-ray spectroscopy, 1keV to 10keV. C1XS also includes an X-ray Solar Monitor 1-20 keV.



M3 : Imaging spectrometer, operating upto μm range for measuring solar reflected energy.



Mini-SAR : Radar system can operate as an altimeter / scatterometer, radiometer, and as a synthetic aperture radar imager.

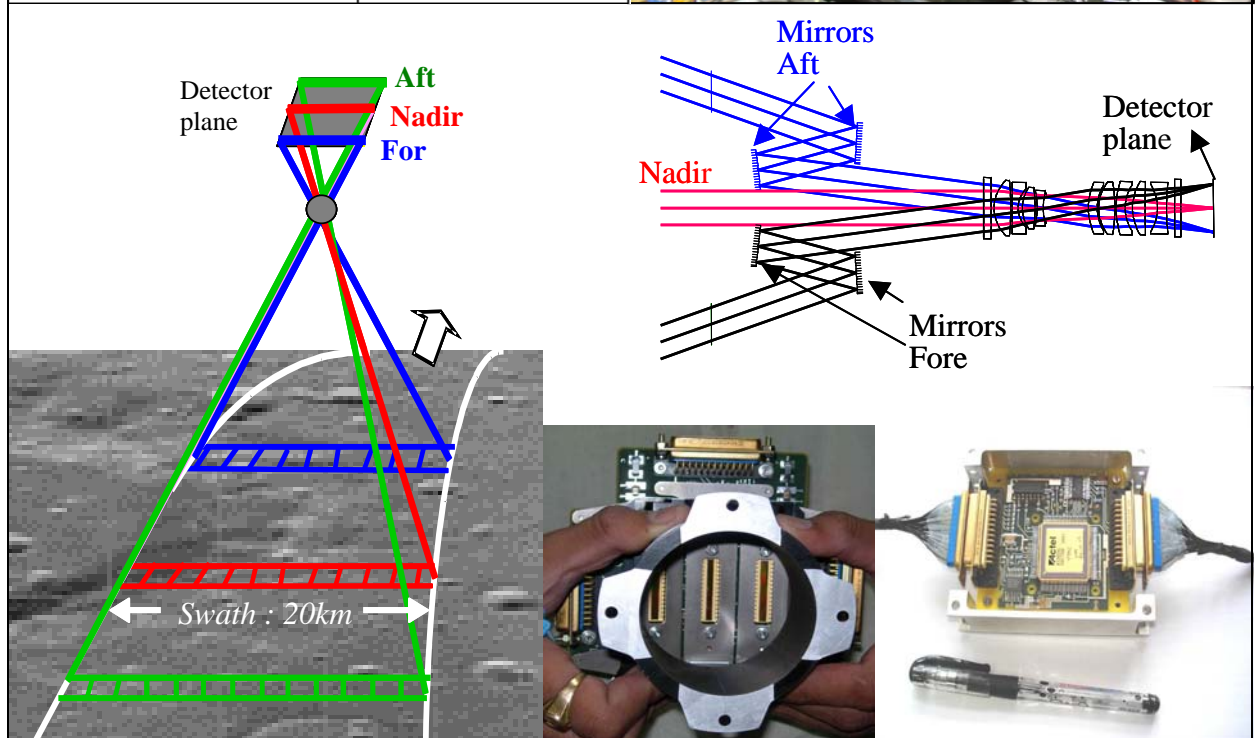
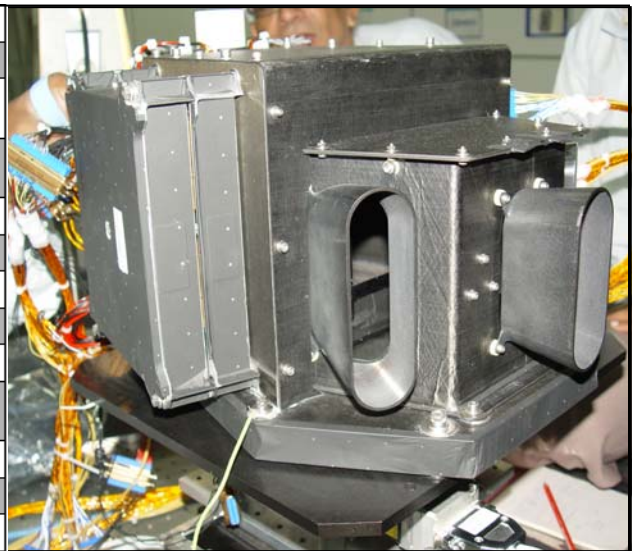
TMC and HySI instruments

Terrain Mapping Camera (TMC) and Hyper Spectral Imager (HySI) are the two Indian Imaging payloads for Chandrayaan-1 which were developed at Space Applications Centre.

The TMC instrument is intended for the topographic mapping of the complete moon. It is a panchromatic camera with stereoscopic imaging in fore, nadir and aft directions of the spacecraft movement. Such high sampled map of entire lunar surface is available for the first time and will help in better understanding of the evolution process and detailed study of regions of scientific interests.

Terrain Mapping Camera

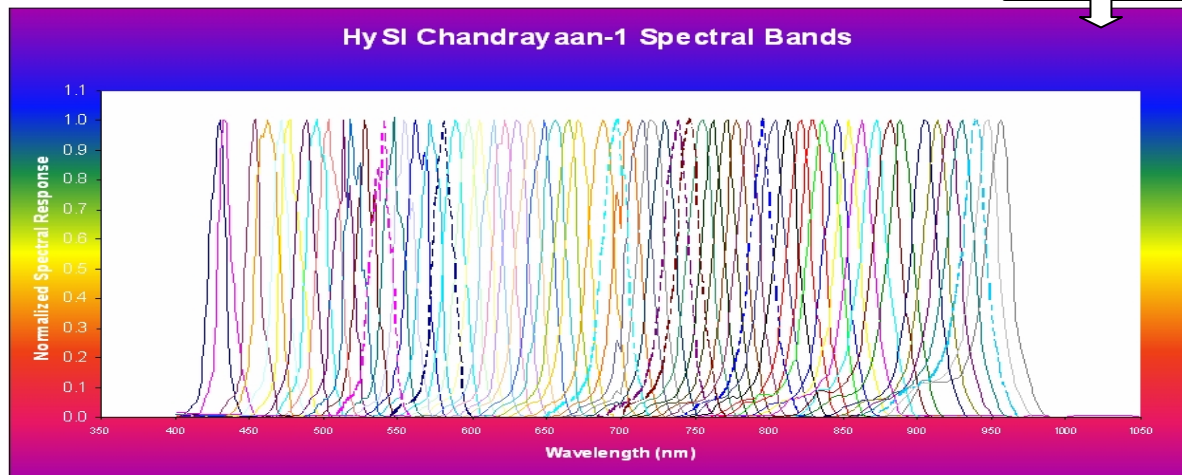
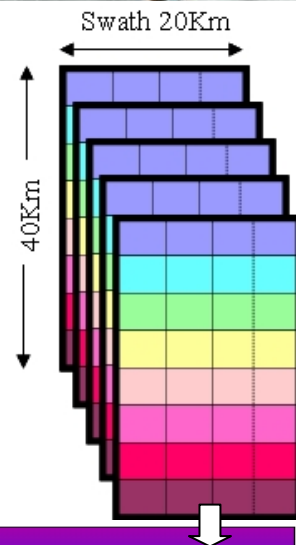
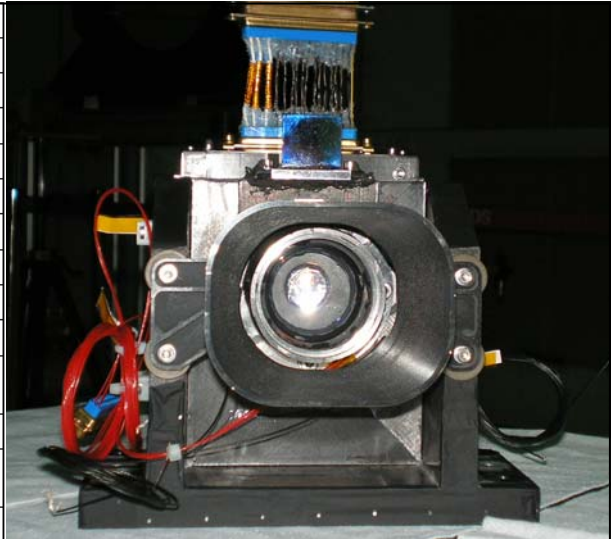
Spatial Sampling	5m x 5m (@ 100km)
Swath	20km
Spectral band	Panchromatic band, 0.5-0.75 μm
Stereo imaging	Along track Triplet (Fore, Nadir, Aft)
Radiometric Levels	4096
No. of gains / exposure settings	4 each
Data rate / view (Mbps)	16.286 (serial)
Operating temperature ($^{\circ}\text{C}$)	20 ± 10
MTF (%)	> 15
SNR @ 1.2 mW/cm ² /sr/ μm	> 80
@ 14 mW/cm ² /sr/ μm	> 300
Weight (Kg)	6.3
Dimension (mm ³)	450*255*362 (Y*P*R)
Regulated Power (W)	1.8



The HySI instrument imaged the lunar surface in 64 bands in the VNIR spectral range with 12-bit quantization. The data available is 80m spatial sampled with 20km swath coverage from 100km altitude. The high sampled spatial and spectral data from the instrument will help in improving the available information on mineral composition of moon.

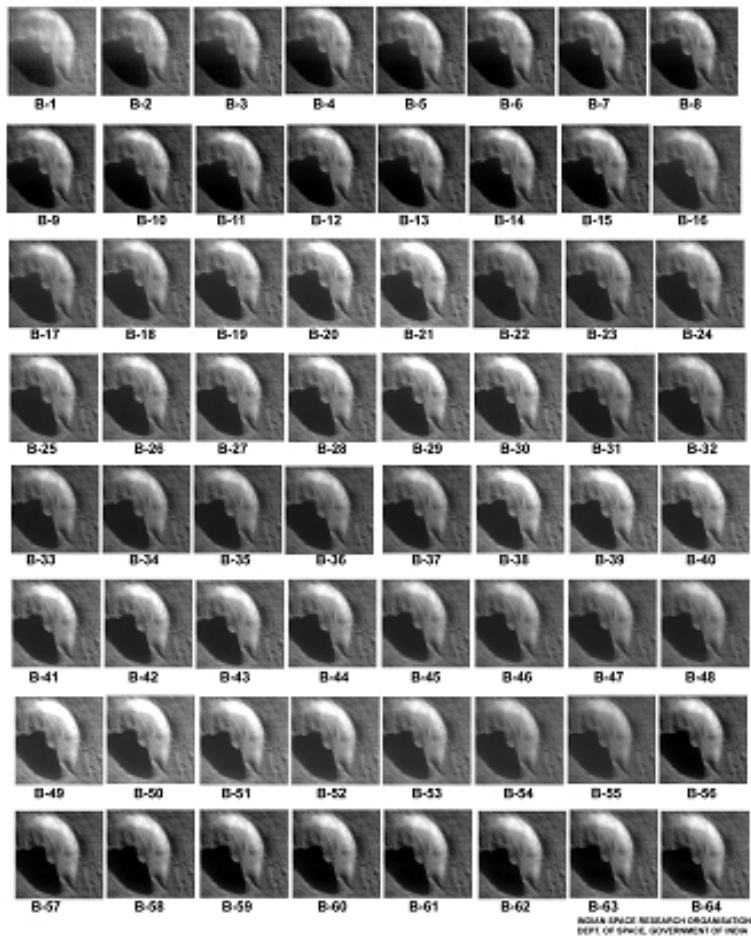
Hyper Spectral Imager

Spatial Sampling	80m x 80m (@ 100Km)
Swath	20km
Spectral range	421-964 nm
No. of bands	64 contiguous
BW (nm)	between 12.3 to 20.5
Sampling interval (nm)	8.3
Radiometric levels	4096
Gains / exposure settings	2 / 4 nos.
Operating temperature (°C)	20 ± 10
MTF (%)	> 20
SNR @ 0.8 mW/cm ² /sr/µm @ count 4000	>100 >1000
Weight (Kg)	2.5
Dimension(mm ³) EOM Electronics	178x163x194 (RxPxY) 172x192x65
Regulated Power (W)	0.8





Craterlet Barrow-H : HySI



**Photogrammetric Modeling & Data
Processing: Chandrayaan-1
Perspective (for Linear CCD Imaging
Sensors)**

By

**B. G. Krishna
GD, SPDCG, SIPA, SAC**

Email: [bgk@ sac.isro.gov.in](mailto:bgk@sac.isro.gov.in)

Photogrammetric Modeling & Data Processing: Chandrayaan-1 perspective (for Linear CCD Imaging Sensors)

B Gopala Krishna, Sanjay Singh, T P Srinivasan

SPDCG/SIPA

Space Applications Centre

Ahmedabad

1.0 Introduction

Photogrammetric modeling is an important aspect for any planetary mission dealing with mapping of the planetary surfaces with respect to topography using imaging sensors. This basically includes the derivation of precise relationship between the (obtained) image and the planet surface (ground) and the derivation of topography. These models further help in correcting/mapping this imagery on to the surface (like orthoimage generation) after eliminating various distortions due to camera tilt, planet rotation, curvature, satellite motion, surface relief etc. The basic inputs required for sensor modeling are sensor parameters, mission parameters, satellite ephemeris and other ancillary data. Control points (if available) further improves the model parameters making the relationship (image to ground/ground to image) more precise. This needs an appropriate mathematical formulation to update the model. In the planetary data processing the ancillary data including the ephemeris are generally represented in the form of SPICE kernels [12]. This tutorial addresses the Photogrammetry model and data processing aspects of Chandrayaan-1 [1, 2, 3] CCD line scanner imaging sensors Terrain Mapping Camera (TMC) and Hyper Spectral Imager (HySI).

2.0 Photogrammetric Model

As indicated in the previous section, a major task in correction of line-scanner imagery (in the case of Chandrayaan-1) is to establish a relation between image and object space (lunar surface). There are various ways to achieve this. Rigorous Imaging model based on photogrammetric collinearity condition has been adopted for Chandrayaan-1 to establish the view direction.

2.1 Collinearity condition

The relationship between image and corresponding object space coordinates is established through physical imaging model in the form of collinearity condition. It states that the perspective centre, image point and the corresponding object space point all lie in a straight line.

Mathematically it can be stated as

$$\begin{pmatrix} x \\ y \\ z \end{pmatrix} = s * M * \begin{pmatrix} XA - XS \\ YA - YS \\ ZA - ZS \end{pmatrix} \dots\dots\dots(1)$$

where,

(x,y,z) are image focal plane coordinates of an image point,

s is a scale factor,

M is the transformation (rotation) matrix between object and image space

(XA,YA, ZA) are selenocentric coordinates of a ground point,

(XS,YS, ZS) are selenocentric coordinates of the perspective center

3.0 Coordinate Systems

In order to establish a precise relation between any two coordinate systems, it is first necessary to consider and list all the coordinate systems in use. The definitions and conventions for each of the above coordinate system are strictly adopted specific to Chandrayaan-1 convention. The following standard coordinate systems are used to carry out the required transformation in the imaging model. The same concept can be extended to any other planetary body.

3.1.1 Inertial coordinate system (LCI, Lunar Centric Inertial system or selenocentric): This is a lunar centered system with moon’s center as origin. This system is parallel to geocentric inertial coordinate system whose x-axis is towards vernal equinox of date (epoch 2000), Y-axis perpendicular to x-axis in the earth’s equatorial plane and the third axis completes the right-handed triad (earth’s rotation axis)

3.1.2 Lunar Centered Lunar Fixed (Selenographic) system: For LCLF, moon’s center is the origin; X-axis is taken in the Moon’s equatorial plane pointing towards the Moon’s prime meridian which is chosen so that it is on an average directed towards the center of the Earth’s disc. Y-axis is perpendicular to X-axis in the equatorial plane of Moon. While the third Z-axis is directed towards the lunar axis of rotation and completes the right-handed triad. The two angles (Figure-1) necessary to define the position vector in selenographic coordinate system are defined as follows. ϕ_m (Selenographic Latitude) is the acute angle measured normal to the Moon’s equator between the equator and a line connecting the geometrical center of the coordinate system with a point on the surface of the Moon. λ_m (Selenographic Longitude) is the angle measured towards the West, in the Moon’s equatorial plane, from the lunar prime meridian to the object’s meridian.

3.1.3 Orbital Coordinate system: The definition is as follows. At any instant of time, spacecraft x-axis towards moon center(yaw), z is along –

ve orbit normal perpendicular to x-axis in the orbital plane and the third one ,y-axis is perpendicular to both x and z.
 X direction $-\mathbf{r}/|\mathbf{r}|$, Z direction $-\mathbf{r} \times \mathbf{v}/|\mathbf{r} \times \mathbf{v}|$ and y is cross product of X and Z.

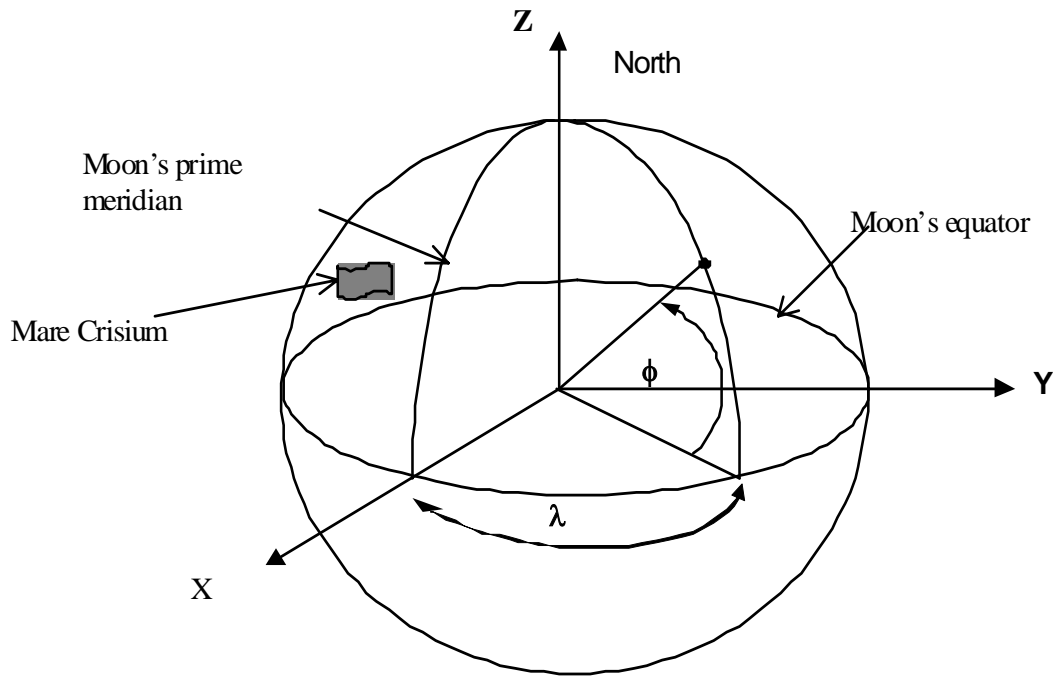


Figure-1 Selenographic Coordinate System

3.1.4 Body Coordinate system: Body coordinate system is nothing but orientation of orbital coordinate system for a given pitch, roll and yaw angles. This coincides with orbital coordinate system in the absence of roll, pitch and yaw angles (i.e all of them are zero).

3.1.5 Image Plane coordinate system (image space): This is the focal plane coordinate system where f (focal length) is in the direction of positive yaw x-direction, z is along the detector array and y is perpendicular to the array.

3.2 Estimation of image coordinates from ground coordinates

The sequence of transformations, which are considered for computing the image coordinates using ground coordinates as the input are as follows:

- Given Latitude, Longitude and Height of a lunar point, it is first converted to Cartesian (Selenographic system) coordinate system.
- Transformation of Selenographic coordinates to Selenocentric coordinates (using the liberation angles from JPL ephemerides)

- c) Selenocentric coordinates are transformed to Orbital Frame of reference using State Vectors.
- d) Transformation of Orbital system coordinates to Body Frame coordinate system using the attitude (orbit to body)
- e) Body Frame coordinate system to Sensor (imaging payload) using the spacecraft mounting angles and alignment angles.
- f) Sensor Frame (imaging payload) to image plane or Focal plane coordinate system using the payload geometry of TMC or HySI.
- g) Focal plane coordinate system to image coordinate system (scanline, pixel).

Transformation matrix M consists of four rotation matrices:

$$M = RL * RA * RO * R_{Lib}, \text{ where}$$

R_{Lib} is the rotation matrix for transformation from selenocentric coordinate system to selenographic coordinate system. These two coordinate systems are oriented by the Euler angles Ω' , i_s and Λ relative to each other as shown in Figure 2 [13].

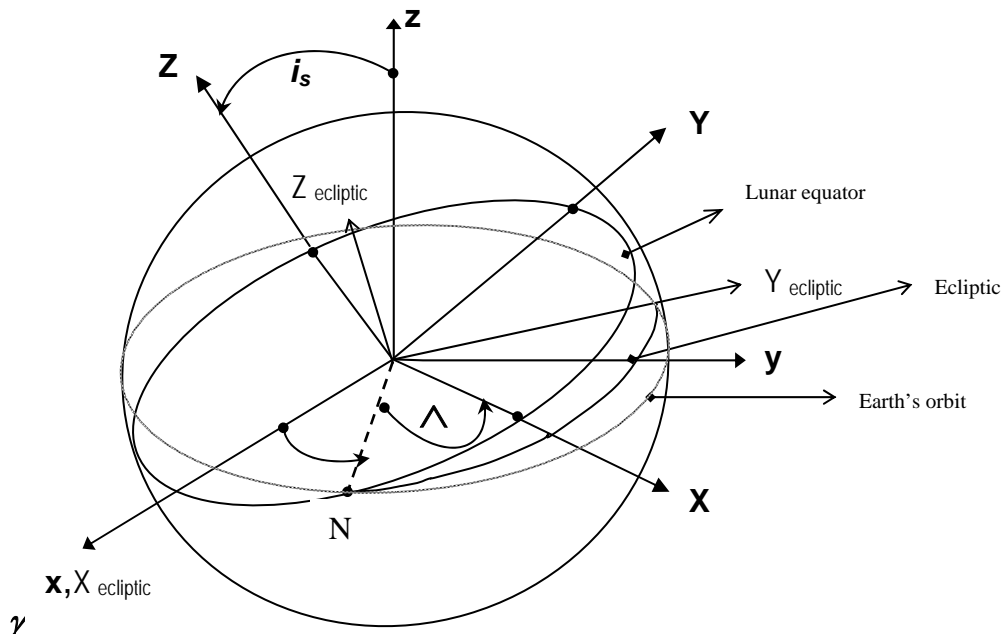


Figure-2 Selenocentric and Selenographic Coordinate Systems

Therefore, R_{Lib} , can be further decomposed into three matrices.

$$R_{Lib} = R_z(\Lambda) R_x(i_s) R_z(\Omega')$$

Determination of Euler angles Ω' , i_s and Λ involves Moon's mean orbit, because of the relationship between Moon's mean position and the orientation of lunar selenographic coordinates.

Above figure shows ecliptic plane ($X_{\text{ecliptic}} - Y_{\text{ecliptic}}$) which passes through the center of the moon. The lunar equator and orbit planes are shown intersecting in a line on the ecliptic plane. The x_m axis is shown in the lunar equator. In this Moon relative coordinate frame, the Earth is considered as orbiting the Moon (origin) in exactly the same orbit as the Moon orbits the Earth except that longitude angles measured in the orbit plane must be reduced by 180° . For example, when the Earth is at the descending node and the x_m axis points towards N (Figure-2) the Moon is in reality, at its ascending node, 180° advanced from N. Therefore the longitude of the ascending node Ω and the mean longitude λ must be reduced by 180° when used in the Moon relative frame.

The selenographic axes can be oriented to the selenocentric axes by means of the following four angles: -

1. ' ξ ' the true obliquity
2. ' $\Omega-180^\circ$ ' the longitude of the descending node
3. 'I' the inclination of the lunar equator to the ecliptic
4. ' θ ' the angle measured in the lunar equator between the descending node and the Moon's prime meridian.

Where the Euler angles Ω' , i_s and Λ are determined as functions of the orbital parameters ξ , Ω , I and θ by equating elements of the R_{Lib} and $R_{\text{Lib}'}$ matrices.

$$R'_{\text{Lib}} = R_z(\theta)R_x(I)R_z(\Omega - \pi)R_x(\xi)$$

RL is look angle rotation matrix transformation from spacecraft body coordinate system to image coordinate system; RL can be further decomposed as:

$RL = R_{po} * R_{mp}$, where

'**Rmp**' transforms coordinates from Master Reference Cube (MRC) to Payload Cube (PLC) and '**Rpo**' transforms coordinates from Payload cube to optical axis.

RA is attitude rotation matrix transformation from orbital coordinate system to spacecraft body coordinate system & it is given as a product of three rotations Rpitch, Rroll and Ryaw.

Therefore,

$$RA = R_{yaw} * R_{roll} * R_{pitch}$$

RA matrix is filled by using Orbit to Body quaternions in True of Date reference system

RO is orbit rotation matrix transformation from selenocentric coordinate system to orbital coordinate system.

Estimation of ground coordinates from image coordinates process is exactly reverse of the above described computation process of image coordinates from ground coordinates. This is directly using the collinearity equations. As such, this is the solution of the look vector intersecting the lunar surface (ellipsoid).

4 Space Resection

Though the above described model satisfy the image-ground; ground-image relation, its accuracy depends on the exterior orientation, which may be poorer in many cases. Space Resection is the process in which the orientation parameters are refined using a set of lunar control points (LCP). The updated orientation parameters are used for further data processing.

The model is based on the collinearity equation and the error in attitude is assumed to be systematic and follows certain polynomial behaviour. Depending on the imaging condition, this systematic error can follow a higher order polynomial behaviour (e.g 2nd order or higher). However, the choice of higher order polynomial requires more number of control points as the number of unknowns will be more. The polynomial coefficients are treated as unknown and thus, are estimated using the lunar control points. A simultaneous least square adjustment is used to determine the most probable solution for the unknowns. The same way orbital parameters can also be estimated using the space resection approach.

5 Rational Polynomial Coefficients (RPC)

The rigorous sensor model of an image is used for transformation between the 3D object space and the 2D image space. It includes the physical parameters about the camera, such as focal length, principal point location, pixel size, lens distortions, and orientation parameters of the image such as position and attitude. The Rational Function Model (RFM) is a general version of the polynomial model that can describe more complex ground-to-image transformations, which is generic in nature. It is otherwise called Rational Polynomial Coefficients (RPC) model that is used as an alternative solution for the physical sensor model and it is widely used whenever complex sensor model is not available. The RPC model forms the coordinates of the image point as ratios of the third degree polynomials in the

co-ordinates of the world or object space or ground point. A set of images is given to determine the set of polynomial coefficients in the RPC model to minimise the error. The least square solution is used to estimate the RPC [14, 15].

6 DEM Generation

To carry out DEM generation from a stereo pair or triplet imagery, space resection will be carried out first, simultaneously taking any two images at a time out of three images of TMC using some control points taken from ULCN (Unified Lunar Control Network) or from Clementine reference. After space resection wherein orientation parameters are updated, traditional space intersection process will be used to generate the DEM (or compute the 3D coordinates) at the conjugate points (mass points) generated through image matching process between FORE, AFT and NADIR imagery. Once the 3D locations of image points have been determined, the 3D points are interpolated using a triangle mesh interpolation. This mesh is then sampled at regular intervals in latitude and longitude. Vertical datum is based on spherical figure of the Moon and a lunar radius of 1737400 m. All elevations thus generated are in meters and represent the true values as the input ULCN points. These calculations are performed under the IAU 2000 Cartesian coordinate. Alternatively, Bundle Adjustment technique can also be considered for DEM generation taking all the three images of TMC simultaneously.

7 Datum and Map projection

7.1 Moon Shape Parameters (Moon Ellipsoid or sphere and datum)

The general shape of the Moon is very nearly a perfect sphere, excluding local topography variations. In fact, the magnitude of the local topography variations is much larger than the overall flattening of the lunar poles or any ellipticity of the lunar equator. IAU/IAG 2000 report recommends using the same radius value for both the lunar equator and the lunar pole (i.e. a sphere). The lunar topography data are expressed relative to a sphere with the same radius as recommended by the IAU/IAG 2000 report. The values in the IAU/IAG 2000 report are listed below.

[Note: The radius recommended here is different than the reference radius for the LP150Q gravity field].

RMoon-Equator = 1737.4 km (Radius of Moon equator from IAU/IAG)
RMoon-Pole = 1737.4 km (Radius of Moon pole from IAU/IAG)
fMoon = 0.0 (Moon flattening factor, derived from IAU/IAG values
((RMoon-Equator - RMoon-Pole)/ RMoon-Equator))

Therefore, an average radius (1737.4 km) datum shall be used for referencing topography data.

7.2 Map Projections

Simple cylindrical map projections are generally used for planetary mapping in addition to conic projections in middle and higher latitudes.

The projections used on most published planetary and satellite map series of the USGS are combinations or variations of Polar Stereographic, Lambert Conformal Conic, and Mercator projections. 1:1 Million - scale maps and beyond were usually compiled on a Transverse Mercator projection. But there were no fixed criteria for choosing a projection related to scale. A small number of special-purpose maps have been prepared on the Lambert Azimuthal Equal-Area and the Oblique Stereographic projections. Maps published by the DMA have used similar projections in addition to gnomonic and orthographic projections. Use of the Mercator projection in equatorial sheets and the Lambert Conformal Conic in middle and higher latitudes is also followed. Polar coverage is usually portrayed through use of a Polar Stereographic Projection between 80°-90° north and south latitudes.

Map Projections chosen for Chandrayaan-1 TMC/HYSI payload data correction and mapping are also in the similar lines discussed above. The map projections considered are,

1. Mercator (general choice)
2. Transverse Mercator (equatorial and middle latitude regions)
3. Polar stereographic (polar regions)

8 Data Processing

With the development of the imaging model, a standard approach is followed for data processing to generate the radiometrically and geometrically corrected data product. First the mappings from locations on object space (lunar surface or also called as output space) to locations in a satellite image (input image space) covering that area fully/partially is carried out and this is stored as a grid file. This file is then used along with the raw data for resampling to generate a geometrically corrected image. Alternatively the same task (product generation) can be done using RPCs along with the COTS package.

The regular Level-1 products (radiometrically corrected with only geometric tagging, no correction done) are generated through a software system (developed at SAC) in an automated mode pipeline [8] setup at Indian Space Science Data Center (ISSDC). The procedures are similar for TMC and HySI,

except that HySI will have an additional processing element of band to band registration. The products will be in a strip mode (as acquired in each pass) provided in Planetary Data System (PDS) standard as defined in [9,10]. Higher level products like DEM and Lunar Atlas [5, 6] are planned to be generated at identified Payload Operations Centres (POC). SAC is identified as POC for TMC and HySI.

There are some photogrammetric guest facilities available in USGS for working and analysing the planetary data for the research [11] purpose.

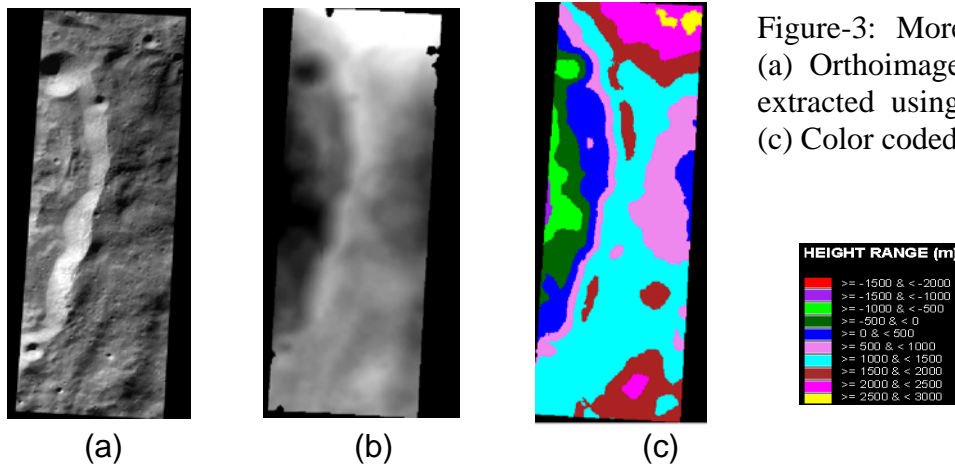
8.0 PDS and Data Archival

The science data obtained from the instruments onboard Chandrayaan-1 is being archived at ISSDC for dissemination and use by the scientific community in India and abroad after the lock-in and peer review process. The data from Chandrayaan-1 instruments is formatted and archived in such a way (in the form of long term archive) that they are easily accessible by Internet through simple interfaces being used elsewhere for similar kind of missions. NASA’s Planetary Data System (PDS) [7,9] is the de facto standard for archival of long term archival of planetary science data.

9.0 Some results of higher level processing [4,5]

10.0 As there are three images possible from TMC with different view angles, there are four possibilities of stereo image processing for the DEM generation. The combinations are Fore - Aft, Fore-Nadir, Aft – Nadir and Fore-Aft-Nadir images as a pair. Out of many cases, as an example, an area in the South Polar Region acquired on 15-11-2008 is given here for DEM generation. The region is a part of the crater Moretus with location -70.6 deg lat and -1.4 deg long. The DEM generated from two views are shown in figure-3. From the study it was observed that due to the relatively large angles between FORE and AFT the image matching was poor, however usage of points from all the images lead to a better DEM accuracy than usage of any of the two imagery. A color coding of the DEM is shown in figure-3c, which clearly shows the height range of the crater from -1500m to 4000 m with respect to the mean radial surface of the moon. This particular exercise is carried out by generation of RPCs through indigenous software and matching & DEM generation carried through a COTS package.

A large strip of 1800 km (location: Coulomb C crater) has been divided into 3 individual strips of 600 km and DEMs have been derived for all three strips separately. This break up is done to reduce the processing time in DEM generation. The DEMs and their visualisations are shown in figures-4, 5 and 6.



11.0 References

1. A quest for moon, Narendra Bhandari, Current Science, Vol. 83, No.4, 25 August 2002
2. Scientific Challenges of Chandrayaan-1:The Indian Lunar polar orbiter mission, Narendra Bhandari, Vol. 86, No. 11, 10 June 2004
3. ISRO page: <http://www.isro.gov.in>
4. Exploring the moon in three dimensions, P K Srivastava, B Gopala Krishna and Amitabh, Coordinates, Volume 5, Issue 4, April, 2009, pp. 6-9
5. Digital Elevation Models of The Lunar Surface from Chandrayaan-1 Terrain Mapping Camera (TMC) Imagery – Initial Results, B. Gopala Krishna, Amitabh, Sanjay Singh, P. K. Srivastava and A. S. Kiran Kumar, Lunar and Planetary Science XXXX (2009)
6. Data Processing and Product generation for Chandrayaan-1 TMC and HySI Payloads, B Gopala Krishna, SAC Courier, Vol. 23, No.1, House Journal of Space Applications Centre, January 2009, pp. 9-12
7. Data Archival & Dissemination System for Chandrayaan-1, Navita Thakkar, Ajay Kumar Prashar and B Gopala Krishna, to be presented in GEOMATICS 2010.
8. Data Processing System, Quick Look Display and Browse for Chandrayaan-1, Devakanth Naidu, K Suresh, Navita Thakkar, Kannan V Iyer, Bhaskara Rao, Sanjay Singh, Medha Alurkar, Ajay Kumar Prashar, T P Srinivasan, Jignesh Bhatt, B Gopala Krishna, to be presented in GEOMATICS 2010.
9. Planetary Data Standards for Archival and Dissemination, S.Manthira Moorthi and B. Gopala Krishna, to be presented in GEOMATICS 2010

10. Chandrayaan-1 Archive Plan, Jagjeet Singh Nain, B Gopala Krishna, Detlief, Chandrasekhar, CH1-SAC-PL-001, Issue. 1, Rev. b, 10 Feb 2008
11. Build your own Topographic Model: A Photogrammetry Guest Facility for Planetary Researchers, R.L. Kirk, E. Howington-Kraus, and M.R. Rosiek, Lunar and Planetary Science XXXX (2009)
12. http://isis.astrogeology.usgs.gov/Isis2/isis-bin//naif_spice.cgi?isis_moc_kernels.html
13. Coordinate Systems for Lunar Mission, Krishna, A., Gopinath, N., 2001, FDD/MDG/CMA/ISAC
14. A comprehensive study of the rational function model for photogrammetric processing. Tao, C.V. and Hu, Y., Photogrammetric Engineering & Remote Sensing, 67(12):1347-1357, 2001.
15. Rational Polynomial Modeling for Cartosat-1 Data, Sanjay K Singh, S Devakanth Naidu, T P Srinivasan, B Gopala Krishna, P K Srivastava, ISPRS Beijing Congress Proceedings, Jul 3-11, 2008, Vol. XXXVII, Part B1, TC-I, pp 885-888.

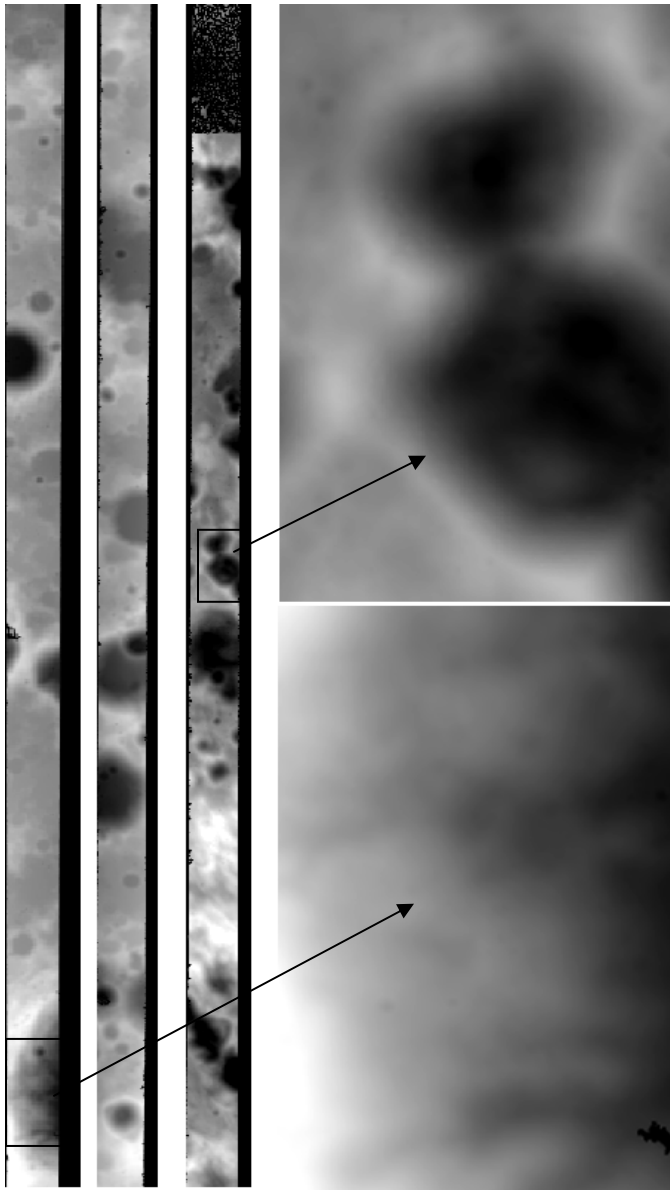


Figure-4: Overview & Full resolution (in box) of DEM generated for three strips of 600 km each [4]

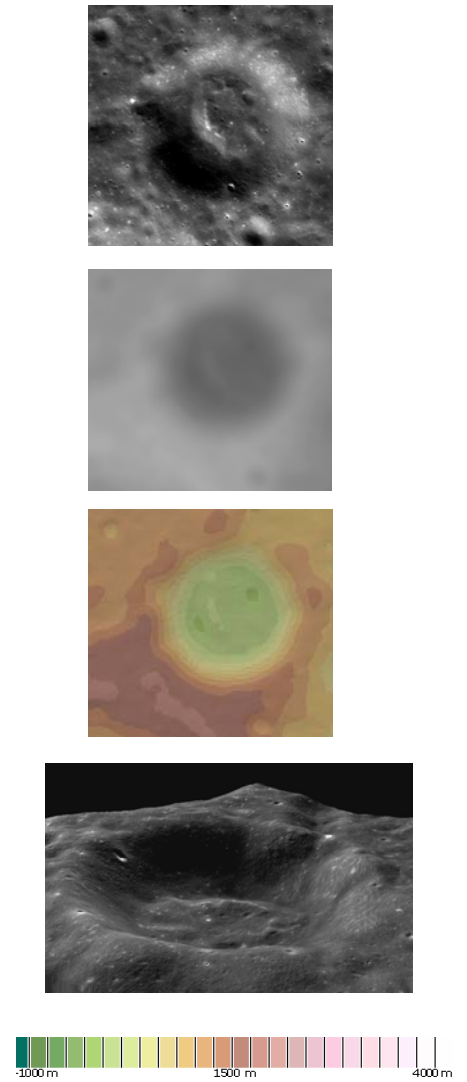


Figure-5: Orthoimage, DEM with color coding and Visualisation of Image draped over DEM (Coulomb C Crater) [4]

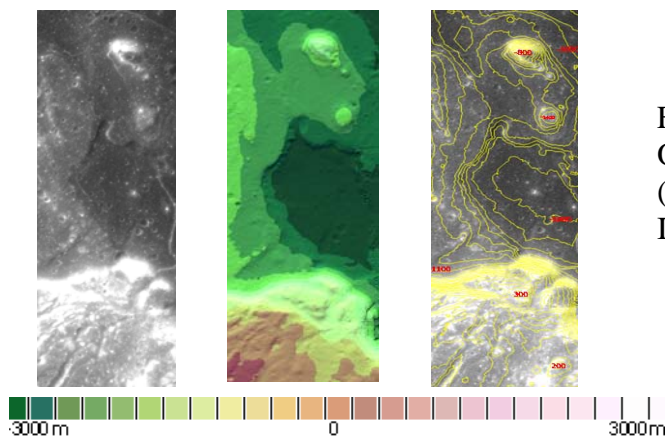


Figure-6: Part of Mare Orientale (a) Orthoimage (b) color coded DEM (20 km x 65 km long) (c) Contour Image [4]

Planetary Data Standards for Archival & Dissemination

By

**S. Manthira Moorthy
DPSG, SIPA, SAC**

Email: smmoorthi@ sac.isro.gov.in

Planetary Data Standards for Archival and Dissemination

S.Manthira Moorthi+ and B. Gopala Krishna*

+Operations Director, Chandrayaan-1 PDS & Long Term Archive

*Deputy Project Director, Chandrayaan-1 data processing & Mission Archive,
Group Director, SPDCG
Signal and Image Processing Area
Space Applications Centre (ISRO)

1.0 Introduction

The science data obtained from the instruments onboard Chandrayaan-1 will be archived in the Indian Space Science Data Center (ISSDC) for dissemination and use by the scientific community in India and abroad. The data from Chandrayaan-1 instruments is formatted and archived in such a way that they are easily accessible by Internet through simple interfaces being used elsewhere for similar kind of missions. NASA’s Planetary Data System (PDS) is the de facto standard for archival of long term archival of planetary science data.

2.0 What is PDS?

In 1972 the USA’s National Aeronautics and Space Administration (NASA), sent their first mission to explore an outer planet of the solar system, Pioneer 10. A data representation format that would allow long-term storage was developed in order to guarantee its usability long after the mission architects had retired. The standard that was adopted is called the Planetary Data System or PDS standard, (pds.jpl.nasa.gov). It has managed to survive till today because it has solved the double requirement of long-term data storage and flexible metadata organization.

Long term storage requires that the data be clearly set out such that several decades after the end of the mission, when the mission and instrument experts have long since retired, the data can still be interpreted meaningfully and even re-calibrated in the light of new findings. In order to achieve this, the PDS standard requires that all metadata files be in an ASCII or ‘human-readable’ format. This metadata is stored in text files using a simple keyword/value structure separated by new lines known as the Object Description Language (ODL, see the PDS Standards reference, pds.jpl.nasa.gov/documents/sr). This allows for an easy, ‘human-readable’, structure that does not require special software in order to read and understand the data stored in the PDS dataset. The data itself can be stored either in ASCII or binary formats, such as text tables, JPEG images files, or more complex 3-dimensional QUBE structures (appendix A.23 of PDS Standards reference, pds.jpl.nasa.gov/documents/sr/AppendixA.pdf).

The PDS standard has survived today thanks to its flexible and well-structured metadata organization. This is achieved using the Object Description Language. It

consists of groups of required and optional keyword/value pairs. These are referred to as objects. Objects can contain nested objects and by definition contain a list of required and optional objects (for an example see appendix A of PDS Standards reference, pds.jpl.nasa.gov/documents/sr/AppendixA.pdf). The definitions of the objects and keywords are stored in the PDS dictionary (pds.jpl.nasa.gov/tools/data_dictionary_lookup.cfm). Thus all metadata organizations have to conform to the structures defined in the dictionary. This is the strength of the standard. New requirements imposed by evolving mission constraints can be introduced into the dictionary. Furthermore, mission specific dictionaries are also a means of fine-tuning the standard to the missions. Henceforth, the standard allows for evolution of mission as well as instrument types, thus ensuring that future mission data can be stored using the PDS format.

The European Space Agency (ESA) has now adopted this standard for all of its future planetary and lunar missions. The Mars Express, SMART1, and Huygens missions have all been stored using the PDS standard into the Planetary Science Archive (PSA, www.rssd.esa.int/index.php?project=PSA).

3.0 ISRO Planetary Data System development

Indian Space Research Organization (ISRO) has also adopted this standard for all its current and future space missions including Chandrayaan-1 the first Indian lunar mission.

In order to achieve this it was decided that all data from a mission would have to abide by a strict definition of the PDS standard. In this context ISRO’ participation in Inter Planetary Data alliance (IPDA) activities will be important. Efforts are needed to avoid incoherent representations of the data due to different definitions. In science archives, there should be no data that is unusable. Therefore one of the precautions in PDS archive is to validate the PDS volume before ingesting into the archive.

4.0 Producing a PDS Archive for Chandrayaan-1 instruments

All instruments onboard Chandrayaan-1 platform is listed below with descriptions in Table-1.

4.1 Chandrayaan-1 Orbiter Science Instruments

Table 1: Ch1 orbiter instruments

Name	Description	PDS OBJECTS
Terrain Mapping Camera (TMC)	5 m spatial resolution and 20 km swath (400-900nm band). The camera has three observation modes viz., fore, aft and nadir.	IMAGE (BINARY)

Name	Description	PDS OBJECTS
	This is accomplished by using three suitably displaced linear arrays in the focal plane of a single lens	
Hyper Spectral Imager (HySI)	Hyper spectral wedges filter camera operating in 400-900nm band with a spectral resolution of 15nm and spatial resolution of 80 m, swath 20km. The hyper spectral camera has 64 channels	SPECTRAL_CUBE(BINARY)
Chandrayaan-1 X-Ray Spectrometer(C1XS) from RAL, UK and ISAC through ESA	A collimated low energy (1-10keV) X-ray spectrometer using CCD for measuring fluorescent X-rays emanating from the lunar surface having a foot print of approximately 20km	TABLE (ASCII)
Smart Infrared Spectrometer (SIR-2) from Max Plank Institute, ESA	Determine chemical composition of lunar crust and mantle and investigate the process of basin, Maria and crater formation on the Moon.	TABLE (BINARY) FITS
Radiation Dose Monitor (RADOM) from Bulgarian Academy of Sciences	Characterize quantitatively and qualitatively dose rate and deposited energy spectrum in terms of particle flux in near moon space.	TABLE(ASCII)
Mini SAR from APL and NAVAIR, USA	Obtain low-resolution topography of the lunar surface from an altitude of approximately 100 km and provide measurement sets associated with geodetic lunar global topography and composition.	IMAGE (BINARY)
Moon Mineralogy Mapper (M3) from JPL, NASA	Create a mineral-resource map of the moon	IMAGE(BINARY)
Sub keV Atom Reflecting Analyser from Swedish Institute of Space Physics, Sweden and SPL-India through ESA	Imaging of the Moon's surface composition including permanently shadowed regions and search for volatile-rich areas, surface magnetic anomalies. Studies of space weathering. Imaging of the	ARRAY/COLLECTION/TABLE (ASCII)

Name	Description	PDS OBJECTS
	sputtered sources of the exospheric gases and comparative studies of the exospheric gas production at moon.	
Lunar Laser ranging Instrument (LLRI) with height resolution of about 5 m	To determine the global topographical field of moon using the laser altimetry data. To determine an improvement model of the lunar gravity field. To interpret the new topographic and gravitational fields data for better understanding the geophysics of moon.	TABLE(ASCII)
High Energy X-ray (HEX) payload	A high-energy X-ray (10-200keV) mapping employing CdZnTe solid-state detectors having a footprint of approximately 40 km	TABLE (BINARY) FITS
Low Energy X-ray (XSM) payload	Collimated low energy (1-10keV) X-ray spectrometer using swept charge detector with a field of view of 20 km for chemical mapping of the lunar surface	TABLE (BINARY) FITS

4.2 Chandrayaan-1 Impact Probe Science Instruments

There are three science instrument subsystems on the Moon Impact Probe. The science instruments are listed below in 2 along with their measurement objectives.

Table 1: Moon Impact Probe (MIP) instruments

Name	Description
Moon Imaging System	Scientific exploration from near range and Design, development & demonstration of technologies required for impacting a probe at the desired location
Radar Altimeter	Measuring the altitude during the descent probe
Mass Spectrometer	Measuring the constituents of tenuous lunar atmosphere during the descent probe

4.3 Definition of Level-0 and Level-1 data products for Payloads at ISSDC

Scientific advisory board has given guidelines to define levels of corrections for data products. As a standard, two processing levels are identified for all payloads of Chandrayaan-1 for archival at ISSDC viz., Level ‘0’ is the Raw payload data along with ancillary information and Level ‘1’ processing involves radiometric and geometric calibration of payload data. All other higher levels are instrument specific.

4.4 CODMAC LEVELS

Committee on Data Management and Computation (CODMAC) data level numbering system is used to describe the processing level in PDS. Compare it with Chandrayaan-1 instruments processing levels. The CODMAC definitions are provided below.

CODMAC Level	Description
Raw – Level 1	Telemetry data stream as received at the ground station, with science and engineering data embedded.
Edited – Level 2	Instrument science packets (e.g., raw voltages, counts) at full resolution, time ordered, with duplicates and transmission errors removed. Corresponds to Space Science Board’s Committee on Data Management and Computation (CODMAC) Edited Data (see National Academy press, 1986).
Calibrated – Level 3	Level 0 data which have been located in space and may have been transformed (e.g. calibrated, rearranged) in a reversible manner and packaged with needed ancillary and auxiliary data (e.g., radiances with the calibration equations applied). Corresponds to CODMAC Calibrated Data.
Resampled – Level 4	Irreversibly transformed (e.g., resampled, remapped, calibrated) values of the instrument measurements (e.g., radiances, magnetic field strength). Corresponds to CODMAC Resampled Data.
Derived – Level 5	Level 1A or 1B data, which have been resampled and mapped onto, uniform space-time grids. The data are calibrated (i.e., radiometrically corrected) and may have additional corrections applied (e.g., terrain correction). Corresponds to CODMAC Derived Data.
Derived – Level 5	Geophysical parameters, generally derived from Level 1 data, and located in space and time commensurate with instrument location, pointing, and sampling. Corresponds to CODMAC Derived Data.
Derived – Level 5	Geophysical parameters mapped onto uniform space-time grids. Corresponds to CODMAC Derived Data.
Ancillary Data – Level 6	Data needed to generate calibrated or resampled data sets.

4.5 Archive Terminology Definition

Archive - a preservation of data for future use. For this document, archive pertains only to long-term archives using the PDS standard.

Archive System – The archive system is comprised of hardware, software, procedures, interfaces, and personnel necessary to complete the archiving of science and ancillary data with the PDS.

Data product -labeled data resulting from a scientific observation. Examples of data products include planetary images, spectrum tables, and time series tables. A data product is a component of a data set.

Data set - a labeled grouping of data products, metadata, documentation, and algorithms for applying calibration or further processing data. Software may also be included. A collection of closely-related PRODUCTS, intended to be distributed together.

Data object -A data object is that portion of a data product that contains the actual data that is described in a data object definition within a PDS label. It is tangible, and can be physically accessed and manipulated.

ODL -Object Definition Language, a parameter-value syntax used in PDS labels and catalog files

OBJECT -An ODL construct used in PDS label and catalog files to organize the attributes and parameters associated with a data file (in a label) or a high-level description (in a catalog file).

LABEL -ODL text describing both the physical format and the logical content of an associated data file

CATALOG FILE -An ODL file providing overview information and indexing keywords for some high-level aspect of the archive.

VOLUME -A physical unit for submission, publication or distribution.

5.0 Steps in producing a PDS archive

These are the steps in the archiving process according to PDS standard:

- Archive planning - deciding what to archive, when, and generally how
- Archive design - learning the details of putting an archive data set together
- Data set assembly and validation - pulling the pieces together
- Data set reviews - the final PDS quality check
- Delivery - passing the result to PDS

5.1 Chandrayaan-1 EAICDs

Details of the data archive structure and contents down to file level are specified by the Experiment to Archive Interface Control Documents (EAICD). The EAICDs are written by the individual instrument PI teams and describe the edited raw data, calibration data, calibrated data, derived higher-level data products and merge products (if any) as well as the software algorithms for generating the PDS labelled data products.

5.2 PDS content for any Level product

The CH1 archive will contain spacecraft data and instrument data, as well as derived or merged instrument data (wherever applicable).

The CH1 archive will be an online archive, where the data are delivered electronically. Thus there is no need to bundle several data sets into one volume, and one data set should correspond to one volume. A data set will include the data products as well as the secondary data, software and documentation that completely document and support the use of these data products. In general, the data products from the different instruments are contained in separate data sets. Data sets may include data products from one or separate data sets.

The top-level structure of the ROOT directory of a typical CH1 data archive volume (= data set) corresponds to chapter 19 of the PDS Standards Reference (AD6) and is summarised below (Fig-1):

- **AAREADME.TXT** file (required): This file describes the volume (= data set) as a whole. It gives an overview of the contents and organisation of the data set, general instructions for its use and contact information.
- **VOLDESC.CAT** file (required): This file contains the VOLUME object, which gives a high level description of the contents of the volume (= data set).
- **ERRATA.TXT** (optional): This file describes errors and/or anomalies found in this and previous volumes (= data sets). As erroneous data sets should be corrected and delivered again, there is no need for this file.
- **CATALOG** directory (required): This directory contains the catalog object files for the entire volume (= data set).
 - **CATINFO.TXT** (required): Description of the contents of the CATALOG directory.
 - **MISSION.CAT** (required): PDS mission catalog information about the CH1 mission will be provided by ISRO.
 - **INSTHOST.CAT** (required): PDS instrument host catalog information about the CH1 spacecraft and the mounting relationship of the instruments within the spacecraft will be provided by ISRO.

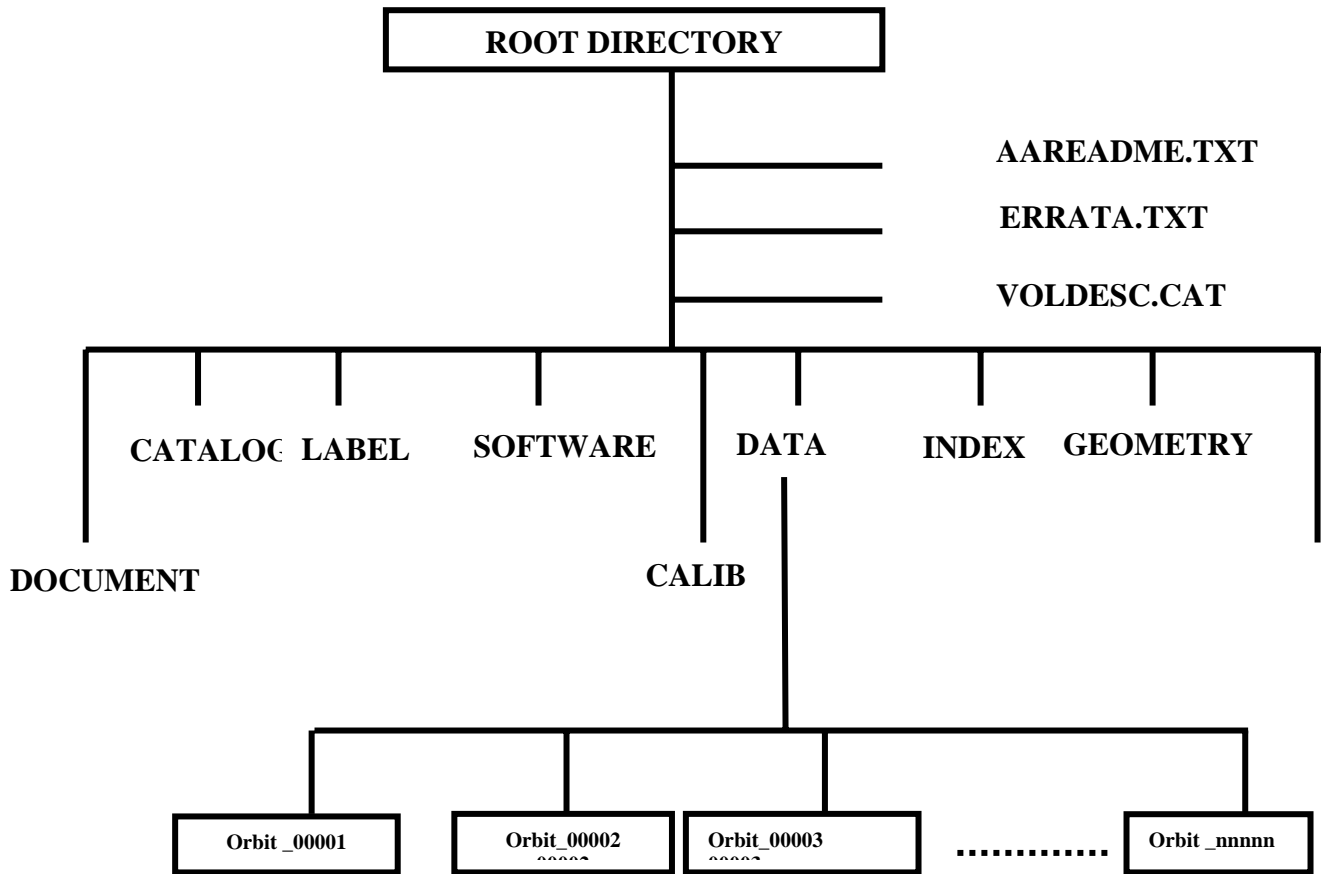


Fig-1: PDS Directory Tree

- **INST.CAT** (required): PDS instrument catalog information about the instrument (likely to be the same in all deliveries, unless updates are needed). There will be one file for each instrument providing data to this data set.
- **DATASET.CAT** (required): PDS data set catalog information about the data set currently being submitted.
- **REF.CAT** (required): PDS reference catalog information about the every journal article, book or other published reference mentioned in the above catalog objects or their components.
- **SOFTWARE.CAT** (required): PDS software catalog information about the software submitted in the data set.
- **TARGET.CAT** (optional): PDS target catalog information about the observation target, i.e. star or Earth, will be provided by ISRO.
- **PERSON.CAT** (optional): PDS personnel catalog information about the instrument team responsible for generating the data products. There will be one file for each instrument team providing data to this data set.
- **DATA** directory (required): This directory contains the actual data such as images or tables. PDS labelled data files or data files with detached PDS label files are arranged in a logical subdirectory structure.

- **INDEX** directory (required): This directory contains the index files summarising all data products in the volume (= data set) by mode, key instrument parameters or mission phase, and organised to facilitate finding the data of interest for a particular scientific question. Information about the observation geometry of the data products are also included here, i.e. spacecraft position and attitude, illumination conditions etc. Information that is not accurately known at the time of delivery and thus will probably be updated later should be stored in the index files rather than in the data product labels.
 - **INDXINFO.TXT** (required): Description of the contents of the INDEX directory.
 - **INDEX.LBL** (required): Detached label for the index table INDEX.TAB. The INDEX_TABLE specific object should be used to identify and describe the columns of the index table.
 - **INDEX.TAB** (required): Index of the data set in tabular format.
- **CALIB** directory (optional): This directory contains the calibration files used in the processing of the raw data or needed to use the data products in the volume (= data set). In addition, the description file CALINFO.TXT is required.
- **DOCUMENT** directory (optional): This directory provides documentation and supplementary and ancillary information to assist in understanding and using the data products in the volume (= data set). The documentation may describe the mission, spacecraft, instruments, data sets and calibration. The EAICD should be included. All documents must be present in ASCII format to ensure long-term readability. Document versions in other formats (Word, PDF, Framemaker, TeX etc.) are not required but encouraged. In addition, the description file DOCINFO.TXT is required.
- **EXTRAS** directory (optional): This directory is the designated area for housing useful but non-essential information beyond the scope of the PDS archive requirements. Examples are scientific papers, HTML or XML pages, tables and figures that describe the data products. Any format may be used. In addition, the description file EXTRINFO.TXT is required.
- **GAZETTER** directory (optional): This directory contains detailed information about the named features on the target bodies associated with the volume (= data set). The information given here needs not to be approved by the International Astronomical Union, but is provided as a convenience for the researchers in the future.
 - **GAZINFO.TXT** (required): Description of the contents of the GAZETTER directory.
 - **GAZETTER.TXT** (required): Text description of the structure and contents of the gazetter table GAZETTER.TAB.
 - **GAZETTER.LBL** (required): Detached PDS label containing a formal description of the structure of the gazetter table GAZETTER.TAB.
 - **GAZETTER.TAB** (required): Gazetter table.

- **GEOMETRY** directory (optional): This directory contains the files needed to describe the observation geometry for the data, i.e. trajectory and attitude of the spacecraft, shape model of target. In addition, the description file GEOMINFO.TXT is required.
- **LABEL** directory (optional): This directory contains PDS labels and includes files that are not packaged with the data products or in the data directory. Include files are files referenced by a pointer in a PDS label. Only files of type FMT, LBL and TXT may be located in the LABEL directory. In addition, the description file LABINFO.TXT is required.
- **SOFTWARE** directory (optional): This directory contains software for data calibration, visualisation and analysis. Algorithms concerning satellite information are supplied by mission. Only public domain software may be included in PDS archives. Source code is preferable over executable code. The subdirectory structure should indicate the hardware platform and operating system/environment. In addition, the description file SOFTINFO.TXT is required.
- **BROWSE** directory (optional): This directory contains browse representations (quick-look, thumbnail) of the data products.

5.3 PDS LABELS

PDS data product labels are required for describing the contents and format of each individual data product within a data set. PDS data product labels are written in the Object Description Language (ODL). The PDS has chosen to label the wide variety of data products under archival preparation by implementing a standard set of data object definitions, group definitions, data elements, and standard values for the elements. These data object definitions, data elements, and standard values are defined in the Planetary Science Data Dictionary (PSDD).

In order to identify and describe the organization, content, and format of each data product, PDS requires a distinct data product label for each individual data product file. These distinct product labels may be constructed in one of two ways:

Fig-2 shows how attached or detached label is associated with the data.

Attached - The PDS data product label is attached at the beginning of the data product file. There is one label attached to each data product file.

Detached - The PDS data product label is detached from the data and resides in a separate file which contains a pointer to the data product file. There is one detached label file for every data product file. The label file should have the same base name as its associated data file, but the extension “.LBL”. The software currently supports only a detached Label. Figure -2 shows this pictorially.

5.3.1 LABEL FORMAT

PDS recommends that labels have stream record format, and line lengths of at most 80 characters (including the CR/LF line terminators) so that the entire label can be

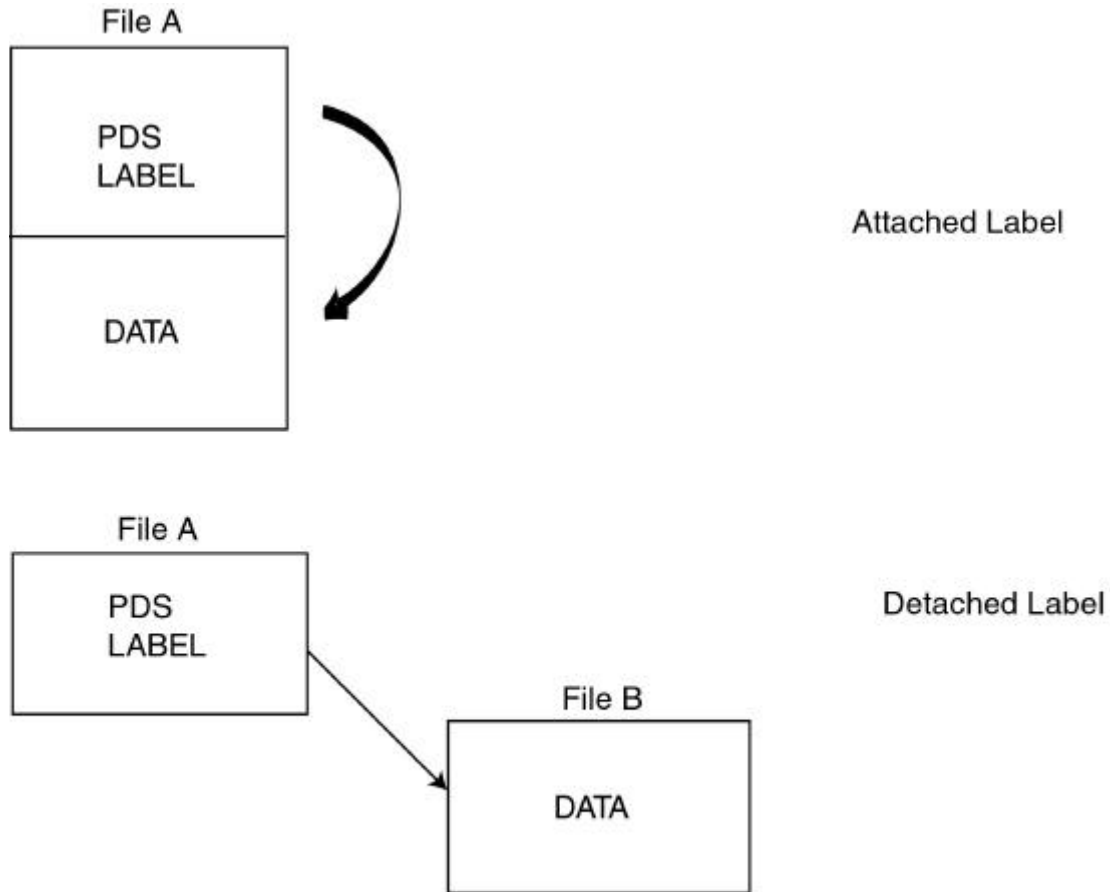


Figure-2: attached and detached label

seen on a computer screen without horizontal scrolling. The carriage return and line feed (CR/LF) pair is the required line terminator for all PDS labels.

PDS data product labels have a general structure that is used for all attached and detached labels,

- LABEL STANDARDS identifier
- FILE CHARACTERISTIC data elements
- DATA OBJECT pointers
- IDENTIFICATION data elements
- DESCRIPTIVE data elements
- DATA OBJECT DEFINITIONS
- END statement

Figure-3 provides an example of how this general structure appears in an attached or detached label for a data product file containing multiple data objects.

PDS LABEL		
PDS_VERSION_ID	=	• LABEL STANDARDS IDENTIFIERS
/*FILE_CHARACTERISTICS */		• FILE CHARACTERISTICS DATA ELEMENTS
RECORD_TYPE	=	
RECORD_BYTES	=	
FILE_RECORDS	=	
LABEL_RECORDS	=	
/*POINTERS TO DATA OBJECTS */		• DATA OBJECT POINTERS (primary, secondary)
^IMAGE	=	
^HISTOGRAM	=	
/*IDENTIFICATION DATA ELEMENTS */		• IDENTIFICATION DATA ELEMENTS
DATA_SET_ID	=	
PRODUCT_ID	=	
SPACECRAFT_NAME	=	
INSTRUMENT_NAME	=	
TARGET_NAME	=	
START_TIME	=	
STOP_TIME	=	
.		
.		
.		
PRODUCT_CREATION_TIME	=	
/*DESCRIPTIVE DATA ELEMENTS */		• DESCRIPTIVE DATA ELEMENTS
FILTER_NAME	=	
OFFSET_MODE_ID	=	
.		
.		
/*DATA OBJECT DEFINITIONS */		• DATA OBJECT DEFINITIONS (primary, secondary)
OBJECT	= IMAGE	
.		
.		
END_OBJECT	= IMAGE	
OBJECT	= HISTOGRAM	
.		
.		
END_OBJECT	= HISTOGRAM	
END		• END STATEMENT

Figure-3: An example label template

5.3.2 File Characteristics Data Elements

The following keywords are defined for this section:

```
FILE_NAME           = "TMC_NEN_20081219T0224253263.IMG"
RECORD_TYPE        = FIXED_LENGTH
RECORD_BYTES       = 8000
FILE_RECORDS       = 193162
```

5.3.3 Data Object Pointers

All data files in the archive have PDS labels, either embedded at the beginning of the file or detached in a separate file. In an embedded label, the location is an integer representing the starting record number of the object. In a detached label, the location denotes the name of the file containing the object, along with the starting record or byte number, if there is more than one object in the file. For example:

The following keywords are defined typically:

```
^BROWSE_IMAGE      = "filename.ext"
^IMAGE             = "filename.IMG"
^HISTORY           = n <RECORD #>
^SPECTRAL_QUBE    = m <RECORD #>
^SPECTRAL_QUBE    = ("[dirlist] filename.QUB", n <BYTES>)
```

5.3.4 Identification Data Elements

The following keywords are defined for this section:

```
RELEASE_ID         = 1
DATA_SET_ID        = "CH1ORB-L-TMC-2-NPO-EDR-RAW-DATA-V1.1"
DATA_SET_NAME      = "CHANDRAYAAN-1 ORBITER MOON TMC 2 NPO EDR
                    RAW DATA V1.1"
PRODUCT_ID         = TMC_NEN_20081219T0224253263
PRODUCT_CREATION_TIME = 2009-07-21T15:44:22.002Z
PRODUCT_TYPE       = "EDR"
PRODUCER_ID        = "CH1-ISRO-SAC-DP-TEAM"
PRODUCER_FULL_NAME = "CHANDRAYAAN-1 ISRO SAC DATA
                    PROCESSING TEAM"
PRODUCER_INSTITUTION_NAME = "SPACE APPLICATIONS CENTRE,
                            (ISRO) AHMEDABAD"
PROCESSING_LEVEL_ID = 2
PROCESSING_LEVEL_DESC = "2 Experiment Data Record,
                        3 Reduced Data Record"
MISSION_ID         = "CH1"
MISSION_NAME       = "CHANDRAYAAN-1"
MISSION_PHASE_NAME = "NORMAL PHASE OPERATIONS"
INSTRUMENT_HOST_ID = "CH1ORB"
INSTRUMENT_HOST_NAME = "CHANDRAYAAN-1-ORBITER"
TARGET_NAME        = "MOON"
TARGET_TYPE        = "SATELLITE"
```

```

START_TIME           = 2008-12-19T02:24:25.3263
STOP_TIME            = 2008-12-19T02:34:50.722
SPACECRAFT_CLOCK_START_COUNT   = "NULL"
SPACECRAFT_CLOCK_STOP_COUNT    = "NULL"
ORBIT_NUMBER         = 00485
IMAGE_OBSERVATION_TYPE = "REGULAR"
    
```

5.3.5 Descriptive Data Elements

```

INSTRUMENT_ID       = "TMC"
INSTRUMENT_NAME     = "TERRAIN MAPPING CAMERA"
INST_CMPRS_NAME     = "ISRO PROPRIETARY"
FILTER_NAME        = "NONE"
LINE_EXPOSURE_DURATION = 3.236 <ms>
FOCAL_PLANE_TEMPERATURE = 6.0000000000 <K>
INSTRUMENT_TYPE    = "LINE ARRAY CAMERA"
DETECTOR_PIXEL_WIDTH = 7 <micron>
FOCAL_LENGTH       = 140 <mm>
SOFTWARE_NAME      = "CH1DPGS"
SOFTWARE_VERSION_ID = "V1.0"
    
```

5.3.6 Data Object Definition

The TMC products will contain two objects, a "browse image" and the full resolution image. The keywords to describe these objects are described in this section.

The browse image always shows a 512 x n version of the full image. This means that from the browse image the user can quickly see what is contained in this file. An example is given below.

```

OBJECT              = IMAGE
LINES               = 193162
LINE_SAMPLES        = 4000
SAMPLE_TYPE         = LSB_UNSIGNED_INTEGER
SAMPLE_BITS         = 16
SAMPLE_BIT_MASK     = "<2#0000111111111100>"
MAXIMUM             = 843.0000000000
MINIMUM             = 0.0000000000
MEAN                = 222.7663176721
STANDARD_DEVIATION = 57.5109323817
VERTICAL_PIXEL_SCALE = 5 <m/pixel>
HORIZONTAL_PIXEL_SCALE = 5 <m/pixel>
SAMPLE_DISPLAY_DIRECTION = RIGHT
END_OBJECT          = IMAGE
    
```

LINES is the number of lines in the image.

LINE_SAMPLES is the number of samples in each line.

SAMPLE_BITS is the number of bits in each individual sample.

SAMPLE_TYPE defines the sample data type.

5.3.7 The TABLE OBJECT

TABLEs are a natural storage format for collections of data from many instruments. They are often the most effective way of storing much of the meta-data used to identify and describe instrument observations.

The TABLE object is a uniform collection of rows containing ASCII or binary values stored in columns. The INTERCHANGE_FORMAT keyword is used to distinguish between TABLEs containing only ASCII columns and those containing binary data. The rows and columns of the TABLE object provide a natural correspondence to the records and fields often defined in interface specifications for existing data products. Each field is defined as a fixed-width COLUMN object; the value of the COLUMNS keyword is the total number of COLUMN objects defined in the label.

All TABLE objects must have fixed-width records.

Many variations on the basic TABLE object are possible with the addition of optional keywords and/or objects. While it is possible to create very complex row structures, these are often not the best choices for archival data products. Recommended ASCII and binary table formats are described and illustrated below.

TABLE contains the following REQUIRED keywords to define the parameters

1. INTERCHANGE_FORMAT
2. ROWS
3. COLUMNS
4. ROW_BYTES

TABLE contains the following OPTIONAL keywords to define the parameters

1. NAME
2. DESCRIPTION
3. ROW_PREFIX_BYTES
4. ROW_SUFFIX_BYTES
5. TABLE_STORAGE_TYPE

ASCII tables provide the most portable format for access across a wide variety of computer platforms.

They are also easily imported into a number of database management systems and spreadsheet applications.

For these reasons, the PDS recommends the use of ASCII table formats whenever possible for archive products.

ASCII formats are however generally less efficient for storing large quantities of numeric data. In addition, raw or minimally processed data products and many pre-existing data products undergoing restoration are only available in binary formats.

Where conversion to an ASCII format is not cost effective or is otherwise undesirable, BINARY table formats may be used.

The recommended format for ASCII TABLE files is a comma-separated value format in which the string fields are enclosed in double quotes. ASCII tables must have fixed-length records and should use carriage-return/linefeed (<CR><LF>) delimiters.

Numeric fields are right-justified in the allotted space and character fields are left-justified and blank padded on the right. This table format can be imported directly into many commercial data management systems.

The following label fragment illustrates the general characteristics of the recommended ASCII TABLE.

5.4 Free PDS Reader Softwares

There are few free types of software for viewing PDS datasets provided by NASA. They help viewing basic PDS objects like IMAGE, QUBE and TABLES. However they are not complete analysis software. So therefore user should have an analyzing tool at his end for his doing science. Following are the popular PDS readers.

5.4.1 READPDS (NASA)

READPDS. Set of IDL procedures for reading the PDS labels common to small bodies datasets. The latest release is version 4.3. This package is intended primarily for end-users of PDS data. Note that as of version 4.2, ReadPDS requires IDL version 6.0 or later.

Platforms:

- Windows
- Most Unix platforms
- Mac OS-X

<http://pdssbn.astro.umd.edu/>

5.4.2 NASAView (NASA)

NASAView. PDS archive product display program that runs on multiple platforms in a GUI environment. This application was built using the Label Library Light (L3), Object Access Library (OAL) and the XVT Development Solution for C package. Label Library Light parses PDS ODL labels and creates an in-memory representation of the label information. The Object Access Library uses the parse tree and accesses the actual PDS object. The XVT Development solution supplies the cross-platform GUI support and an object-oriented environment.

Platforms:

- Windows
- Most Unix platforms
- Mac OS-X

<http://pds.jpl.nasa.gov/tools/nasa-view.shtml>

5.5 Archive Validation and Distribution

A detailed description of the review procedure can be found in the Planetary Missions Science Archive Review Procedure (RD06). ISRO proposes to follow similar procedure for CSDA. Below a summary is given.

The review is a three-step process consisting of (i) the Peer Review of the Archive Plan (this document) and the individual EAICDs (EAICD Review), (ii) the review of the first data delivery (Initial Peer Review) and (iii) the review of all data sets together after the final delivery (Final Peer Review).

(a) The ISRO science data archive team arranges the Peer Reviews. It is proposed to appoint separate review panels for the individual instruments. The external review team members and the review chairpersons will be agreed on in the SWT.

(b) The Peer Review team verifies the data sets /documents. The tasks of the team can be best compared to the tasks of a referee for a paper to be published in a scientific journal.

(c) Arising problems (called "liens" in PDS jargon) will be resolved by the concerned experiment/PI teams, and the ISDA team. Data sets where liens occurred and the Peer Review team proposed clear solutions to these liens, do not have to undergo an additional Peer Review. In case of more serious liens, revision and reviewing of the data sets will be iterated.

(d) Depending on the result of the Peer Review, the CSDA will indicate the status of the reviewed data set as "successfully peer reviewed", "peer review is pending" or "failed peer review". At the conclusion of the review / revision process all data sets should be "successfully peer reviewed".

5.6 Peer reviews

Prior to archive by PDS, the data sets need to be reviewed. The purpose of the review process is to ensure the accuracy, dependability, and usefulness of science data to be distributed by PDS. The primary goal is to make sure the data is well documented for future users. PDS archive cannot be left to grow by itself, but to be reviewed time to time to assess the quality of the PDS data sets in the archive by an expert team. Such peer reviews are essential before ingesting into archive especially Level-1 products and beyond.

5.7 Online Archive dissemination

Peer reviewed PDS data sets are made available online. The user will be able to query the data sets based on the data descriptions provided. When the user identifies the data set in which he is interested, it can be requested for download.

References

- [1] NASA/JPL., “Planetary Data System Data Preparation Workbook”, Doc. No. JPL D-7669, Part 1, February 17, 1995, Version 3.1, <http://pds.jpl.nasa.gov/documents/dpw/index.html>
- [2] NASA/JPL., Planetary Data System Standards Reference, JPL D-7669, Part-2. March 20, 2006, Version 3.7, <http://pds.jpl.nasa.gov/documents/sr/index.html>.
- [3] Jagjeet Nain., Gopala Krishna, B., “CHANDRAYAAN-1 Archive Plan”, Doc.No. CH1-SAC-PL 001, Issue 1,Rev.a, 31 Dec 2007
- [4]Manthira Moorthi, S., Gopala Krishna, B., “CHANDRAYAAN-1 Archive Conventions”, CH1- SAC-PL-002, Issue 1, Rev. a, 31 Dec 2007
- [5] Dublin Core Metadata Initiative. The Dublin Core Element Set Version 1.1, Dublin: DMCI, July 1999.

Lunar Mapping and Atlas

By

**Amitabh
SPDCG, SIPA, SAC**

Email: [amitabh@ sac.isro.gov.in](mailto:amitabh@sac.isro.gov.in)

Lunar Mapping and Atlas Generation

Amitabh and B Gopala Krishna

Satellite Photogrammetry & Digital Cartography Group
Space Applications Centre (ISRO), Ahmedabad-380015
amitabh, bgk@sac.isro.gov.in

Contents of Tutorial :

- 1. Introduction**
- 2. Planetary Versus Terrestrial Mapping**
- 3. Chandrayaan-1 Map Catalogue**
- 4. Projection and Datum**
- 5. Input Datasets Requirement**
- 6. Map Index**
- 7. Nomenclature and Feature Identification & extraction**
- 8. Overview of Map**

1. Introduction

In the past four decades the exploration of moon has become a reality. A number of missions have been flown to the moon by many countries. Many of these missions have carried imaging systems that, collectively, have returned an incredible wealth of information on the shape and surface characteristics of planetary objects. Mapping of moon began in the seventeenth Century by Galileo. Chandrayaan-1 is the India's first mission to moon for mapping the different aspects of the lunar surface.

Throughout history, maps and charts have played an integral role in the exploration of earth. Their importance holds true for moon exploration as well. Maps of the planets are needed by planners of spaceflights to design missions, including the selection of safe and scientifically fruitful landing sites, and are the framework for recording measurements from a wide variety of spacecraft instruments.

The high level data products defined for Chandrayaan-1 mission includes the Lunar Atlas and maps. An Atlas serves many purposes: the need to have a ready compilation of maps to locate features, a desire casually to explore an unknown territory, or a summary of existing knowledge about a barely familiar place. The inspiration to prepare Chandrayaan-1 atlas is different kinds of high resolution datasets received from the most successful Chandrayaan-1 mission instruments.

The making of moon maps has required the new methods and techniques. Most of the commercial mapping software supports the map making of earth surface features based on earth projection and datum but the utilization of same in the current form is not possible for mapping the lunar surface because of the absence of planetary projection and datum in the available software. Many of the basic principles derived from the mapping of the earth must be reconsidered in the mapping of the moon.

2. Planetary Versus Terrestrial Mapping

Maps of earth’s surface have been produced primarily by piecing together large-scale sketches and diagrams since centuries. Control networks were derived through extensive and laborious ground surveying. By the late nineteenth century, regional maps were produced in this fashion that was relatively accurate. With twentieth-century technology came the ability to obtain the synoptic view. Photographs taken from earth-orbiting satellites enabled the rapid production of accurate maps. When combined with well established control networks, these maps have enabled surface features on earth to be located precisely. Planetary explorers, on the other hand, have had the global perspective from the beginning, and they have progressed from global, through regional, to local vantages.

The naming of features is as much a part of map making as are the measuring and plotting of their locations. Without names, communication of ideas is impossible. The names applied by explorers on earth often bear their provincial outlook. Ambiguities abound; settles on different parts of the same river often know the river by different names. The tradition that the privilege of naming belongs to the discoverer resulted in hopeless ambiguities, redundancies and inconsistencies. The International Astronomical Union (IAU) has therefore assumed control of the naming process. It’s working groups are composed of planetary scientists from many nations.

3. Chandrayaan-1 Map Catalogue

A map Catalogue is nothing but a collection of maps produced from various map series. A map series is a set of maps of a specific planet that have a specified scale, projection scheme, and map type (Planimetric, topographic, geologic etc.). Thus planetary map series are designed to specific requirements:

1. To produce small-scale and synoptic maps showing entire moon surface on single sheets for data indexing and planning and as bases for global geologic maps.
2. To produce a series of regional maps in which planets are segmented into quadrangles as necessary, depending on resolution of available data.
3. To produce standard map scales for similar map series, regardless of planet, for comparative studies.

ISRO Lunar map catalogue will contain different types of maps generated at 1:1 Million, 1:250,000, 1:50,000 and 1:25,000 scale. This will consists of the following maps:

- Lunar Topomap
- Lunar Ortho-image (PAN, FCC, NCC) map
- Lunar Topo-Ortho Image map
- Lunar Thematic Maps (Reference Contributory Themes by different POCs)

The lunar topomap will be composition of color coded DEMS with annotation. Lunar Ortho-image map will contain PAN, FCC and NCC orthoimage with annotation while Lunar Topo-Ortho map will contain contours overlaid on Orthoimage with annotation. Lunar thematic maps will contain thematic layers provided by different POCs. The basic diagram for the map production is as shown in fig-1. This can be realized by using the customization of the required COTS packages. The COTS packages are helpful even in generation of various layers of the Lunar Atlas, which are the outputs.

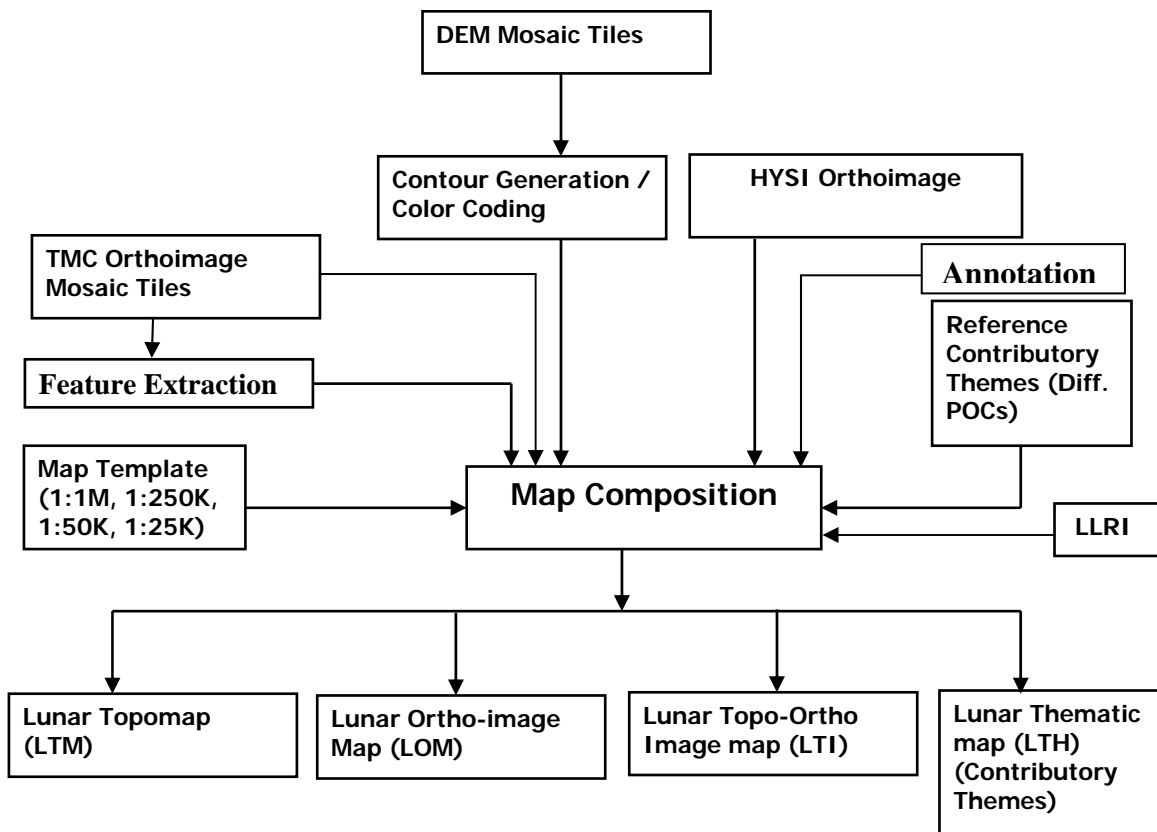


Figure-1: Basic Diagram of ISRO Lunar Map Catalogue

4. Projection and Datum

Maps are needed to show shapes, dimensions, and areas, but no one map projection can achieve all of these goals well. Conformal projections like the Mercator, Transverse Mercator, Lambert Conformal Conic, and Polar stereographic retain the true shapes of small landforms and are favoured by scientists wishing to recognize and interpret phenomena characterized by shape. Equal area projections, on the other hand, are useful in evaluating the distributions of surface features, such as craters, especially at global scale.

Map projections can be visualized as planes, cones, or cylinders tangent to or intersecting a sphere. Features on the globe are projected onto the planes, cones, or cylinders according to some mathematically defined system. The polar stereographic is the simplest conformal projection used in planetary cartography, and it can be constructed graphically. Although it is sometimes useful to think of Transverse and normal Mercator Projections as cylinders and of Lambert Conformal Conic projection as cones, these are mathematically modified to achieve the conformal condition and are not graphical projections. Standard parallels, Central meridians, and projection centers define the location of true or constant scale on map projections. These are the lines or points at which a projection intersects or lies tangent to a globe. For preparing the maps from Chandrayaan-1 datasets we have considered Polar stereographic for polar regions (70 degree to 90 degree north & 70 degree to 90 degree South) and Transverse Mercator for rest of the regions.

The horizontal datum of the moon has been considered as 1737.4 Km i.e., Mean radius of the moon. Until 1981, all lunar topographic maps were compiled on a spherical datum. An equipotential reference surface for the moon was computed by Wu (1985); the vertical datum is based on the lunar gravity field expressed in terms of spherical harmonics of fifth degree and fifth order, with the sixth-degree sectorial terms. Gravity coefficients used for the derivation of the datum were developed by Sjogren, who worked with Lunar Orbiter 4 tracking data and laser ranging data.

The coordinate reference system is based on OGC Planetary coordinate reference system as given below.

```
GEOGCS["GCS_Moon_2000",DATUM["D_Moon_2000",SPHEROID["Moon_2000_IAU_IAG",1737400.0,0.0]],PRIMEM["Reference_Meridian",0.0],UNIT["Degree",0.0174532925199433]]
```


5. Input Datasets Requirement

Following inputs are required for mapping the moon surface:

- Ortho Image / Image Mosaic of TMC nadir image (Grid Size = 5m & 10 m)
- DEM Tiles of 45’X45’ (Grid Size = 20 m)
- HySI Ortho Images (NCC, FCC)
- Reference Contributory Themes

6. Map Index

Common Nomenclature for Maps in TM Projection (70N to 70S Lat.) is as follows.

1:1Million Scale (20d x 20d)

39	40
41	42

1:250,000 Scale (5d x 5d)

39A	39E	39I	39M
39B	39F	39J	39N
39C	39G	39K	39O
39D	39H	39L	39P

1:50,000 Scale (1d x 1d)

39A1	39A6	39A11	39A16	39A21
39A2	39A7	39A12	39A17	39A22
39A3	39A8	39A13	39A18	39A23
39A4	39A9	39A14	39A19	39A24
39A5	39A10	39A15	39A20	39A25

1:25,000 Scale (30’ x 30’)

039A1NW	39A1NE
39A1SW	39A1SE

Legend:

1st Number (2digit) = 1:1 Million Map ; 1st Alphabet = 1:250, 000 Map

2nd Number (2 digit) = 1:50,000 Map; NW: North West; NE: North East; SW: South West; SE: South East

7. Nomenclature and Feature Identification & extraction

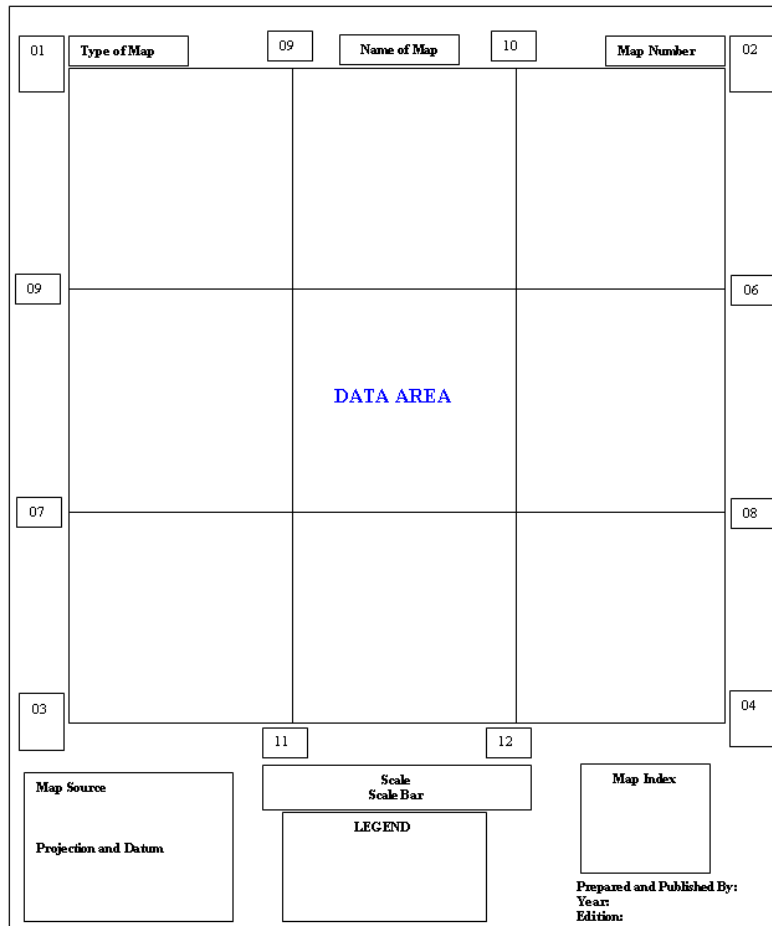
The nomenclature of the features will be based on *Gazetteer of Planetary Nomenclature* which will follow the IAU rules and conventions. The features will be extracted as per cartographic standards. The topographic feature of the moon to be extracted will include Index contour, Intermediate contours, Supplementary contours, Slope ticks, crater rim and interior elevations and Spot elevation. Few of the feature types are as follows:

- Crater
- Crater Chain
- Plain
- Mountain Range
- Craterlet
- Walled Plain
- Mountain
- Dome

- Dome System
- Wrinkle ridges Network
- Rille
- Valley
- Lake
- Cape
- Ejecta
- Human Mission
- Mare
- Wrinkle ridge
- Scrap
- Rilles Network
- Marsh
- Sea
- Bay
- Probe
- Inert equipment

8. Overview of Map

A. Layout:



01 – 12: Graticules in Geographic (Latitude / Longitude)
Every 1000 m one tick-mark will be placed in Easting / Northing

Figure: Overview of Map Layout

B. Samples of Maps

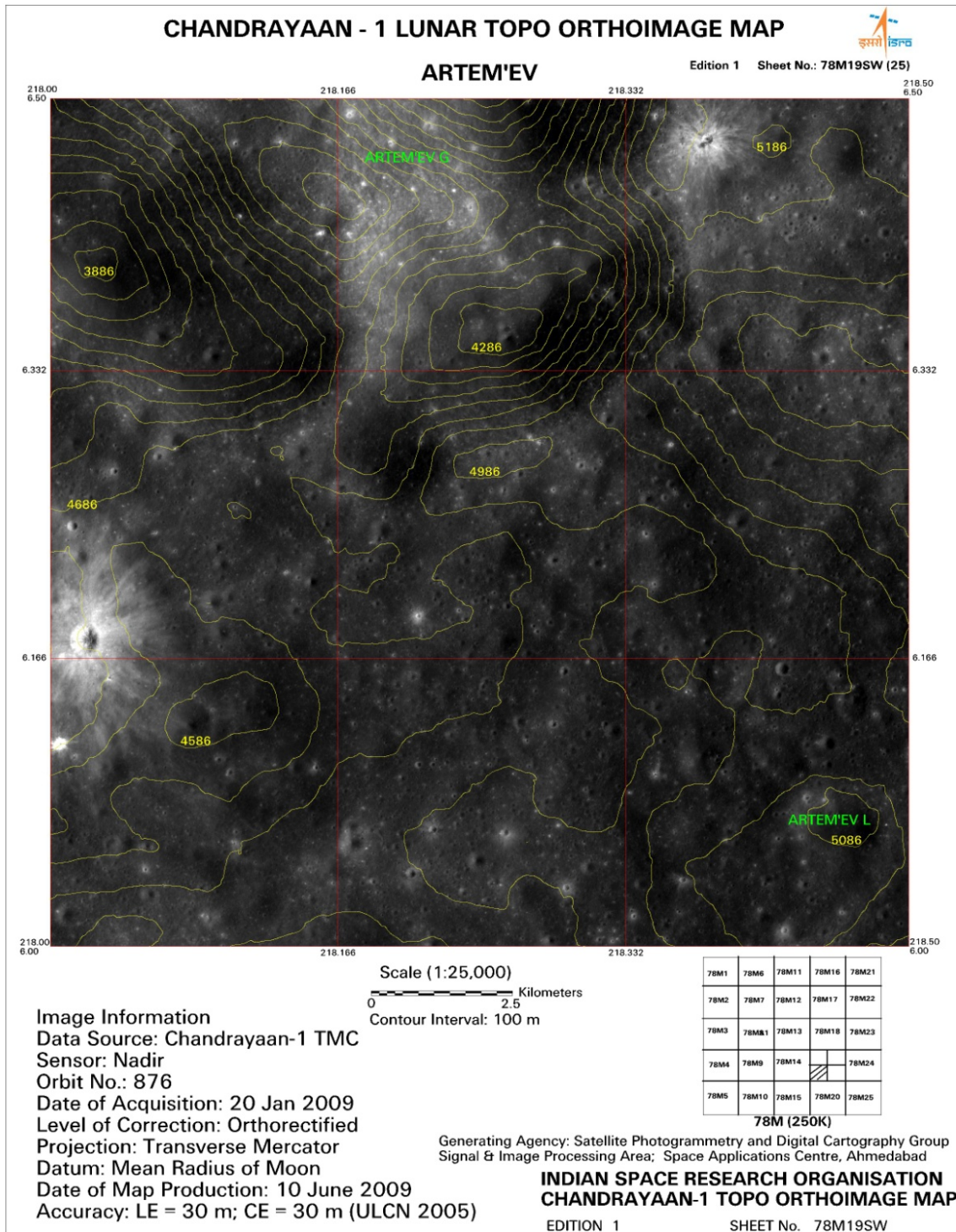


Figure: Overview of One of the map Prepared

Bibliography:

1. **“Lunar Cartographic Dossier Vol-1”**, Lawrence A. Schirmerman, NASA , 1973
2. **“Combining lunar photogrammetric topographic data with Clementine LIDAR data”** M. R. Rosiek, R. Kirk, and E. Howington-Kraus United States Geological Survey, Astrogeology Team, Flagstaff AZ 86001
3. **“Planetary Mapping”**, Ronald Greeley and Raymond M. Batson; Cambridge University Press 1991
4. **“Geologic Map of Near Side of Moon”**, Don E Wilhelms and John F Mc Cauley, USGS report for NASA, 1971
5. **“Cartography For Lunar Exploration : 2008 Status and Mission Plans”**, R.L. Kirk, B.A. Archinal, L.R. Gaddis, and M.R. Rosiek; U.S. Geological Survey, Flagstaff, AZ 86001, USA, Commission IV, WG IV/7; ISPRS Congress 2008
6. **“General Architecture Design of Lunar Projection”** Lü xiaohua,, Deng Shujuna and Ma Juna; Institute of Surveying and Mapping, Information Engineering University, 66 Longhai Road ,ZhengZhou,450052 ,China, Commission IV, WG IV/7; ISPRS Congress 2008
7. **“Chandrayaan-1 Lunar Atlas and Maps: A Definition Document”** by Amitabh and B Gopala Krishna; SAC/SIPA/SPDCG/TN-xx/feb. 2009

Planetary Exploratory Applications: Chandrayaan-1 TMC view

By

**Ashutosh Arya
MESG, RESA, SAC**

Email: [arya_as@ sac.isro.gov.in](mailto:arya_as@sac.isro.gov.in)

Planetary Exploratory Applications: Chandrayaan-1 TMC View

A.S. Arya
ESH/MESG/RESA
Space Applications Centre,
Ahmedabad – 380 015
arya_as@sac.isro.gov.in

Moon, is a natural satellite of Earth and is about **4.60 billion years old**, or about the same age as Earth. The **diameter** of Earth’s Moon is about 3,480 km (about 2,160 mi), or about **one-fourth** that of Earth and volume is about one-fiftieth that of Earth. The **mass** of Earth is 81 times greater than the mass of the Moon while the **average density** of the Moon is only **three-fifths** of the earth. The gravitational pull at the lunar surface only **one-sixth**, that of Earth. The Moon has **no liquid-water** and essentially **no atmosphere**, so no weather exists to change its surface; yet it is not totally inert. The distance of Moon from the Earth is about **384,403 km**

The Moon revolves around the earth at an average speed of **3,700 km/h** and completes one revolution in an elliptical orbit about Earth in **27 days 7 hours 43 minutes 11.5 seconds**. For the Moon to go from one phase to the next similar phase, or **one lunar month**, requires **29 days 12 hours 44 minutes 2.8 seconds**.

Although the Moon appears bright to the eye, it reflects into space only **7 percent** of the light that falls on it. At any one time, an observer can see only **50 percent** of the Moon’s entire surface – the near side. Far side is never visible to a viewer on Earth.

Temperatures on its surface are extreme, ranging from a **maximum of 127°C** (261°F) at lunar noon to a minimum of **-173°C** (-279°F) just before lunar dawn.

For a long time, the fundamental question regarding the history of the Moon was about its origin. Early hypotheses included *fission* from the Earth, *capture*, and

co-accretion. Today, the *giant impact hypothesis*, postulated by Reginald Aldworth Daly in 1940's, and which became popular in 1984, is widely accepted by the scientific community. Accordingly the origin of the Moon involves a collision of two protoplanetary bodies during the early accretional period of Solar System evolution. Moon came into existence about 4.6 billion years ago and after solidification of its crust a significant percentage of the lunar impact basins formed within a very short period of time between about 4 and 3.85 Ga ago (lunar cataclysm hypothesis). Many big and huge craters came into existence, which formed enormous basins. The heavy and continuous impacting resulted in volcanism on Moon which filled these basins with dark colored basaltic lava. This is why when we see the Moon from earth with naked eyes, we see two distinct colors on the Moon, the dark patches are called MARE (younger rocks) and the bright areas are HIGHLANDS (older rocks.). It is interesting to note that only one side of the Moon is visible from Earth all the time and thus it is called the NEAR-SIDE and the opposite one is the FAR-SIDE (fig. 1).



Fig. 1: Near-Side and Far-Side view of the Moon

The Moon has no physical weathering like water-erosion, wind-erosion, frost-shattering etc, so no erosion/ degradation as known on earth is applicable on the Moon. However, the Moon experiences *space weathering* due to high energy particles, *solar wind implantation*, and *micrometeorite impacts*.

The lunar landscape is characterized by impact craters, their ejecta, hills, lava flows and depressions filled by magma etc. A lot of these features vary in size from several kms. to few cms, or even less. Thus the Lunar surface furnishes an

excellent opportunity to study and map all these features to re-construct the history of the Moon, and satellite remote sensing is the best and fastest way to do this .

Chandrayaan-1 is the maiden Indian planetary mission to the moon, realised by the state of art technology involving 11 different & complimentary sensors. One of the sensors, the Terrain Mapping Camera (TMC) has high spatial resolution of 5 m and multi viewing capability, enabling 3 dimensional view of the Lunar surface [1]. The TMC camera images the Lunar surface in the panchromatic spectral region of 0.5 to 0.85 μm with a spatial/ ground resolution of 5m, 10 bit quantization and swath coverage of 20 Km. The camera has been configured for imaging in the push broom mode with three linear 4K element detectors in the image plane for fore, nadir and aft views in the along track direction of satellite movement. The strength of this camera lies in its high resolution and 3D imaging capabilities providing unique opportunity to study the lunar terrain in unprecedented way. The primary aim of TMC is to map topography in both near and far side of the Moon and prepare a 3-dimensional atlas with high spatial and altitude resolution. However, for geological purpose the TMC data is used primarily to map the morphology, structural features and crater studies, in order to answer the science questions related to the origin & evolution of the Moon as well as the Earth-Moon system. The digital elevation model available from TMC along with the Lunar Laser Ranging Instrument (LLRI) on Chandrayaan-1 will also improve the Moon gravity model. Parts of the near and far side of the Moon has been covered in strip (swath of 20kms) mode and some of these strips have been processed and visually interpreted for identification of various features on the Moon, especially the morphological features, faults, grabens, lava-flows, crater types etc.

Some of the Lunar features viz. types of craters, rille etc, as viewed by the TMC camera, are given below (fig. 2, 3, 4 & 5):

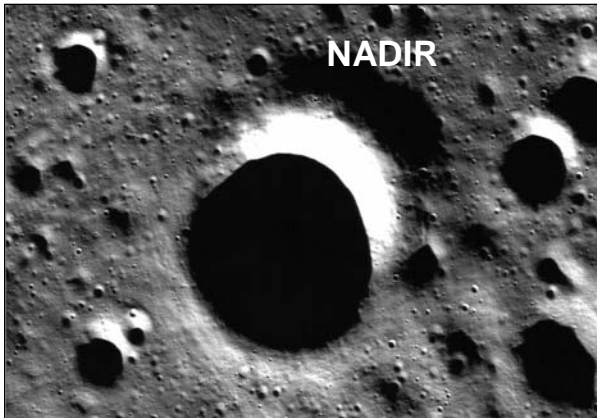


Fig. 2: Simple/Conical Crater: (Nearside 16.11.2008)

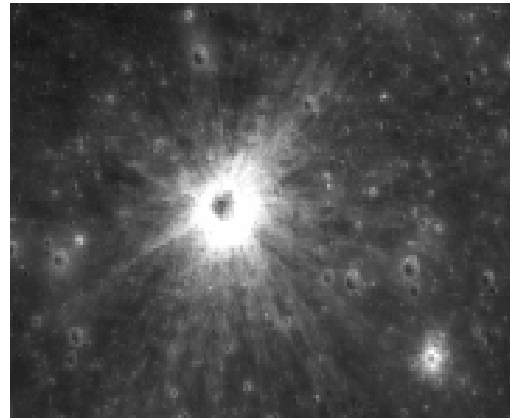


Fig. 3: Ray Crater (Far-side - 24.11.08)



Fig. 4: A typical 'Sinuous Rille' indicating a collapsed lava tube, tapering away from the crater (Near Side 13.1.2009)

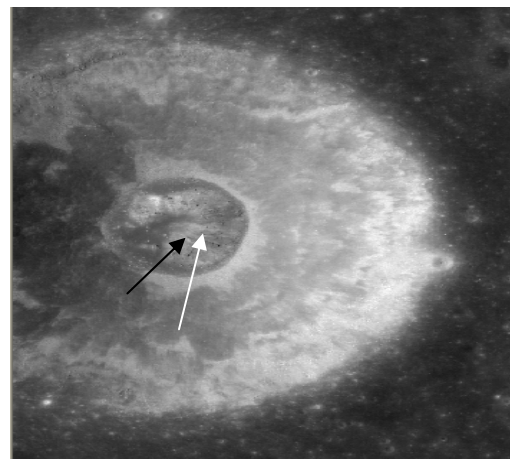


Fig. 5: Complex Crater with a central dome (see arrow): Far-side (13 Jan 2009)

The following image shows a major break in the Lunar surface showing part of a faulted rim of More tus crater near the south pole (fig. 6).

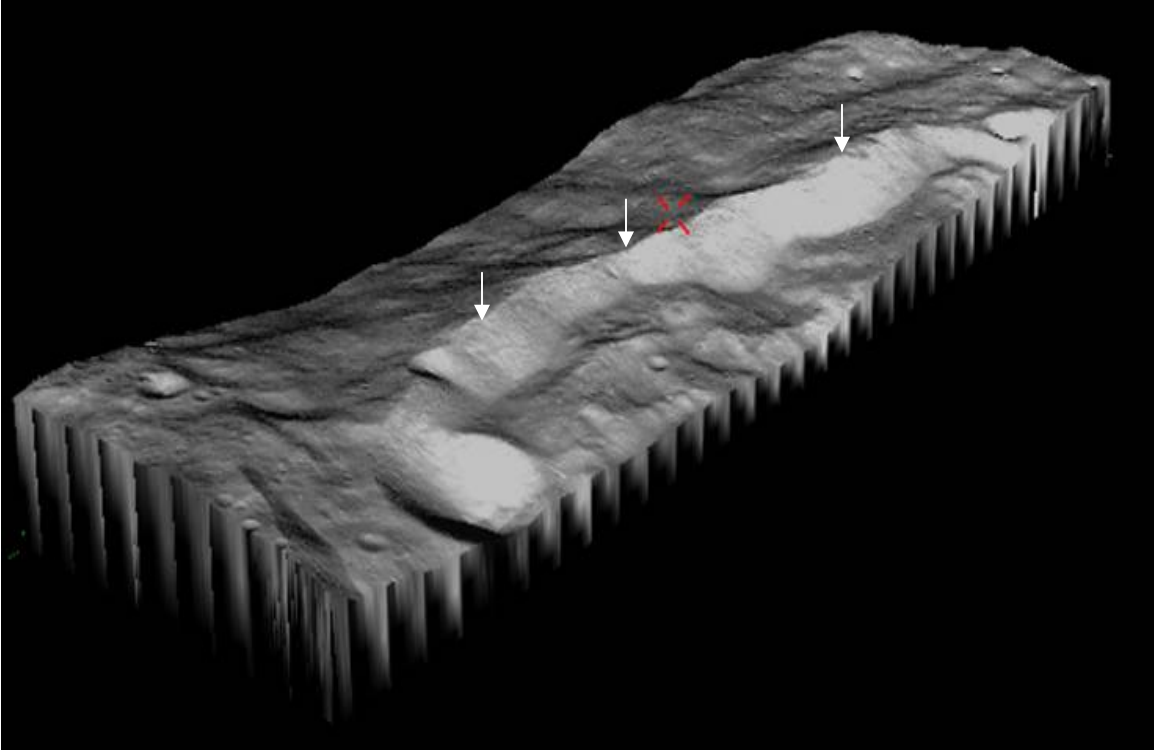


Fig. 6: 3D view of part of step faulted-rim of Moretus Crater - arrow shows the fault: (Near-side, 15 Nov 2008, TMC Image)

The multi-viewing capability of TMC (Fore- Aft-Nadir-) enables to estimate the depth and diameter of craters as shown in following profile (cross-section) of a crater (fig. 7).

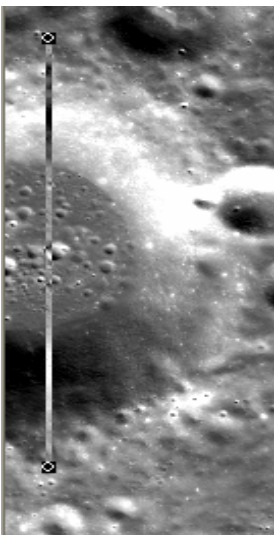
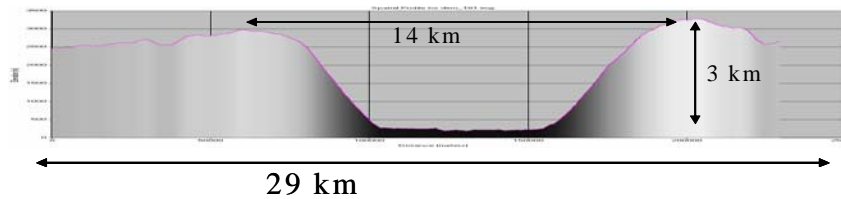


Fig. 7: Cross section profile of a crater displaying the depth and diameter of the Coulomb-A crater (Far side , 1.12.2008)



Consequentially the 3D view of TMC is used to generate DEM (Digital Elevation Model) of desired area or feature and a perspective view of the same is possible to generate as follows, which is useful in understanding the chronological ordering of the features and classifying them accordingly (fig. 8).

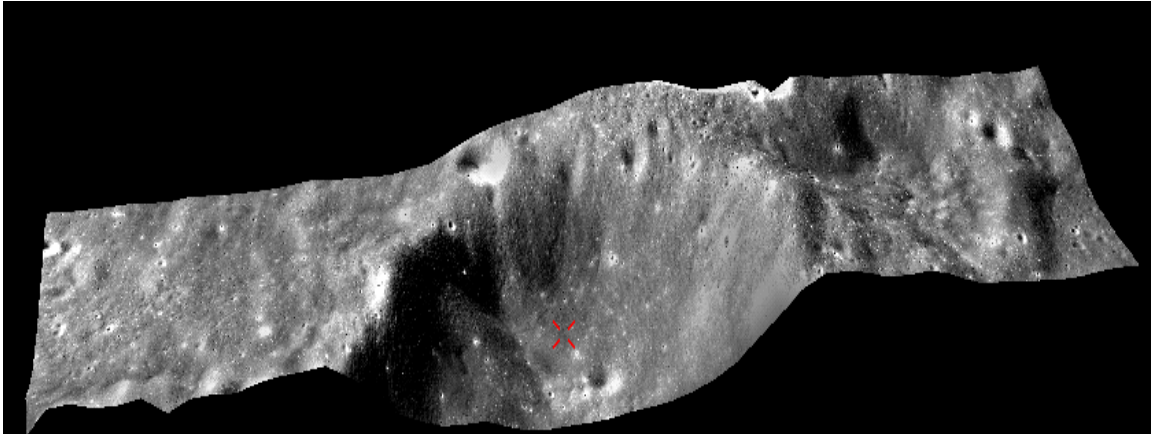


Fig. 8: 3D view of the Coulomb-A crater

The TMC DEM is also very useful as the ‘rider-data’ for other CHANDRYAAN-1 sensors, e.g. HySI data can be draped on the TMC DEM and thus a perspective view can be generated to understand the three dimensional spatial distribution of the mineral assemblages, and their relative proportions, in and around a crater (as shown below for Coulumb-A crater fig.9)

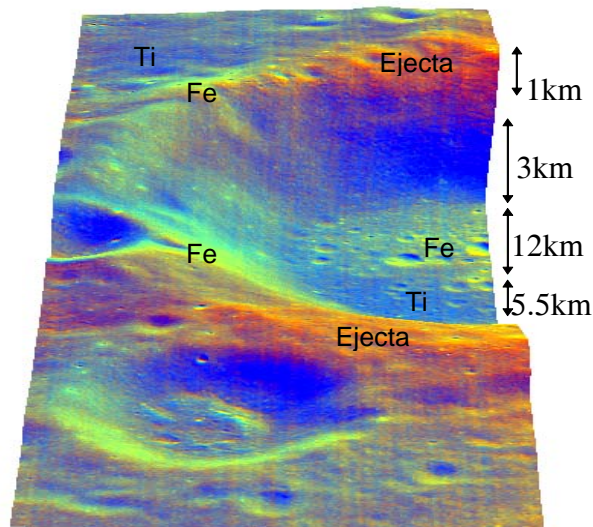


Fig. 9: Hysi data draped on TMC DEM for Coulomb-A crater

Thus a wealth of data set from TMC is available which could be mosaiced for entire Moon surface to map and understand the morpho- structural set up and the composition of the Moon inorder to address the scientific issues associated with the origin and evolution of the Moon and Earth-Moon system.

References:

[1] Kiran Kumar, A.S. et al. (2009), *The Terrain Mapping Camera on Chandryaan-1 and initial results. LPS XXXXI*, Abstract #1584.

Demo/Hands on exploration of Lunar Morphology with TMC PDS Data

R. Phani Rajasekhar
Space Applications Centre, Ahmedabad

(Tutorial topic: Planetary Exploratory Applications: Chandrayaan-1 TMC view,
By Shri Ashutosh Arya, MESG, RESA, SAC, 3rd Feb 2010)

Overview of course:

1. Brief introduction about the TMC data
2. Brief introduction about Lunar morphological features
Simple and complex craters, ray crater, Wrinkle ridge etc.
3. Brief description about TMC PDS data and loading of data in to ERDAS/ IGIS software.
4. Outline of applications of TMC - DEM in lunar morphological studies

1. Brief introduction about the TMC data:

Chandrayaan-1 is the maiden Indian planetary mission to the moon, realised by the state of art technology involving 11 different & complimentary sensors. One of the sensors, the Terrain Mapping Camera (TMC) has finest spatial resolution of 5 m and multi viewing capability, enabling 3 dimensional view of the Lunar surface.

TMC data with high resolution is extremely useful in mapping lunar morphological features in details.

2. Brief introduction about Lunar morphological features

Craters dominates all other landforms, which range in size. Shape and form change with increasing size (bowl shaped to central peaks to multiple rings). Few other land forms are Domes and cones; Faults and Graben; different types of rilles and wrinkle ridges. As TMC image having high resolution of 5m with a swath of 20 km, above features can be mapped in detail on fore, aft and nadir images. Then terrain variations of these features can be studied using DEM generated using TMC data. This will be help full in understanding morphological characteristics of the above features. Using TMC DEM depth and diameters of craters can be measured which will be use full in understanding depth to diameter relations in different basins of near side, farside and polar regions. Using Nadir

image of TMC, characteristics of features like types of rilles, wrinkle ridges can be mapped and terrain characteristics using DEM can be studied in detail. Study of diverse morphological features in will be useful in understanding lunar basins.

3. Brief description about TMC PDS data and loading of data in to ERDAS/ IGIS software.

TMC data can be visualized in image processing softwares i.e ERDAS / IGIS. Basically TMC data is provided in PDS format. Information about Date of pass, orbit, No of scan lines and pixels corner coordinates and file format can be obtained form *.LBL file. No. of scanlines and pixels of the image were also given in the first line of GRD (*.GRD) file. Longitude and latitude corresponding to every 100th scanline and pixels were provided in *.GRD file from the second line onwards. This file can be used in getting in location information in the TMC images, since Lon/Lat information corresponding to any scanline/pixel can be obtained from this file.

4. Outline of applications of TMC - DEM in lunar morphological studies

By using TMC DEM terrain characteristics of different lunar morphological features can be studied. Terrain variations across various features can be analysed using profile variations across the above features at different locations. Terrain variations in the adjacent areas of features can be studied using three dimensional perspective view, which will provide better understanding of morphological features than nadir image.

Hyper-Spectral Remote Sensing for Lunar Surface Composition

By

**Prakash Chauhan
MESG, RESA, SAC**

Email: [prakash@ sac.isro.gov.in](mailto:prakash@sac.isro.gov.in)

Remote Sensing of Lunar Surface composition using Chandrayaan-1 HySI data

Prakash Chauhan & Satadaru Bhattacharya
Space Applications Centre, Ahmedabad

1. INTRODUCTION

Moon is the most prominent object in the night sky and the only natural satellite of the Earth. From time immemorial, moon is familiar to humans. Moon is the nearest celestial body to Earth and lies at a distance of about 384,000 km from the Earth. It rotates around Earth once in 27.3 days and takes the same time to spin around its own axis. Thus, one hemisphere of the moon ('the farside') is not visible from Earth. In terms of diameter, moon is one fourth the size of Earth and its mass is 1/81 of Earth. Gravity on the surface of the moon is only one sixth of that on Earth. Like Earth, the moon too is a world with mountains, plateaus, plains, lowlands, and of course, craters. But, unlike Earth, the moon does not have an atmosphere. Formation and evolution of our moon are of importance in understanding the history of Earth-Moon system. After the dawn of the space age in October 1957, moon became the prime target of exploration partly due to its proximity to Earth. In September 1959, the Soviet Luna 2 hit the lunar surface while Luna 3 took the photographs of the far side of the Moon and transmitted them to Earth. In 1966, Luna 9 gently landed on the lunar surface. In the late 60s and early 70s, Soviet spacecraft brought back small soil and rock samples from the moon and landed Lunakhod-1 and 2 robotic vehicles on the lunar surface. Also during the 1960s, unmanned American Ranger, Surveyor and Lunar Orbiter spacecraft conducted detailed exploration of the moon. This was followed by successful human landing on the moon in Apollo spacecraft during 1969-72. A large amount of lunar rocks were brought back by different Apollo missions and these lunar samples were analyzed world over to provide insight into surface composition of lunar rocks and soils.

Over the last three decades, India has achieved a successful space program, and made big progress in design, development and operation of space systems as well as applications for telecommunications, television, meteorology, natural resource mapping and management. With the successful launch of Chandrayaan-1 on October 22, 2008 we are now in a position to develop lunar and interplanetary sciences and applications of remote sensing to understand evolution of our solar system and assessment of planetary resources. Chandrayaan-1 mission has carried eleven world class instruments to conduct investigation relating to mineral distribution, surface and sub-surface structures, elemental distribution and to characterize radiation environment around the Moon. One of the three hyperspectral cameras flown on Chandrayaan-1 mission is Hyperspectral Imager (HySI), which is developed at Space Applications Centre, Ahmedabad to map the lunar surface for mineralogical and morphological investigations at high spatial and spectral resolution. The HySI camera recorded reflected radiations of sun light from lunar surface in 64 spectral bands with a spatial resolution of 80 meters.

2.0 Major geology of Lunar Surface

The geology of the moon can broadly be divided into three types based on major mineralogy viz. Feldspathic Highlands Terrane (FHT), Procellarum KREEP Terrane (PKT) and Mare Basalts (MB). All the aforesaid terrains are characterized by intense cratering over the geologic time vastly modifying the lunar surface since its early evolution. Moreover, absence of atmosphere allows moon to directly interact with the space environment, causing changes in the physical nature of lunar materials. Moon basically acts as a laboratory for the study of processes that occur on all airless bodies. All geologic mapping and remote sensing techniques utilize only the outermost portion of the Moon. The data obtained remotely by the Galileo, Clementine, and Lunar Prospector missions, as well as data derived from lunar meteorites, have resulted in major changes to our understanding of global distributions of chemistry and rocks.

The lunar surface basically comprises of I. Lunar Regolith and Soils, II. Rocks and III. Minerals

- I. Lunar Regolith and Soils: Regolith is defined as the layer of fragmented, unconsolidated rock materials resulting from more than 4 billion years of impacts of meteoroids into the moon surface. The entire lunar surface consists of a layer of regolith except for some very steep-sided crater walls and lava channels, where bedrock may be exposed. Lunar soil refers to the finer grain size fraction (< 1-mm) of the regolith. The grain size of lunar soils range from 40 – 800 μm and averages between 60 and 80 μm. The lunar regolith comprises of fragments of igneous rocks, both intrusive and extrusive, crystalline impact-melt rocks, various types of crystalline and glassy breccias, meteorites and agglutinates Agglutinates are a special type of lithic component of lunar regolith that has resulted from micrometeoroid bombardment of lunar regolith at very high speed of 15 – 30 km/s.
- II. Lunar Rocks: Major rock types found on lunar surface can be divided into three broad categories: 1. Anorthositic Highlands crust, Mare Basalts and Procellarum KREEP Basalts. Following Ternary plot shows the rock types encountered on lunar surface.

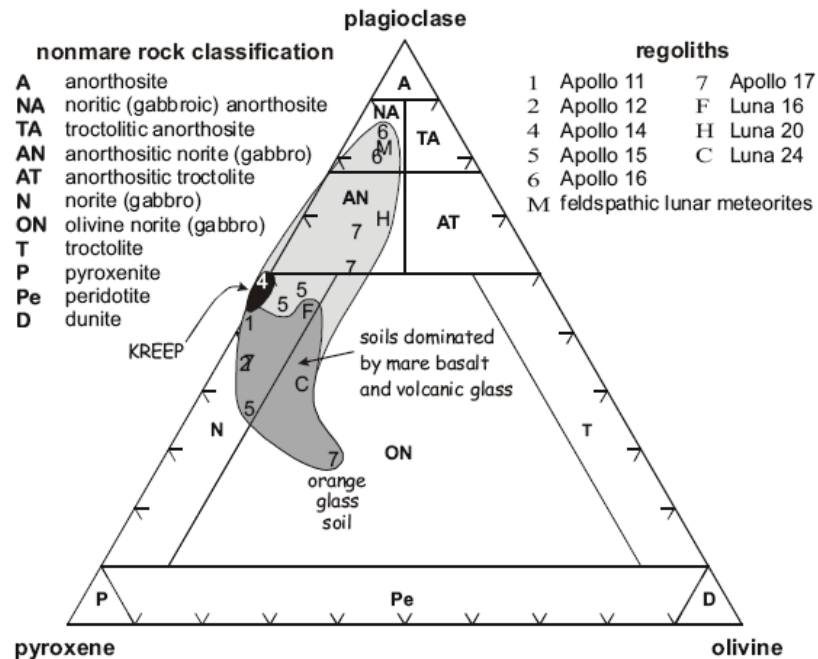


Fig. 1: Triangular diagram showing lithological variations in lunar crust

III. Lunar Mineralogy: Minerals have provided the keys to understanding lunar rocks because their compositions and atomic structures reflect the physical and chemical conditions under which the rocks formed. The array of minerals found in the lunar samples demonstrates strong differences between the Earth and Moon. The most common minerals found in the lunar samples are the silicates, namely, plagioclase feldspar $(\text{Ca,Na})(\text{Al,Si})_4\text{O}_8$, pyroxene, $(\text{Ca,Fe,Mg})_2\text{Si}_2\text{O}_6$, and olivine $(\text{Mg,Fe})_2\text{SiO}_4$. Potassium feldspar $(\text{KAlSi}_3\text{O}_8)$ and the silica (SiO_2) minerals (e.g., quartz) are rare on the Moon. Minerals containing ferric iron (Fe^{3+}) and carbonate (CO_3^{2-}) are absent on the Moon. The lunar mineralogy is also characterized by the lack of minerals that contain water, such as phyllosilicate clays, micas, amphiboles, and oxyhydroxides. These minerals may yet be found near the lunar poles where increased H concentrations occur. Next to the silicates are the oxides. They are mostly concentrated in the mare basalts. The most abundant oxide mineral is ilmenite, $(\text{Fe,Mg})\text{TiO}_3$, a black, opaque mineral that is the carrier of high TiO_2 concentrations of many mare basalts. The second most abundant oxide mineral, spinel, has a widely varying composition and actually consists of a complex series of solid solutions. Members of this series include: chromite, FeCr_2O_4 ; ulvöspinel, Fe_2TiO_4 ; hercynite, FeAl_2O_4 ; and spinel (*sensu stricto*), MgAl_2O_4 (Table 2.2). Another oxide phase, which is only abundant in Ti-rich lunar basalts, is a mineral first described from the Moon, armalcolite $(\text{Fe,Mg})\text{Ti}_2\text{O}_5$.

3.0 Reflectance characteristics of Lunar rocks and Minerals

The importance of reflectance spectroscopy of lunar rocks/soils lies in the fact that it provides an opportunity not only to understand the environmental features but also in the processing, analysis and interpretation of the original spectrum data. Moreover, based on study of reflectance spectra, specific bands sensitive to specific elements can be identified which in turn helps in determining various kinds of indices to map and quantify the lunar surface materials. As mentioned above, Lunar surface materials are generally composed of two major types of materials, i.e., lunar highland materials and lunar mare materials.

The most common rock-forming minerals on the Moon are feldspar, pyroxene, olivine, and ilmenite. The lunar mineralogy is characterized by absence of OH in the crystal lattice of the minerals and indicates a strong euxinic condition. Also, the minerals are relatively poor in alkali metals. The laboratory measured reflectance characteristics of some rock-forming minerals separated from the returned lunar rock samples are shown in Fig. 2.

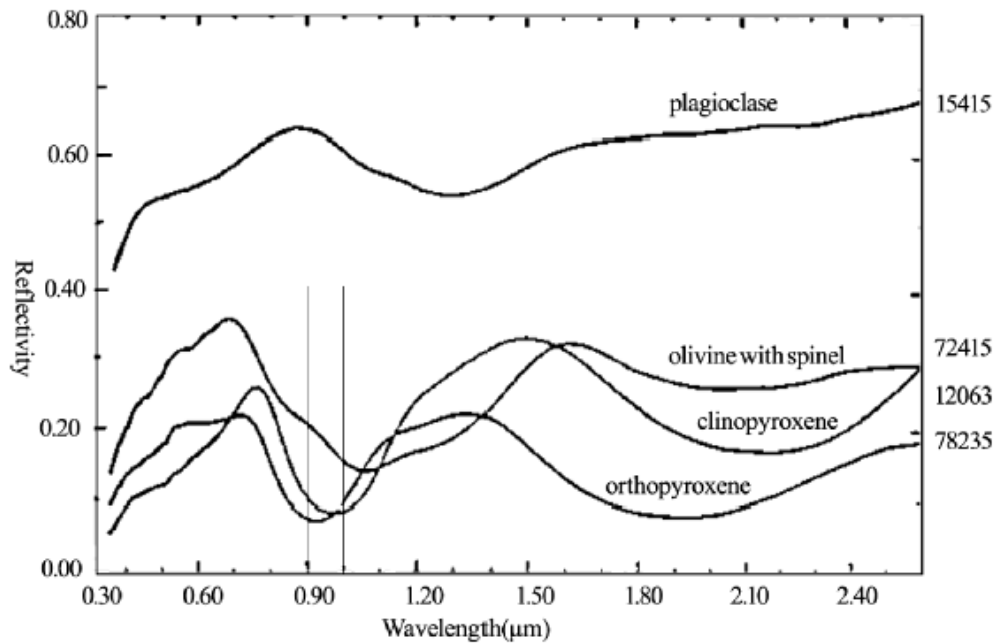


Fig 2: Reflectance characteristics of some lunar rock-forming minerals

The inferences drawn from figure 2 are as follows:

- (1) Lunar materials are mostly distinguished on the basis of presence of Mg-Fe minerals characterized by absorption features between 750 – 950 nanometers of EM spectrum in the NIR range. These absorptions can be attributed to the electron transition of ferrous ions in the specific lattice of the above mentioned minerals.
- (2) Experimental analysis shows that ferrous-ion free silicates are highly reflective and their spectrums are basically neutral. With increasing Fe^{2+} ,

an absorption peak will appear near 1 micrometer along with a marginal absorption peak toward the ultraviolet wavelength range.

- (3) It has also been studied that presence of some elements alter the spectral characteristics of host materials as is found in the case of injection of Ti in glass during maturation process due to micro meteoritic bombardment over Ti bearing lunar soil. Intensive charge transfer takes place because of existence of Ti in Fe^{2+} containing glass ($\text{Fe}^{2+} \longrightarrow \text{Ti}^{4+}$) resulting in darkening and reddening of spectra at 0.3 – 0.6 micrometer wavelength range.
- (4) Presence of nano-phase metallic iron Fe^0 resulting from space weathering also plays an important role in darkening and reddening of lunar soil. It weakens the spectral contrast and introduces an intense positive spectrum slope throughout the ultraviolet, visible and near-infrared wavelength ranges by obliterating Fe^{2+} and other absorption features.

Spectra of rock forming minerals have been used for generating major indices for discriminating various types of rocks. Lunar mare basalt contains abundant high-Ca pyroxene (> 50 %) with variable amount of olivine (0 – 20 %) thereby showing considerable variations in the spectra. Lunar highland rocks, on the other hand, comprise of mainly anorthosites, anorthositic gabbro and anorthositic norite characterized by different proportions of plagioclase feldspar (mainly anorthite) and different kinds of magnesiferous minerals. Presence of pyroxenes in norite and gabbro give rise to an absorption band between 0.9 to 1.0 micrometer and peak wavelength of absorption varies with varying degrees of Fe, Mg and Ca. Highland rocks are also composed of dunite and troctolite containing olivine and characterized by broad multi-absorption bands near 1.1 micrometer. The main mineralogical compositions of KREEP are same as that of highland anorthosite with minor difference in content and therefore exhibit spectral characteristics close to those of anorthosite.

4.0 Spectral reflectance studies using HySI data

Optical, ultraviolet and infrared remote sensing of the Moon has a venerable history, beginning with Wood (1912) who discovered significant variations in the visible and ultraviolet characteristics of the lunar surface. A host of techniques has been applied using ground-based telescopes; the most scientifically fruitful of these for compositional mapping have been spectroscopy and multispectral imaging in the region of solar reflectance from 0.4 to 2.5 microns. Spectral reflectance measurements of the lunar surface are sensitive to the mineralogy, mineral chemistry, and physical state of the regolith, including the important optical effects of space weathering.

The foundation for remote compositional analysis lies in optical absorption physics and the linking of spectral properties of materials measured in the laboratory to well-understood mineral species and their mixtures. The pioneering work by Burns (1970), Hapke et al. (1970), McCord and Adams (1973), McCord et al. (1981), and others amply demonstrated the potential of spectral reflectance measurements for understanding lunar materials. Following this initial era, a diverse set of remote-sensing investigations made significant progress in understanding the distribution of mare and highland materials. Mare studies using spectroscopy and multispectral imaging produced maps of a diverse suite of mare basalts, including unsampled types, pyroclastic deposits and the abundance of Ti. Spectroscopy of the lunar highlands uncovered a spectral diversity that mirrors the diversity found in the pristine rock collection, but occurs in vast exposures that the tiny fragments found in the Apollo collection did not anticipate.

Techniques and methodologies developed during the 1970's and 1980's for lunar spectral analysis provided the foundation for understanding of the new mission data, such as using observations of craters of all sizes to probe beneath the regolith, and inferring the abundance of Ti from lunar color. These and similar approaches benefit from three key characteristics of the Clementine data set: global reach, high spatial resolution, optimal band passes, and data uniformity. The value of global

data is obvious; studies previously confined to the lunar near side can now be conducted globally. High spatial resolution enables entirely new studies, such as examination of compositional properties of individual lava flows. The Clementine band passes were chosen to characterize the major features in the spectra of lunar rock-forming minerals. Data uniformity in terms of calibration and photometric correction enable confident comparison of radiometric and derived compositional information Moon-wide and provide access to new quantities such as albedo to be applied more confidently. Continuing studies of lunar samples, especially the regolith, have provided new understanding of lunar soil formation processes and effects that strongly influence the ability to glean information from the Moon remotely.

A major step toward a global assessment of lunar surface chemistry was provided by analysis of spectral reflectance data returned by the Clementine mission. Comparison of the spectral reflectance properties and chemical compositions of lunar soils returned by the Apollo and Luna missions, and remote measurement of the spectral properties of the Apollo and Luna sample collection sites by Clementine, led to the development of algorithms that derive the abundance of FeO and TiO₂ from spectral properties of lunar soils and surface units with 1 to 2 weight % accuracy. By applying these algorithms to HySI images with minor modifications, it has been possible to infer the abundance of FeO and TiO₂ both quantitatively as well as qualitatively within $\pm 80^\circ$ latitude at resolutions approaching 80 m.

The basic goal of present tutorial is to generate reflectance spectra of selected lunar surfaces using HySI data and to map various mineralogical/lithological entities present therein. A reflectance spectrum is essentially a measure of how much radiation incident on a surface (solar radiation) is reflected and how much is absorbed at each wavelength. Moon is basically represented by various shades of red when viewed through photoelectric instruments and the redness increases with wavelength. In the near-infrared there

are absorptions diagnostic of minerals superimposed on the Moon's redness. For the Moon, and other rocky bodies such as asteroids, most of the detectable absorptions arise from ferrous iron in various crystallographic sites. The wavelength, shape, and strength of these absorptions identify the minerals present, and allow their abundances to be estimated.

To accurately measure these diagnostic mineral absorptions with remote detectors requires not only a quality instrument, but also excellent electronic calibration and either direct measurement of the light source (the sun), or a proxy, or a well known reference standard illuminated by the same light source. In the laboratory a white reference such as halon is used (or commercial Spectralon), which in turn has been extensively calibrated relative to a known radiance.

The level 1b HySI scenes over selected lunar surfaces have been corrected by converting the scaled radiance to reflectance unit (each pixel is presented by reflectance value) using the following equation (1).

$$\rho_{\lambda} = (\pi * d^2 * L_{\lambda}) / (E_{0\lambda} * \text{Cos } \theta_s) \dots \dots \dots (1)$$

Where, d is moon-sun distance correction (1.00901 Astronomical Units), θ_s is Solar zenith angle, L_{λ} is Radiance as a function of wavelength, $E_{0\lambda}$ is Exo-atmospheric solar spectral irradiances. To further improve the reflectance values generated using equation (1), normalized exo-atmospheric solar spectral irradiances have been calculated using Relative Spectral Response (RSR) function of the sensor as is given by equation (2).

$$\langle E_{0\lambda_i} \rangle = \int E_{0\lambda_i} * RSR_{\lambda_i} d\lambda / \int RSR_{\lambda_i} d\lambda \dots \dots \dots (2)$$

Where, RSR_{λ_i} is the relative spectral response function for the i^{th} band, $d\lambda$ is the bandwidth, λ is the central wavelength.

In the present study, three HySI bands viz. 450 nm, 747 nm and 948 nm have been used for generation of ratio images. Ratio of 430 nm to 748 nm is sensitive for mapping Titanium. Similarly, ratio of 747 to 948 has been used for iron mapping and ratio of 747 to 430 basically shows the presence of plagioclase feldspar and/or ejecta material. Another important parameter known as optical maturity or OMAT has also been studied using ratio of 948 nm to 747 nm and reflectance at 747 nm. This parameter shows the degree of maturity and relates to the exposure age of the surface under observation. Higher the OMAT value, fresher is the surface. The spectral ratio is controlled by both composition and maturity. Colored plate 1 shows example of reflectance spectra obtained from the Chandrayaan-1 HySI data. In the tutorial session a similar exercise will be undertaken to analyze the HySI data and to generate the spectral signatures of the various geological features of the Moon surface.

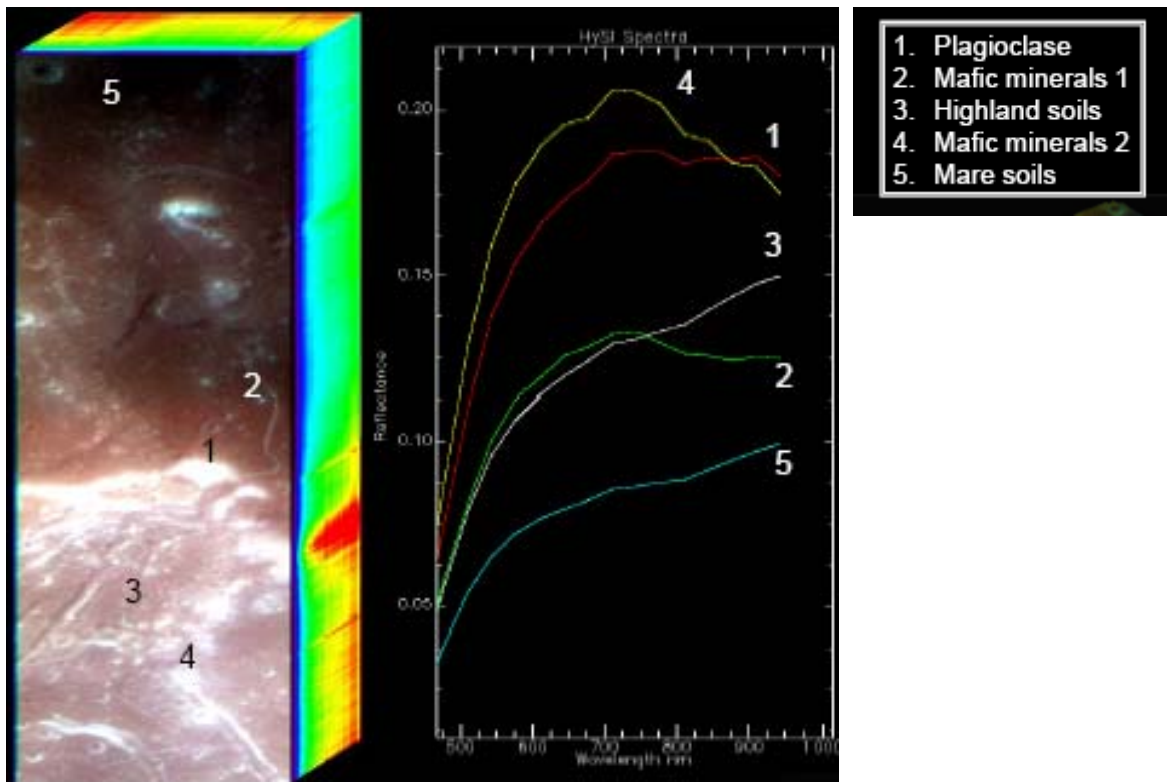


Plate1: Spectral signatures of Lunar rocks using HySI data for Part of Mare Orientale

Tutorial on HySI & M³ PDS data analysis towards mineralogical applications


Satadru Bhattacharya

Space Applications Centre, Ahmedabad

Outline:

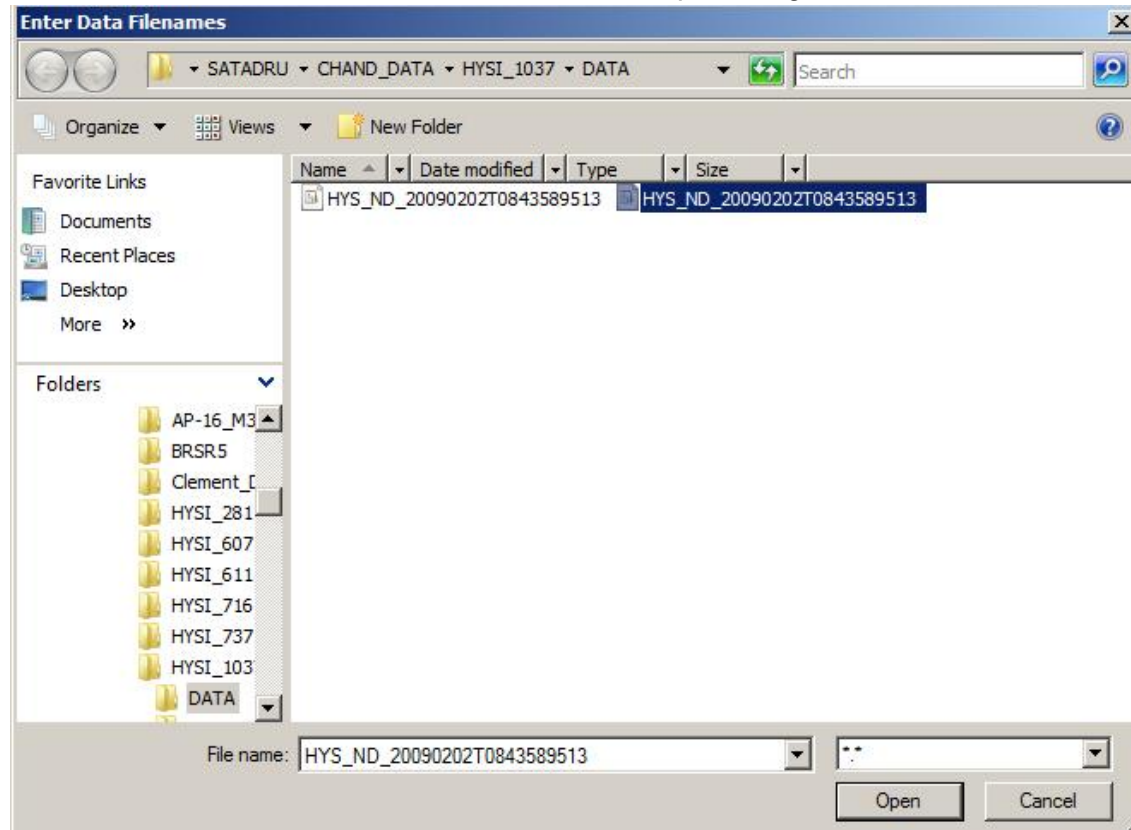
- **Loading of Level 1B HySI PDS data in ENVI**
- **Radiance to Reflectance Conversion**
- **Generation of basic image statistics**
- **Generation of Region of Interest (ROI) and ROI statistics**
- **Extraction of spectral profile from image**
- **Creation of data cube**
- **Band Ratioing**
- **Generation of Ratio FCC**
- **Study of spectral signatures of various lunar surfaces**
- **Examples from HySI & M³**

- **Loading of Level 1B HySI PDS data in ENVI**

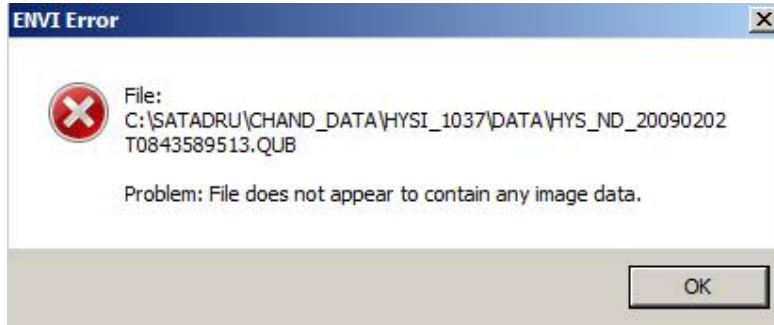
1. Double click on ENVI  icon
2. ENVI main menu bar will open



3. From the ENVI main menu bar, select **File** → **Open Image File**

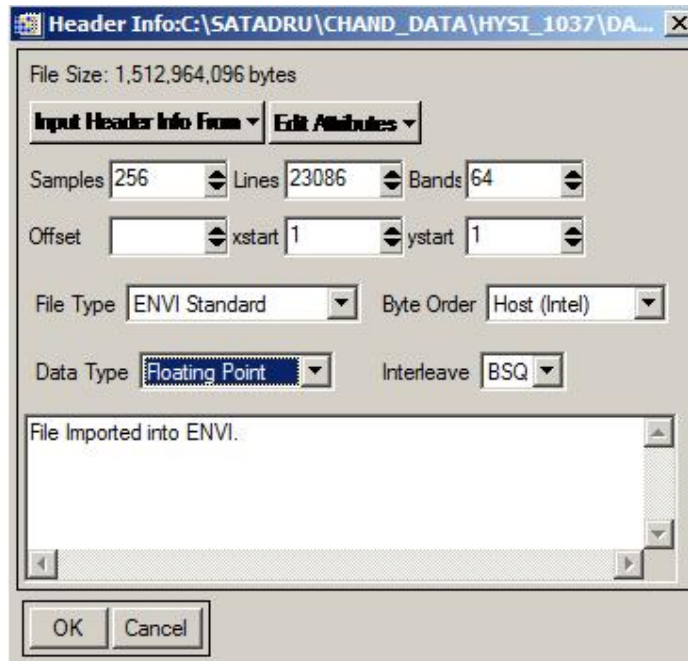


4. Navigate to the folder where HySI data have been copied and select the *.QUB file
5. Click the Open button
6. ENVI error message will be displayed



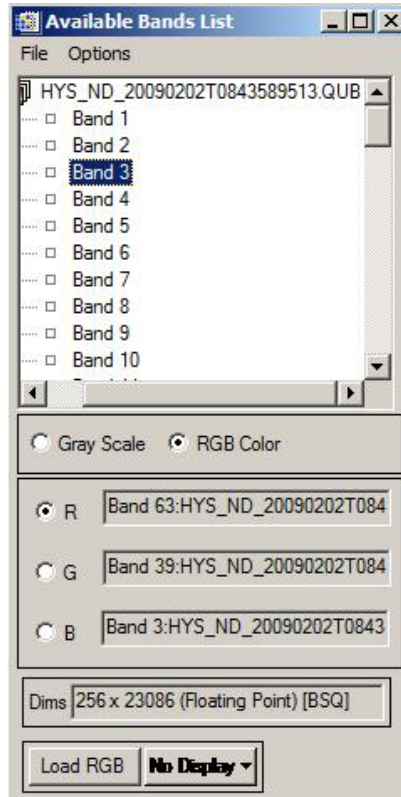
7. Click OK button

8. Header Info dialogue box will open

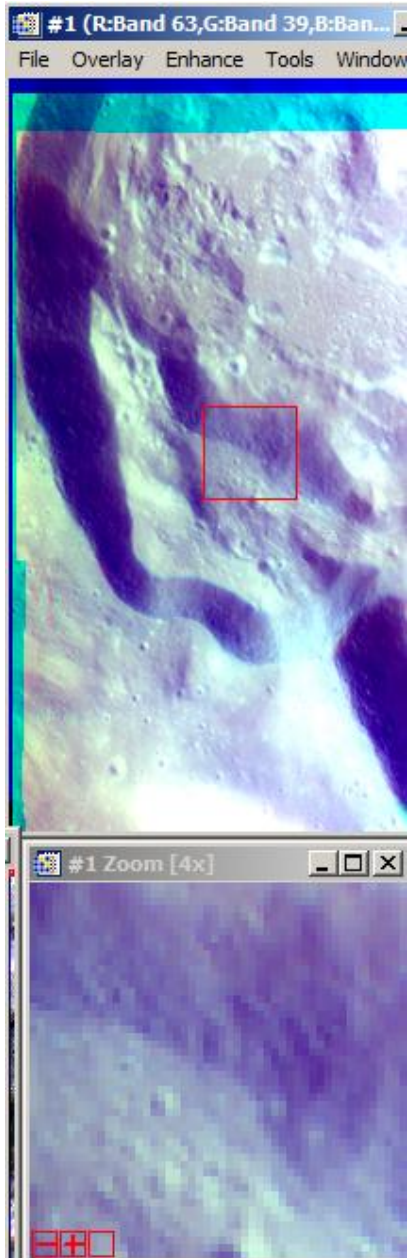


9. Specify the no. of samples, lines and bands and specify the data type as Floating Point. The default data type is Byte. Click OK button

10. Available Bands List dialogue box will open



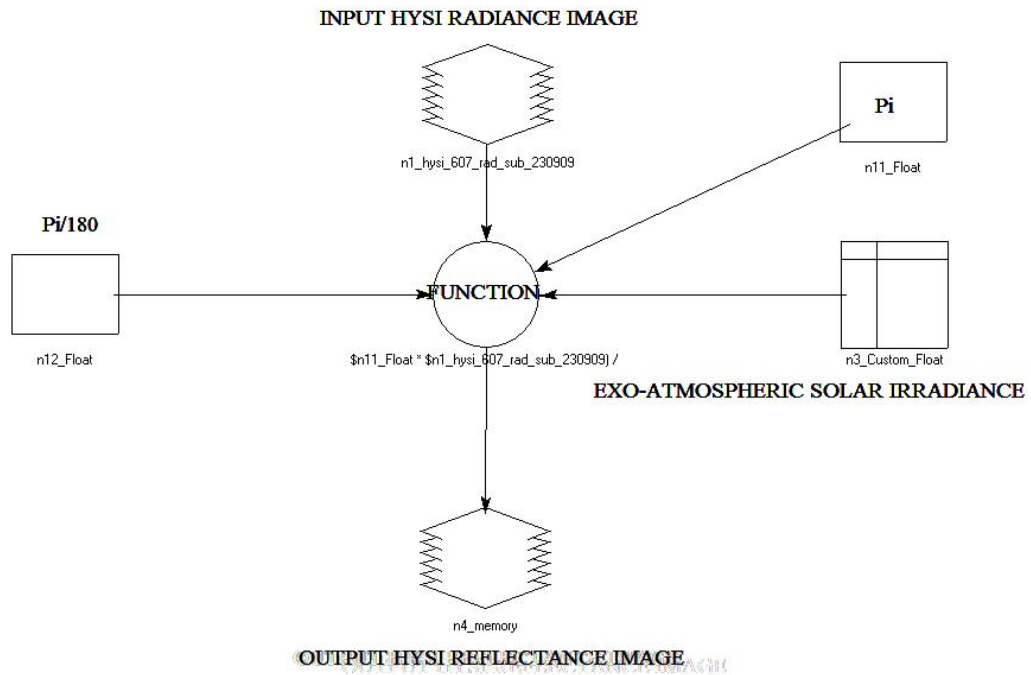
11. Check in the RGB Color button and select band nos. 63, 39 and 4 as R, G and B respectively
12. The image will open in 3 windows, namely, Image window, Scroll window and Zoom window



- **Radiance to Reflectance Conversion**

1. Open ERDAS Imagine and import the image into ERDAS Imagine s/w
2. Open the Model Maker module from main menu bar
3. Create a model for conversion of radiance to reflectance

The model comprises of one input raster object, two scalar objects, one table object, one function object and one output raster object



Inside the Function circle specify the function as under

$$(\$n11_Float * \$n1_hysi_607_rad_sub_230909) / (\$n3_Custom_Float * \text{COS}(30 * \$n12_Float))$$

$$(pi * \text{input image}) / (E_{\text{not}} * \text{COS}(\text{Solar Zenith Angle} * pi/180))$$

In the Model Maker menu bar, click process and then click run to execute the model. The resulting output image is a reflectance image

Indian Space Science Data Centre (ISSDC)

By

**J. D. Rao
DGM, ISSDC, ISTRAC**

Email: [jdrao@ istrac.org](mailto:jdrao@istrac.org)

**Indian Space Science Data Center (ISSDC)
ISRO’s Archive center for Space Science Missions of India**

J.D. Rao
DGM, ISSDC, ISTRAC

Abstract:

In the space science discipline especially in the planetary and deep space research, the data collected from the satellite missions plays an important role in the understanding of universe. In order to cater the needs of scientific community especially space science community there is a great importance to the data storing, archiving and dissemination facility called Science Data Center.

Indian Space Science Data Center (ISSDC) is one such national facility established in the premises of IDSN as part of CHANDRYAAN-1. ISSDC has played a major role in the operations of India's first unmanned mission and has received more than 3 TB of raw data. This center has the responsibility of successful Data ingest, archive and dissemination to the team Principal Scientists involved in the mission and to the other scientific community. It has also carried out various levels of data processing required for the successful scientific analysis of the data. In chandrayaan-1, ISSDC has played very crucial in helping to find water on the moon. There are many such successful findings are behind the role of data center.

1. Introduction

Indian Space Science Data Center (ISSDC) is the primary data center for the payload data archives of Indian Space Science Missions. This data center is located in the IDSN campus, Byalalu village near Bangalore. This center is responsible for the Ingest, Archive, and Dissemination of the payload data and related ancillary data for Space Science missions like Chandrayaan (CH1), Megha-Tropiques (MT), YouthSat, and Astrosat etc. The primary users of this facility will be the principal investigators of the science payloads. In addition to them, the data will be made accessible to scientists from other institutions and also to the general public. The facility started its operations with the support for Chandrayaan-1 and ready to support Megha-Tropiques, AstroSat and other missions.



Fig. 1. Indian Space Science Data Center

ISSDC facilitates the data flow between ISSDC and other tracking stations. The Spacecraft Control Center (SCC) located at Peenya, Bangalore controls all the S/C operations and the generation of the ancillary data. The ancillary data is transferred to ISSDC archives for storage and dissemination.

The raw payload data received through the data reception stations is transferred to ISSDC and further processed to generate Level-0 and Level-1 data products which are stored in the ISSDC archives for subsequent dissemination.

Raw payload data / Level-0 data/ Level-1 data for each science payload is transferred to the respective Payload Operations Centers (POC) for further processing, analysis and generation of higher level data products. The higher level data products generated by the POC's are subsequently transferred to ISSDC archives for storage and dissemination. ISSDC also hosts long term archival of the data from all the space science missions.

ISSDC hosts several suites of software for implementation of Ingest, Archive, Data processing, and data dissemination functions. Some of the suites of the software are developed by mission teams / mission software development teams in the different centers of ISRO, while some are developed by the principal investigator's teams / payload development teams. These software development teams interact with ISSDC for delivery and implementation of software, fault resolution, and change management. ISSDC provides dedicated services for supporting the software maintenance life cycle for the software used by ISSDC. Towards this, ISSDC provides the infrastructure support for the change / configuration management of the software.

Principal investigators are the primary users of the data archives for science research. They have exclusive access to the payload data for a defined

period before the data is made available to public users. ISSDC assigns high priority in its resource allocation for meeting the requirements of the principal investigators. After a pre-specified lock-in period for the data, ISSDC makes the data available to public users (if required). Such users can access the data archives through the Internet.

The dissemination of data generated at ISSDC to the payload operations centers / principal investigators, scientists and general public is supported through private WAN connections and Internet. The security mechanisms of the ISSDC archives and its interface to the SCN is assured by isolating them from the ISSDC data dissemination infrastructure through custom designed gateways and strong network security mechanisms.

ISSDC supports a large data archive capable of providing online access to any of the data sets in the archive according to the ISRO policy. To facilitate the science investigation, ISSDC is capable of supporting data network connectivity through secure gateways to a number of premier science institutions in India and abroad.

2. ISSDC facilities

The primary facilities for ISSDC are being established at the IDSN site at Bangalore. Integrated with the Telemetry complex at IDSN, the SDC operations facility provides the infrastructure facilities (Civil, Electrical, environmental..) for ISSDC support. This facility supports the computing, storage and network systems for supporting the data ingest, long term archive, data center operations, and the network connectivity to the external entities. This facility supports the work-areas for the ISSDC operations teams to carry out the operations tasks for problem resolution in the automated processes, Quality assurance, data product generation, data management, dissemination support, and system management. This facility also supports the work-areas for the software developers to install, test and commission the software for ISSDC support.

Data processing centers of principal investigators, Mission teams, S/W developers and payload Operations centers involved in ISRO Space science missions interface with the Operations facility through private network connections for data interchange and workflow coordination. Principal investigators, Science working groups, S/W developers, Mission teams, Payload developers can access the data archives either through local access support or through the remote access support.

To assure availability of archives in case of disaster scenarios affecting the IDSN site, a disaster backup facility is planned to be established later. The disaster backup facility is expected to be connected to the primary facility through high speed, low latency communication links.

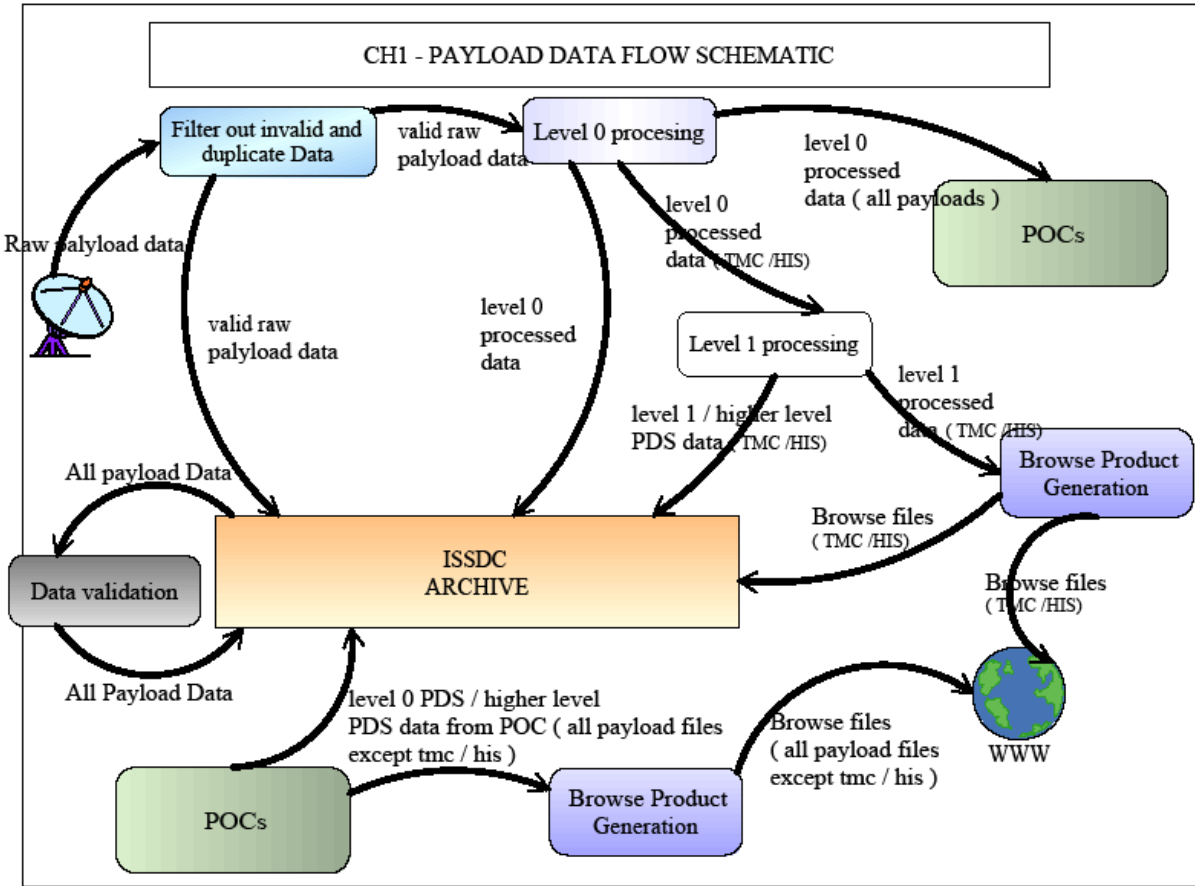
The primary technical areas of ISSDC at IDSN site are the Server & Storage area, Network area, Software & System Support area and Operations Area.



Fig. 2. Indian Space Science Data Center

3. ISSDC Support for Chandrayaan-1

A detailed automated workflow management work flow pattern was defined and executed for the Chandrayaan I mission. The automated processing supports data reception, data ingestion, data processing, data dissemination along with the computer and infrastructure health monitoring. The data from the ground stations termed as ‘raw data’ are received at ISSDC, any invalid /duplicate data are filtered at ISSDC before being archived. The raw data are provided supplied for offline qld display and level 0 processing at ISSDC. The level 0 processed files are disseminated to the POC. The level 0 files are also ingested by level1 software for HIS and TMC, which generates the level1 products of TMC and HIS payloads of Chandrayaan 1. A simple schematic of the data flow at ISSDC is shown in the diagram.



4. Chandrayaan -1 data harvesting payloads

Chandrayaan-1 has carried 11 payloads onboard out of which, the Indian payloads are TMC, MIP, HYSI, LLRI and HEX. The remaining are Announcement of Opportunity payloads (AO P/L) namely C1XS, SIR2, MiniSAR, MMM, RADOM, SARA. The payloads C1XS and SARA are collaborated projects with ISRO and foreign space agencies. All these payloads are successfully commissioned and data has been harvested throughout the mission period. A huge amount of nearly 2.5TB of Raw data has been collected and stored at ISSDC.

Optical imaging camera:

4.1 Terrain Mapping Camera (TMC):

Main objective of this camera is to make a 3 D Atlas of moon with spatial resolution of 5m, ever made in the lunar exploration till the Chandrayaan-1 mission life. The camera has 3D view of Fore, Nadir and Aft which enables 3 D coverage of Moon. TMC have three linear 4K Active pixel sensors having one port with 12 bit pixel depth. The camera supports a ground resolution of 5 meter. The total swath provided by TMC is 20Km. The payload is

Commissioned on 16 Nov 2008. Raw Data Received during the operational period accounts to 1.2 Terra Bytes.

This instrument is designed and developed by Space Applications Center SAC , Ahmadabad. A POC- Payload Operation Center is established at Ahmadabad for Scientific and image analysis. At ISSDC also similar arrangements are made for higher level image processing.

This instrument has attracted people of its unique facility of Quick Look Display (QLD) at ISSDC and has played significant role in popularizing the terrain of moon to the common man.

4.2 Hyper Spectral Imager (HySI):

Main objective this camera is to create mineralogical map of moon. HySI is a multi-spectral resolution camera and has 64 continuous bands in the spectral range of 0.4 to 0.95 μ m. Spectral resolution is obtained through wedge filter method. Camera is developed around 256 x 512 Area array APS, with 256 pixels in across track and 512 pixels mapped to 64 bands. Integration time of the camera is 51.78ms and has a ground resolution of 80m at 100km lunar orbit. Total swath support by camera is 20km. This payload is commissioned on 16 Nov 2008. Raw data received during operational period is 386GB.

This instrument is designed and developed by Space Application center, Ahmadabad. A POC –Payload Operation center is established at Ahmadabad for Scientific and Image analysis. At ISSDC also similar arrangements are made for higher level image processing.

This instrument has attracted people of its unique facility of Quick Look Display (QLD) at ISSDC and has played significant role in popularizing the terrain of moon to the common man.

4.3 Moon Mineralogy Mapper (M³):

The sensor has prime objectives of assessing mineral resources, characterize and map the composition of the moon surface at high spatial resolution. M³ will extend spectral range of HySI into the near-infrared 0.7 to 3.0 μ m. The Spectral and Spatial resolution is around 10nm and 30 meters respectively. Total Swath of the M³ is 20 Km. This payload is Commissioned on 18 November 2008. Raw Data Received during the operational period accounts to 439 Giga Bytes

This Instrument is designed and developed by JPL-NASA. A POC is established by NASA to which the data of this instrument received at ISSDC is delivered for higher Scientific analysis.

This instrument data also can be visualized with QLD facility.

4.4 Smart Infrared Spectrometer (SIR-2):

SIR-2 is a near-infrared spectrometer that covers wavelength range of 0.93 to 2.4 μ m having spectral resolution of 6nm. Instrument has two units named as (i) Optical box and (ii) Electronic Box. The information collected from optical box is passed to Electronic box through a fiber link. Electronic box digitizes the data and sends it to spacecraft data bus. This payload is commissioned on 19 Nov 2008. Raw Data Received during the operational period accounts to 11 Giga Bytes

This instrument is designed and developed by European Space Agency. At ESA, a POC is established and entire data received at ISSDC from this instrument is disseminated to the ESA Principal Investigator for Scientific Analysis.

X-Ray Sensor:

4.5 Collimated low energy X-ray spectrometer CIXS2/XSM:

The function of CIXS2/XSM is to provide a high quality X-ray spectroscopic mapping of the moon, in order to constrain key questions on the origin and evolution of the moon. It is a low energy X-Ray spectrometer and has multiple scientific objectives. The Sensor of CIXS2 is developed using SCD and they are located at three facets of the instrument. XSM has been included along with CIXS2 to monitor continuously the solar X-ray flux that excites the lunar emission.

This is Commissioned on 20 Nov 2008. Total Raw Data received during mission period accounts to 7.5 Giga Bytes.

This instrument is designed and developed by RAL-United Kingdom in collaboration with ISAC, ISRO. This instrument data can be viewed through QLD facility.

The entire data collected from this instrument is disseminated to the PIs and other co-PIs.

4.6A High energy X-ray spectrometer (HEX):

The primary objective of the HEX payload is to determine the surface composition of naturally occurring Pb-210 in the uranium decay series by its 46.5 Kev gamma ray. The other objective is determining the integral flux of gamma rays coming out of the moon in the energy region (10-250 Kev). This payload is Commissioned on 5 December 2008. Raw Data Received during the operational period accounts to 2 Giga Bytes.

This Payload is designed and developed by ISRO-ISAC and PRL. It also has the QLD facility to have first look at the quality of data.

The entire data received by HEX is disseminated to PIs at ISAC and PRL.

Radiation Monitoring Sensor:

4.7 Radiation Dose. Monitor (RADOM):

RADOM instrument will qualitatively and quantitatively characterize, in the terms of particle flux, dose rate and deposited energy spectrum, the radiation environment in near-Moon Space. This is the only instrument powered on immediately after the launch and continuously powered on throughout the mission life. This instrument is fully Commissioned on 20 November 2008. Raw Data Received during the operational period accounts to 3 Giga Bytes.

This instrument is designed and developed by Bulgarian Academy of Sciences. The data of this instrument can be see using the QLD facility.

The entire data collected is disseminated to PI at Bulgaria and Co-PI at ISAC.

4.8 Sub-Kev Atom Reflecting Analyzer (SARA):

SARA subsystem has two sensors and a Data Processing Unit (DPU). The Sensors named Chandrayaan-1 Energetic Neutrals Analyzer (CENA) and Solar Wind Monitor (SWIM) are connected to Spacecraft through DPU. SARA will image the moon surface using CENA in the energy range of 10ev – 2 keV. CENA sensor is composed of four units (i) charged particle deflector (ii) ionization surface (iii) electrostatic analyzer and (iv) Time of flight section. SWIM is an optimized ion mass analyzer that provides monitoring of the precipitating ions. This instrument Commissioned on 8 December 2008 (for SARA LV), and 8 January 2009 (for SARA HV). Raw Data Received during the operational period accounts to 5 Giga Bytes

This Instrument is designed and developed by group of nations (Japan, Sweden, India) with SPL as lead center. Quick Look of data of this instrument also is arranged at ISSDC.

The entire data received from this payload is disseminated to SPL POC :

4.9 Moon Impact Probe:

Impact probe as name suggest will impact on moon after being separated out from Chandrayaan-1 satellite. While de-orbiting, it sends photographed images of moon, information on altitude profile of lunar atmospheric constituents including ion composition and radar altimeter data. Released on 14 November 2008. This activity has attracted wide spread popularity for the Chandrayaan-1 mission as it painted our National Flag on the South pole of the Moon. Data Received and processed during the operational period accounts to 16GB (images ,movies)

This probe is designed and developed by VSCC, ISRO. All the data received immediately after the release is analysed and the images are released to public. The scientific data is handed over to the PIs of MIP for further Scientific analysis.

5 Data Processing Support for Chandrayaan-1

5.1 Level 0 Processing:

All valid raw files received from ground station have been supplied for Level 0 processing. The level 0 generates a tar file (for every session dump ingested).

The level 0 processed tar set file consists of the following files

- Payload Files
- Ephemeris File
- Attitude File
- SClock File
- Hk File
- Orbit number File

All the raw files received from the ground stations have been successfully ingested by the level 0 software and level 0 products has been generated for all the raw files ingested . The tar files generated by level 0 software are archived safely at ISSDC and the same has been delivered to POC .

5.2 Level 1 product generation:

The level 1 PDS products for TMC and HySI are generated at ISSDC and archived at ISSDC.

For Every level 0 tar file ingested by the level 1 software, Image cube QUB and Label LBL files are generated in PDS format and are archived at ISSDC. The correlation of Level 1 files with the raw file sessions and level 0 files are carried out as and when the level 1 files are available at ISSDC.

5.3 Browse products Generation:

The browse products of TMC and HySI are generated at ISSDC. This enables users to submit work orders for data and collect the same over internet. For every level 0 processed file corresponding level 1 files and browse files are generated

All the browse products generated by the level 1 software are preserved safely at ISSDC and are correlated with level 0 files ingested.

5.4 Other Higher products: All higher level products generated for TMC and HySI are archived at ISSDC as and when the products are delivered to ISSDC.

6. Data Backup

The file system for the data ingestion and archival is QFS(Quick File system) on both Solaris and Linux Platforms. QFS file systems are configured to archive and to take backup of all payload data of Chandrayaan-1. The data of Chandrayaan-1 is available at ISSDC as raw data, level0 data and level1 data. The policy for backup is such that, no data of any form is lost and also to ensure the high availability of data at ISSDC. The data is archived in a 3 tier Hierarchical storage Management System(HSM). Primary copy (archived) resides on 9990V storage system. The copy 1 is stored in SATA 6540 storage system as hard disk data backup. Copy2 and copy 3 are taken in to SL8500 as tape backup in LTO4 tapes and in T10K tapes.

All these three types of data backup is successful and data is intact. There is well defined and user friendly procedure available at ISSDC to retrieve data from these backup copies.

Following table gives about the overview of pay load wise data size and backup status

Pay-Load wise Data Status and Backup						
PL	RawData	BackupCopies 3Nos	Level0DATA	BackupCopies3Nos	Level1DATA	BackupCopies 3Nos
TMC	1.2960TB	YES	7.562TB	YES	183GB	YES
HIS	386GB	YES	1.0107TB	YES	156GB	YES
MMM	457GB	YES	548GB	YES	774GB	Progress
MSR	188.861GB	YES	124.152(gzipped)	YES	NO DATA	NA
MIP	623.2MB	YES	18GB	YES	NA	NA
LRI	2.296GB	YES	42.1GB	YES	NO DATA	NA
RDM	2.634GB	YES	150.7GB	YES	NO DATA	NA
SRA	4.730GB	YES	333.265GB	YES	NO DATA	NA
SIR2	10.174GB	YES	109GB	YES	NO DATA	NA
CXS	7.681GB	YES	151.1GB	YES	NO DATA	NA
HEX	1.964GB	YES	22.425GB	YES	NO DATA	NA
Total	2.332TB		10.0187TB			

Conclusion:

During the Chandrayaan mission, ISSDC has played a significant role in providing the services with respect to the data ingest, archive, processing and dissemination. Other value added services such as Support to the Payload community during the mission initial phase, generation of visual products, and other need based mission demands. Plans are under progress to make the entire Chandrayaan data available to the general public through designated website by ISSDC.

Planetary Remote Sensing of Energetic Particles and Photons

By

**Debabrata Banerjee
PRL**

Email: deba@prl.res.in



Contents lists available at ScienceDirect

Planetary and Space Science

journal homepage: www.elsevier.com/locate/pss

The C1XS X-ray Spectrometer on Chandrayaan-1

M. Grande^{a,*}, B.J. Maddison^b, C.J. Howe^b, B.J. Kellett^b, P. Sreekumar^c, J. Huovelin^d, I.A. Crawford^e, C.L. Duston^f, D. Smith^g, M. Anand^h, N. Bhandari^j, A. Cook^a, V. Fernandes^l, B. Foing^o, O. Gasnaut^f, J.N. Goswami^j, A. Holland^h, K.H. Joy^{b,e,i}, D. Kochney^o, D. Lawrence^k, S. Maurice^f, T. Okadaⁿ, S. Narendranath^c, C. Pieters^p, D. Rothery^h, S.S. Russellⁱ, A. Shrivastava^c, B. Swinyard^b, M. Wilding^a, M. Wiczcerek^m

^a Institute of Mathematical and Physical Sciences, University of Wales, Aberystwyth SY23 3BZ, UK

^b Rutherford Appleton Laboratory, Chilton, UK

^c Space Astronomy & Instrumentation Division, ISRO Satellite Centre, Bangalore, India

^d The Observatory, University of Helsinki, Finland

^e The Joint UCL/Birkbeck Research School of Earth Sciences, Gower Street, London WC1E 6BT, UK

^f Centre d'Etude Spatiale des Rayonnements, Université de Toulouse, CNRS, France

^g Brunel University, UK

^h Open University, UK

ⁱ Department of Mineralogy, Natural History Museum, Cromwell Road, London SW7 5BD, UK

^j PRL, India

^k Los Alamos National Lab, USA

^l Berkeley Geochronology Center, Berkeley, CA, USA

^m IPG Paris, France

ⁿ ISAS/JAXA, Japan

^o ESTEC, ESA, Holland

^p Brown University, USA

ARTICLE INFO

Article history:

Received 21 November 2008

Received in revised form

27 January 2009

Accepted 29 January 2009

Keywords:

Moon

Lunar composition

X-ray spectroscopy

Chandrayaan-1

Space instrumentation

ABSTRACT

The Chandrayaan-1 X-ray Spectrometer (C1XS) is a compact X-ray spectrometer for the Indian Space Research Organisation (ISRO) Chandrayaan-1 lunar mission. It exploits heritage from the D-CIXS instrument on ESA's SMART-1 mission. As a result of detailed developments to all aspects of the design, its performance as measured in the laboratory greatly surpasses that of D-CIXS. In comparison with SMART-1, Chandrayaan-1 is a science-oriented rather than a technology mission, leading to far more favourable conditions for science measurements. C1XS is designed to measure absolute and relative abundances of major rock-forming elements (principally Mg, Al, Si, Ca and Fe) in the lunar crust with spatial resolution ≤ 25 FWHM km, and to achieve relative elemental abundances of better than 10%.

© 2009 Elsevier Ltd. All rights reserved.

1. Introduction

The Chandrayaan-1 X-ray Spectrometer (C1XS) is a compact X-ray spectrometer for the Indian Space Research Organisation (ISRO) Chandrayaan-1 lunar mission, which was successfully launched on 22 October 2008. It exploits heritage from the D-CIXS instrument (Grande, 2001; Grande et al., 2003, 2007; Swinyard et al., forthcoming) on ESA's SMART-1 mission (Racca et al., 2002). However, by comparison with SMART-1, Chandrayaan-1 is a science-oriented rather than a technology

mission, leading to far more favourable conditions for science measurements. C1XS is designed to measure absolute and relative abundances of major rock-forming elements (principally Mg, Al, Si, Ca, Ti and Fe) in the lunar crust with spatial resolution ~ 25 km.

The C1XS hardware was designed and built by an international team led from the Rutherford Appleton Laboratory (RAL), STFC. The Principal Investigator is Prof. M. Grande at Aberystwyth University. There is also a major science and design contribution from ISRO Satellite Centre, Bangalore, India; CESR, Toulouse, France provides 3-D Plus video processor integrated circuits, and there is an important contribution to the detector characterisation from Brunel University. The Science team is chaired by Dr. I.A. Crawford of Birkbeck College, London. In order to record the incident solar X-ray flux at the Moon, C1XS carries an X-ray Solar

* Corresponding author.

E-mail address: M.Grande@aber.ac.uk (M. Grande).

Monitor (XSM) provided by the University of Helsinki Observatory, Finland. C1XS is primarily funded by ESA with partial support to RAL from ISRO.

D-CIXS was able to demonstrate an ability to sense remotely elements in the top few micrometers of the lunar regolith, in particular Mg, Al, Si, Ca and Fe (Grande et al., 2007; Swinyard et al., forthcoming). The Ca detections represented the first unambiguous remote sensing of calcium. More recent detailed analysis shows that in favourable conditions titanium is also observed (Swinyard et al., forthcoming). Other companion papers describe in more detail the science goals (Crawford et al., 2009), the instrument construction (Howe et al., forthcoming) and the calibration status (Kellett et al., 2009).

2. Instrument requirements

Solar irradiation excites fluorescent emission from the lunar surface; by measuring this emission, whilst at the same time monitoring the incident solar X-ray emission, we are able to map the absolute elemental abundances of the main rock-forming elements on the Moon. In addition, during bright flares, we detect localised concentration levels of key minor elements. The timing of the Chandrayaan-1 mission, ensuring that the spacecraft arrives at the beginning of the rising phase of the solar activity cycle, with

near Solar maximum flux levels expected at the end of its nominal mission, is well suited for this purpose. The 10 × higher solar X-ray fluxes, combined with the excellent (85–115 km near

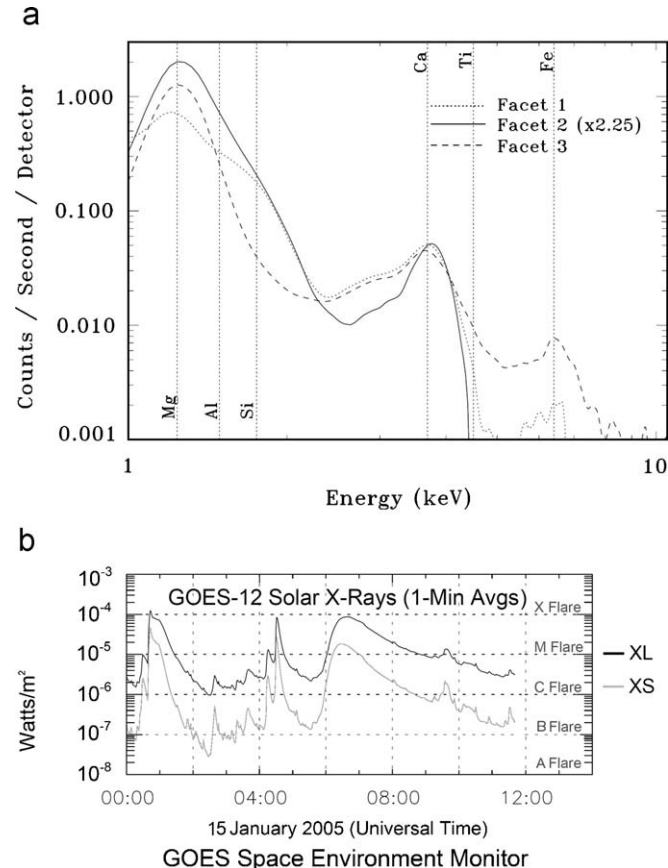


Fig. 1. (a) Fluorescence spectra obtained by D-CIXS on SMART-1 on 15 January 2005, indicating an ability to remote sense elements in the top few micrometers of the Lunar regolith, in particular Mg, Al, Si, Ca and Fe, as indicated by vertical lines (Grande et al., 2007). Vertical lines indicate the expected position of these elements. (b) Also shown is the 10 Å (black) and 1 Å (grey) (TBC) Solar X-ray illumination at the time, derived from GOES Space Environment Monitor data, indicating the high variability of the Sun as an X-ray source. Times are indicated on the x-axis in hours. Note the conventional A,B,C,M,X nomenclature for flare levels are indicated on the left-hand side of the plot.

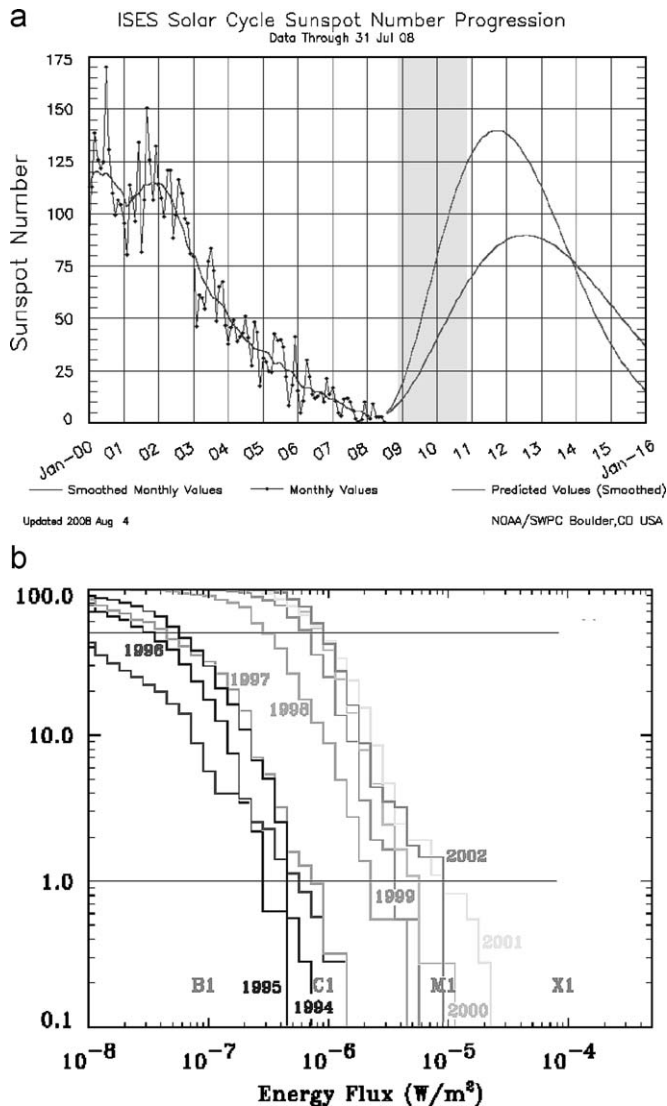


Fig. 2. (a) Past blue and predicted red solar cycle variation (NOAASpace Weather Prediction Center) during the Chandrayaan-1 missions (Ref.). Note that whilst SMART-1 took place during a decline into solar minimum, Chandrayaan-1 will be launched in the ascending phase of the cycle (shown by shaded region), which is predicted to be close to peak by the end of the mission. The two red lines indicate alternative predictions. (b) Cumulative distribution of 1 min solar flare date from the previous cycle, indicating probability of illumination above a certain illumination level more. To obtain predicted fluxes add 11 to the year.

Table 1 Energies (eV) of relevant X-ray fluorescent lines. [See discussion for those lines detectable by C1XS.]

Element	Kα ₁	Lα ₁
Oxygen	524.9	-
Sodium	1040.98	-
Magnesium	1253.60	-
Aluminium	1486.70	-
Silicon	1739.98	-
Potassium	3313.8	-
Calcium	3691.68	-
Titanium	4510.84	-
Iron	6403.84	705.0

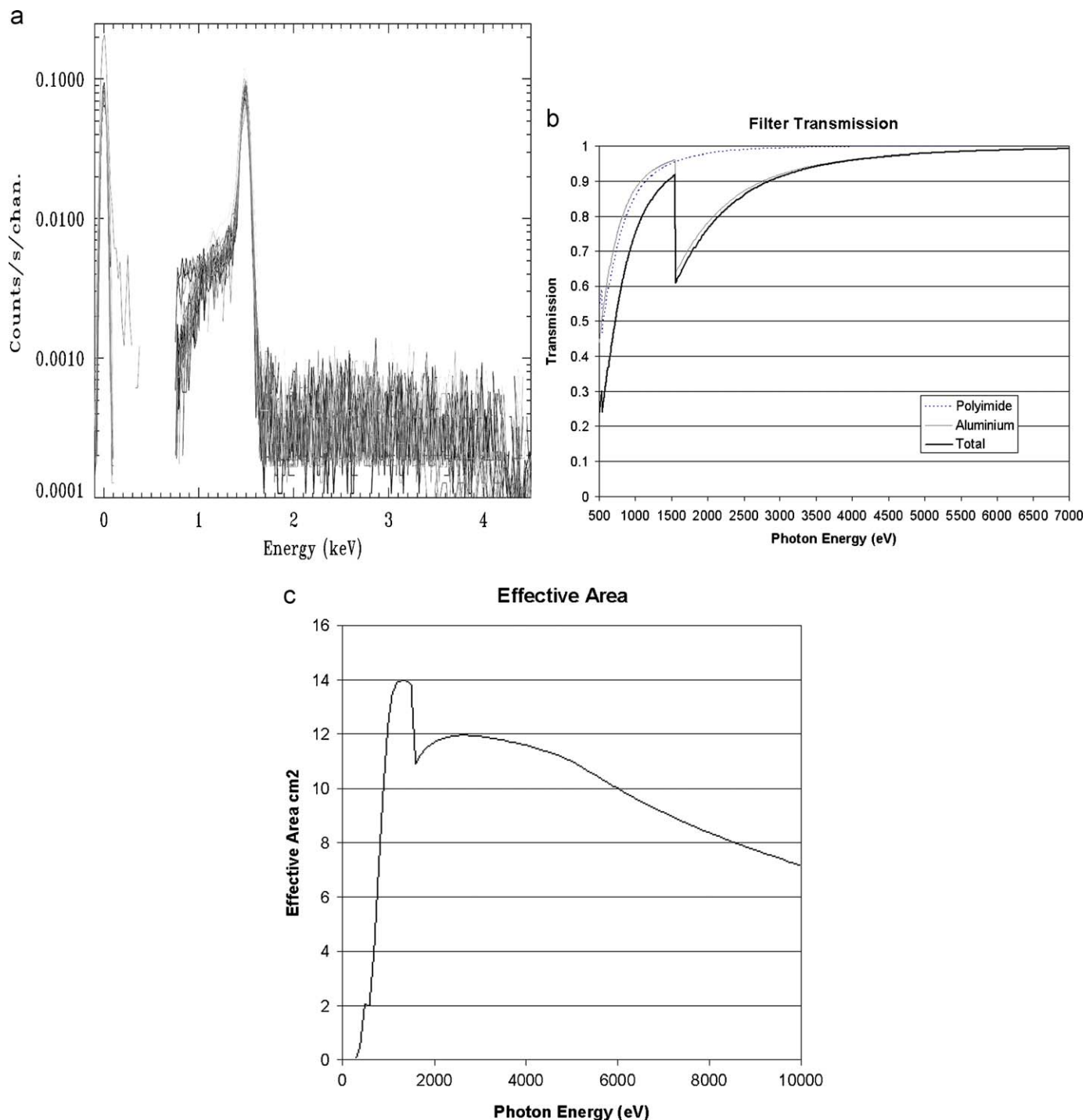


Fig. 3. (a) Measured performance at low energies in C1XS illustrating the reponse of all 24 SCDs to Al $K\alpha$ (1.487 keV), derived during calibration (Kellett et al., 2009). Note the excellent alignment and uniformity of the 24 different responses. (b) Calculated filter transmission for 800 nm of Al-coated polyimide over the active range of the instrument. (c) Calculated effective area of the instrument, plotted against energy, based on geometry, and filter and detector specification, but neglecting electronic losses. Note the rapid loss of effective area below 1 keV.

circular) orbit, will help ensure that C1XS can carry out enormously enhanced science compared to SMART-1.

The nominal mission duration is 2 years. Given the Moon's 28 day rotation, this corresponds to 25 daylight overflights for each 25 km FWHM field-of-view (FOV) on the surface, and 16 within 60° of zenith illumination. Illumination conditions will be different for each overflight, both for geometrical reasons, but much more importantly because of the huge variations in the solar X-ray illumination that takes place on timescale of minutes,

as shown in Fig. 1b. At solar maximum, expected at or shortly after the end of the Chandrayaan-1 mission, X-ray illumination is above C1 category flare conditions for $\sim 40\%$ of the time (see Fig. 2), based upon statistics from the previous cycle. In a 2-year solar maximum mission, each pixel would be sampled with near zenith C1 illumination on average 6 times. A more precise calculation shows around 95% probability of a pixel being illuminated at greater than C1 at some point during the mission, which is sufficient to return the required spectral resolution. Around 10% of

pixels should be illuminated with greater than M1 at some point during the mission. We note that C1XS is to be launched at around the beginning of solar cycle, and that fluxes are therefore very sensitive to variations of a few months in the upturn in the solar cycle relative to the launch date. Fig. 2 is based on the current (27 June 2008) best NOAA SEC predictions (Biesecker, 2008) showing the high and low predictions. Currently (Keating, 2008) the cycle appears to be an average 11-year cycle. However, flare numbers are very low compared to recent cycles. A 6-month mission extension, at full Solar maximum, would certainly yield large increase in the quality of X-ray illumination.

We can investigate minor elements like sodium, phosphorous and sulphur, which provide great insight into lunar evolution. The energy range of C1XS is 0.8–7 keV, and the energy resolution at launch is ~ 160 eV FWHM at 8 keV (2%), sufficient to resolve all the main fluorescence lines of interest, as shown in Table 1. The ability to detect sodium ($K\alpha$ at 1.043 keV) if it is present in significant quantities is particularly interesting. It may also be possible to detect the iron L-lines, which will enable C1XS to observe iron in all illumination conditions. For these reasons, particular care has

been taken in defining the lower energy cutoff, as illustrated in Fig. 3a. The low-energy discriminator level is software commandable, but whilst in theory it could be lowered to include the oxygen $K\alpha$ line at 525 keV, and the detectors have some sensitivity at these low energies, the filter cutoff shown in Fig. 3b would preclude useful information. Since the oxygen concentration across the highly oxidised lunar surface does not vary outside a range 41–46% (e.g., Lawrence et al., 1998), these data would not in any case yield significant new information. However, at the start of mission, we will have sufficient sensitivity for the Fe $L\alpha$ line at 705 eV, which greatly improves the functionality of the instrument, enabling Fe concentrations to be measured in all illumination conditions. Fig. 3c shows the calculated overall effective area of the instrument, excluding electronic considerations.

In order to obtain good absolute elemental abundances by the X-ray fluorescence technique, it is essential to continuously monitor the solar X-ray flux, which excites the lunar emission. To this end the C1XS instrument includes an X-ray Solar Monitor, designed and delivered by the University of Finland. The XSM will also provide a scientific bonus in providing a long time series of the solar X-ray spectra with high spectral resolution and full energy band coverage.

3. Instrument

The baseline instrument design (see Fig. 4) consists of 24 nadir pointing Swept Charge Device (SCD) detectors (Howe et al., forthcoming). A traditional box collimator defines the field-of-view of each SCD, resulting in a triangular angular sensitivity with 50% of the X-ray signal deriving from 14° of the collimator aperture, corresponding to 25 km on the lunar surface from Chandrayaan-1's circular 100 km orbit. Due to the highly elliptical orbit of SMART-1, the corresponding values for D-C1XS ranged from 32 to 315 km. The uniform spatial resolution of C1XS will greatly simplify the data analysis. The C1XS collimator stack differs from that on D-C1XS in that it is machined numerically, as opposed to by lithographic construction (Grande et al., 2003; Howe et al., forthcoming). Fig. 5 shows the flight instrument during calibration.

A deployable door protects the instrument during launch and cruise, and also provides a ^{55}Fe calibration X-ray source for each of

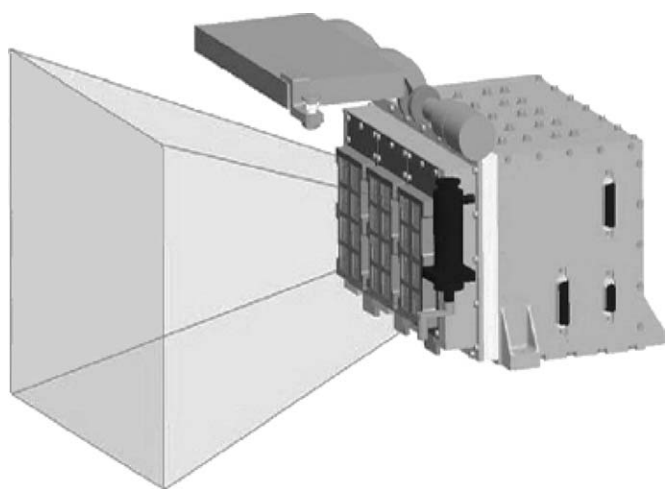


Fig. 4. CAD image of the C1XS instrument showing colligned front detectors, deployable radiation shield and 140 field-of-view. Note light-coloured thermal gasket separating cool detector enclosure from electronics case to the right. The instrument design aims to keep detector temperatures below -17.5°C , which ensures optimum signal-to-noise and stability, as well as improving radiation tolerance. The table below gives a summary of the instrument parameters for C1XS and XSM.

C1XS	
Mass	5.5 kg
Volume (with door closed)	250 mm wide, 150 mm tall, 190 mm deep
Power	6.3 W (Standby)
25.5 W (operating)	
Energy range	0.8–20 keV
Geometrical detector area	24 cm ²
Field-of-view	14° (FWHM)
28° (full angle)	
Supply voltage	20 to 45 V
Temperature range	
Electronics	–50 to +80 (off)
	–20 to +40 (operating)
Detector module	–50 to +80 (off)
–40 to +0 (operating)	
Readout frequency	87,381 kHz
Data volume (average)	36 Mbits/orbit
XSM	
Nominal energy range	1.2–20.0 keV
Energy resolution	200 eV at 5.9 keV
Number of spectral channels	512
FOV(circular) diameter	104°
On-axis geometric area	0:001 cm ²

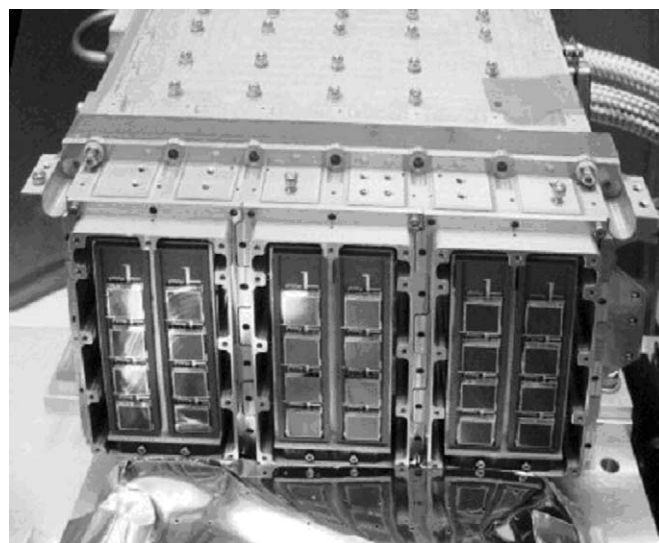


Fig. 5. View of the C1XS flight instrument during calibration. The collimator assembly and doors have not yet been added, so that the 24 swept charge detectors, arranged in ladders of four, are clearly seen.

the detectors, allowing in flight calibration to be performed. The source strength is sufficient over the 2-year mission for gain calibration to the required 1% accuracy to be obtained within 10 min. This will also allow energy and FWHM calibrations of sufficient accuracy to be obtained.

4. Detectors

The Swept Charge Device detectors (Gow et al., 2007) provide high detection efficiency in the 0.8–7 keV range, which contains the X-ray fluorescence lines of interest. The SCD is a CCD-like device which achieves near Fano-limited spectroscopy below -10°C . It has a continuous one-dimensional readout architecture, which is otherwise similar to a conventional CCD, and a 1.1 cm^2 detector area. The instrument design aims to keep detector temperatures below -17.5°C , which provides sufficiently low

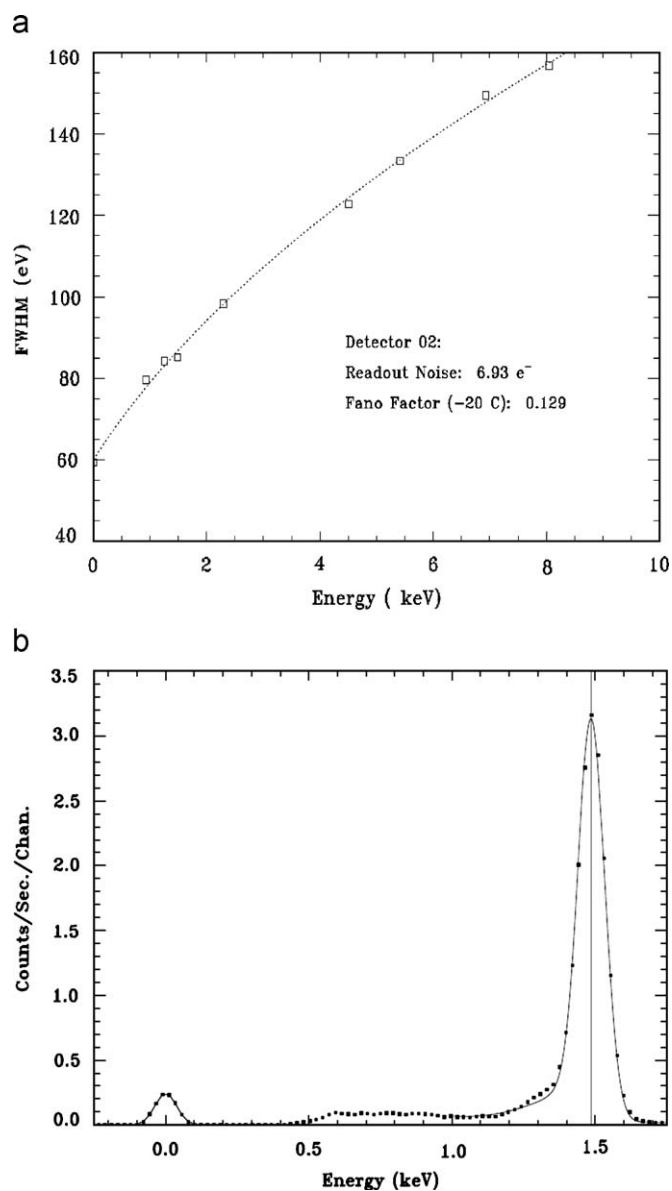


Fig. 6. laboratory performance of C1XS as obtained during calibration (Kellert et al., 2009). (a) Measured combined FWHM of the detectors and readout electronics as a function of energy. (b) Example showing measured resolution at the 1.49 keV aluminium $K\alpha_1$ line and also the well-separated zero energy electronic noise peak. Note the major improvement over the performance of D-CIXS as shown in Fig. 1.

SCD leakage current to ensure optimum signal to noise and stability, as well as improving radiation tolerance.

The detectors are shielded from the lunar UV and visible albedo, as well as protons below 180 keV and low energy electrons, by two layers of 400 nm aluminized polyimide filtering (Fig. 3b shows their calculated X-ray transmission). Careful thought has been given to the radiation shielding, in what is already a comparatively low radiation environment orbit. It will now consist of a 4-mm-thick aluminium electronics box with 3 mm of copper and 6 mm of tantalum behind the SCD modules. Due to the low altitude, the spacecraft is well-shielded from the front by the Moon itself. The collimator structure and additional tantalum provide additional shielding for oblique angles.

The principal instrument requirement is a spectral resolution sufficient to clearly resolve the three common light rock-forming elements (Mg, Al, Si). As will be seen from Table 1, this implies an energy resolution better than 250 eV at 1–2 keV. Fig. 6a and b indicates that in laboratory calibration this condition is comfortably met. The effects of radiation tests on SCD detectors from the same batch are shown in Fig. 7 suggesting that even at the end of life, the performance requirements will be met. There is some uncertainty in the predicted range of exposures due to the sensitivity to the phase of the solar cycle. The figures shown reflect the fact that as of present, large solar flares have not been observed in the current rising cycle. Note by comparison the reduced energy resolution of D-CIXS after the heavy radiation doses it incurred during its extended cruise phase to the Moon (Grande et al., 2007).

The maximum expected count rate for the C1XS instrument will be 2000 counts per second for all 24 detectors, for an X20 flare, acceptable within the instrument limit of 5500 cps (see Howe et al., forthcoming). Additional refinements to the electronics, onboard software and thermal design will also greatly increase detector stability and signal-to-noise ratio over what was achieved on D-CIXS [Grande et al., 2007]. Electronic noise has been reduced to 60 eV. A detailed account of the technical development is given in Howe et al. (forthcoming).

5. X-ray solar monitor

The X-ray solar monitor is based on the SMART-1 XSM (Huovelin et al., 2002) and consists of a separate silicon detector unit on the spacecraft. The non-imaging HPSi PIN sensor has a

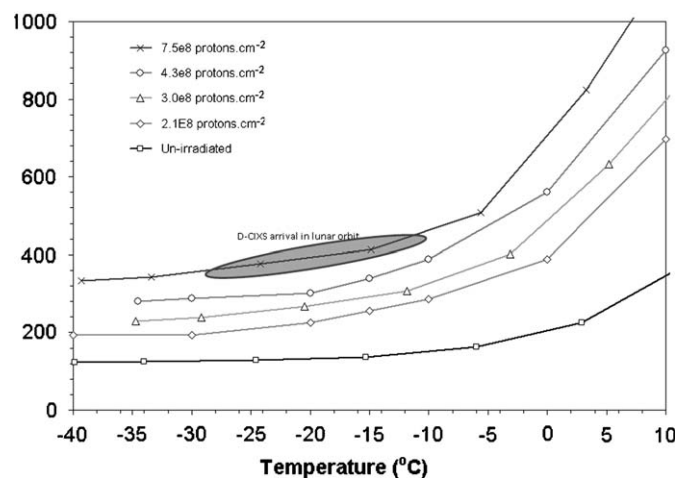


Fig. 7. Swept charge device energy resolution shown as FWHM at the Mn- $K\alpha$ line vs. temperature, before and after radiation testing. The specified maximum operating temperature is -17.5°C . Note the favourable comparison with D-CIXS FWHM shown in between the dashed lines.

wide field-of-view to enable Sun visibility during a significant fraction of the mission lifetime, which is essential for obtaining calibration spectra for the X-ray fluorescence measurements by the C1XS spectrometer. The energy range (1–20 keV), spectral resolution (about 200 eV at 6 keV) and sensitivity (about 7000 cps at a flux level of 10^{-4} W m^{-2} in the range 1–8 keV) are tuned to provide optimal knowledge about the solar X-ray flux, matching well with the activating energy range for the fluorescence measured by C1XS.

As has been remarked, the X-ray flux rises rapidly during a major solar flare. However, this is frequently followed by an increase in the penetrating background radiation, at a time-delay dependent on the energy and the geometry of the interplanetary magnetic flux. Thus, it is still in general possible to use the brightest X-class events for fluorescence spectroscopy, and the very high fluorescence count rates obtained will be invaluable in revealing the concentrations of minor elements in the regolith. Typical time delays are of up to 1 h duration.

6. Predicted response

The baseline specification is to achieve 10% relative elemental abundance accuracy from a single overflight of a 25 km pixel in C1 solar flare conditions, and we consider the instrument response in terms of this baseline situation. Fig. 8 shows the calculated response to fluorescence from a representative Lunar basalt, using our physical instrument model, indicating the minimum detectable flux for C1 flare with a 14° opening angle for a real detector area of 24 cm^2 detector and a 0.8 throughput collimator expressed

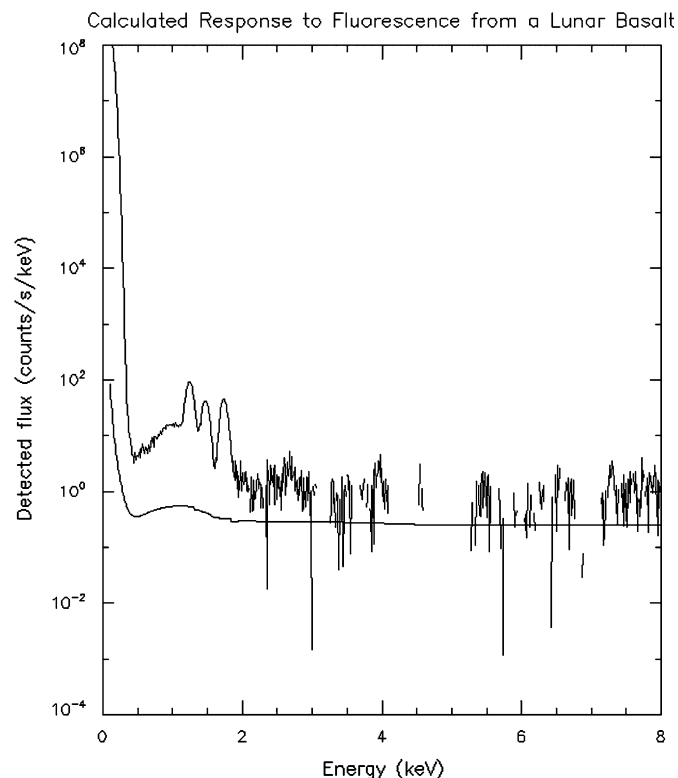


Fig. 8. Calculated response to fluorescence from a representative Lunar basalt, using our physical instrument model, indicating the minimum detectable flux for C1 flare with a 14° opening angle for a real detector area of 24 cm^2 detector and a 0.8 throughput collimator expressed as counts/s/keV and 100 eV resolution. The calculation includes calibration and electronic efficiency data from D-CIXS. The smooth line is the 3 sigma detection limit for a 16s integration, typical for overflight of a single pixel. It is seen that the Mg, Al and Si lines are well-resolved in this baseline illumination condition.

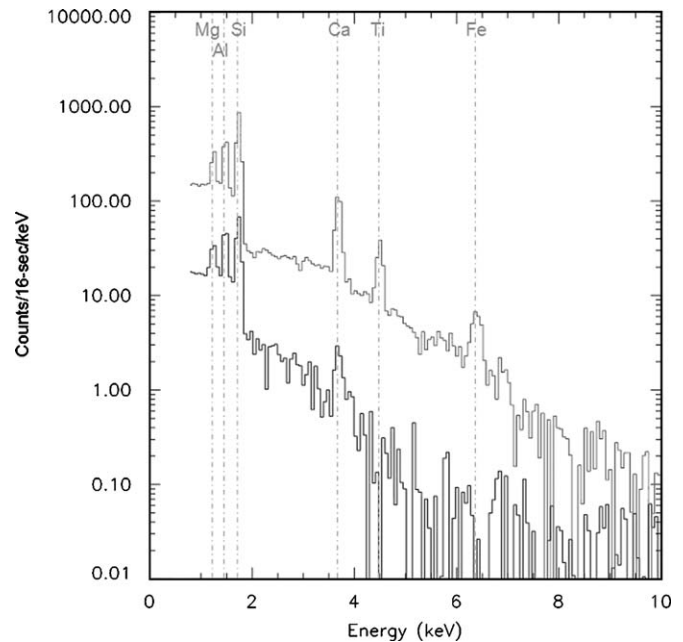


Fig. 9. Simulated C1XS spectrum for the November 18 flare based on individual 16 s integrations. The lower line (black) shows the spectrum detected during the quiet period just before flare begins, while the upper line (grey) shows the spectrum obtained at the peak of the flare.

as counts/s/keV and a 100 eV resolution. The calculation includes calibration and electronic efficiency data from D-CIXS. The smooth line is the 3 sigma detection limit for a 16 s integration, typical for overflight of a single pixel. It is seen that the Mg, Al and Si lines are well-resolved for this baseline illumination condition. As an example of inferred performance under flare conditions, Fig. 9 shows a comparison of predicted C1XS response in quiet and flare conditions to an actual event observed by D-CIXS, described in the accompanying paper by Swinyard et al. (forthcoming). Note the greatly increased signal for the low-energy Mg, Al and Si lines, and the excellent signal-to-noise ratio in the Ca, Ti and Fe lines at the peak of the flare. Again, instrument response (100 eV) is derived from C1XS laboratory calibrations (Kellett et al., 2009).

Accurate knowledge of the input solar spectrum is essential for determination of elemental abundances. A linear difference in solar input will leave the relative line ratios unchanged. However, this is not the case if the shape of the input solar spectrum changes. Fig. 10 shows 4 different flare levels (A5, B1, C1, M1), with the output spectra that would result. We note that the apparent line ratios are very significantly modified. The point is made even more clear in Fig. 11, which shows three different models of C1 solar flares (Mewe et al., 1985; Clark and Trombka, 1997). The calculated lunar fluorescent spectra, which would be detected following scintillation of lunar basalt, are also shown. In this case the predicted line ratios are modified by more than $\pm 10\%$.

This emphasizes the vital importance of accurate monitoring of the solar input spectrum, as well as good codes to forward model the expected lunar X-ray fluorescence for different possible regolith compositions. Thus, whilst elemental abundance ratios may be useful diagnostics in our initial analysis, final estimations of lunar elemental abundance ratios will require detailed modeling (see Swinyard et al., forthcoming). One of the lessons learned from D-CIXS was the critical importance of fully characterizing the input solar spectrum, if one is to derive absolute lunar elemental surface abundances. In comparison to D-CIXS, C1XS and XSM are far better calibrated. Details of the results obtained in the calibration campaign of the C1XS instrument are given by Kellett et al. (2009).

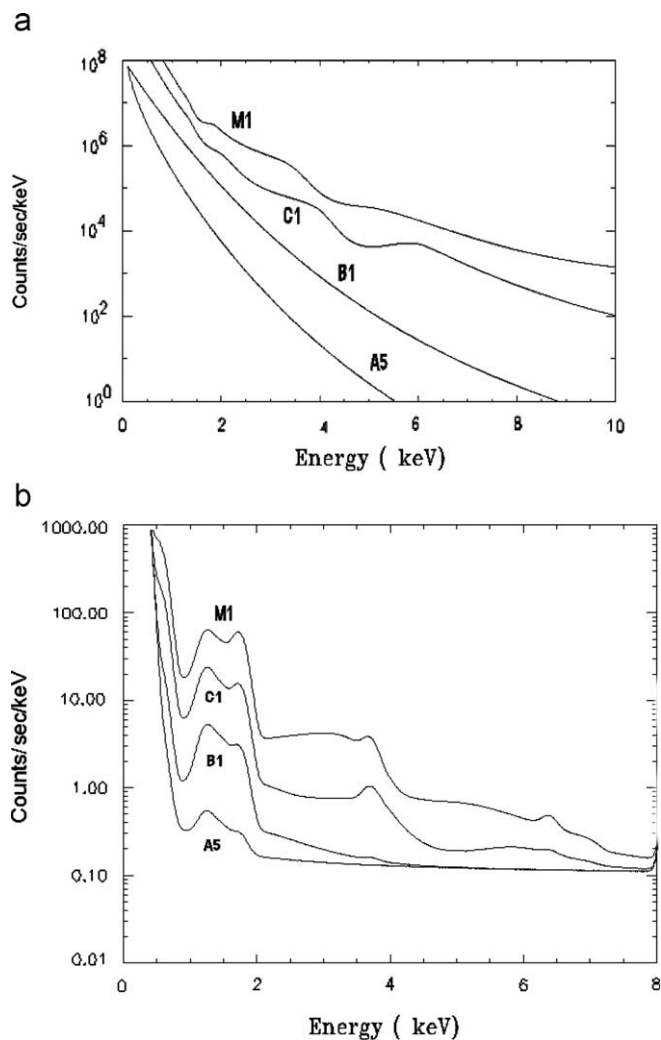


Fig. 10. Calculated lunar fluorescent spectra, which would result from four different solar flare input levels (A5, B1, C1, M1). Upper panel (a) shows input flare spectra while lower panel, (b) shows the calculated detected flux from a lunar basalt, in counts/s/keV, as detected by C1XS. Note that calcium and iron lines (at 3.7 and 6.4 keV) are only seen for the harder input spectra of the stronger flares.

7. Science goals

A detailed description of the science objectives for the instrument and the match of its capabilities to key questions is given in a companion paper by Crawford et al.

C1XS will arrive at the Moon in the run up to the maximum of the solar cycle, and the high incident X-ray flux observed from an orbit optimised for science, and coupled with good instrumental energy resolution, means that we will obtain composition data accurate to better than 10% of major elemental abundances over the entire surface. We note that observations of major element abundances for regions where samples have been obtained by the Apollo and Luna missions will be used to validate the calibration of C1XS measurements. Thus, C1XS will be well-placed to make significant contributions to lunar science in a number of areas.

Specifically, C1XS will determine the major element geochemistry (and especially Mg/Si and/or Mg/Fe elemental ratios) in the main lunar terrain types (i.e. Procellarum KREEP Terrane, South Pole-Aitken Basin, and the Farside Highlands; Jolliff et al., 2000) and establish the geographical distribution of the magnesian suite of rocks. A key ambition is to determine the large-scale stratigraphy of lower crust (and possibly crust/mantle boundary region) by measuring the elemental abundances of the floor

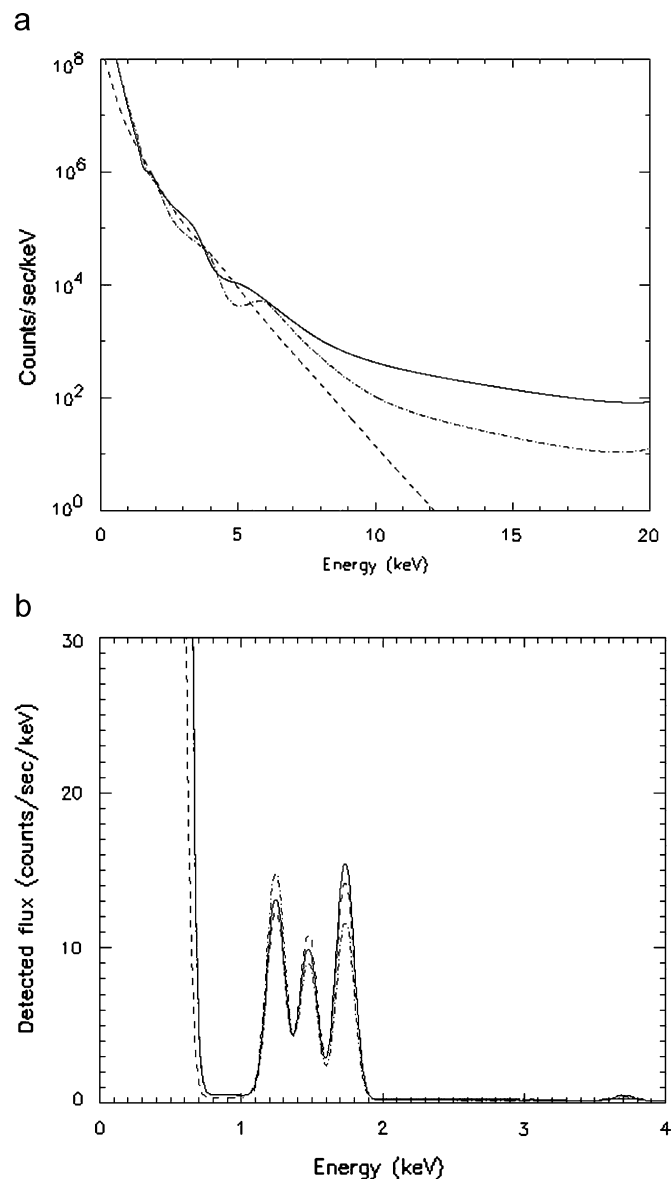


Fig. 11. (a) Three different models of C1 solar flares (dashed line, Mewe et al. (1985); dash-dotted line, Clark and Trombka (1997); full line, M1 flare from Clark and Trombka, (1997) normalised to C1 intensity). (b) Resulting calculated lunar fluorescent spectra, as detected by C1XS, that would result. Note the complete reversal of the line ratios which would be observed.

material of large basins not obscured by mare basalts (e.g., SPA and other farside basins), and the central rings and ejecta of large basins, which expose material derived from depths of many tens of km. In addition, determination of the crustal aluminium abundance and distribution is important for the assessment of lunar refractory element enrichment, and C1XS-derived aluminium abundance maps will thus constrain models of lunar origins. Last but not the least, the ~ 25 km spatial resolution will enable C1XS to address a number of smaller-scale geological issues (e.g., the composition of discrete mare basalt lava flows and, pyroclastic deposits), which also refine our understanding of lunar geological evolution (Joy et al., 2008; Crawford et al., 2009).

8. Conclusions

The C1XS instrument is optimised to perform X-ray spectroscopy in the framework provided by the ISRO Chandrayaan-1

mission to the Moon. This is highly suitable for producing high-quality data on lunar composition derived from Lunar X-ray fluorescence spectra, taken in the approach to Solar maximum. The instrument represents a considerable refinement on the original D-CIXS instrument on SMART-1. It is expected to provide data of the spatial and the spectral resolution required to produce significant progress in lunar science.

Acknowledgements

The C1XS instrument development was supported with funding from ESA Science and Technology Research Programmes. Major thanks for support are due to RAL/STFC, and also ISRO ISAC. Additional hardware was provided by CESR, Toulouse and University of Helsinki Observatory. J. Carter of Aberystwyth University is thanked for recalculating Fig. 8.

References

- Biesecker, D., the NOAA/SEC Solar Cycle 24 Panel. The Solar Cycle 24 Consensus Prediction; Web document <www.swpc.noaa.gov/SolarCycle/SC24/Biesecker.ppt>, June 2008.
- Clark, P.E., Trombka, J.I., 1997. *Journal of Geophysical Research* 102, 16631.
- Crawford, I.A., Joy, K.H., Kellett, B.J., Grande, M., Anand, M., Bhandari, N., Cook, A.C., d'Uston, L., Fernandes, V.A., Gasnault, O., Goswami, J., Howe, C.J., Huovelin, J., Koschny, D., Lawrence, D.J., Maddison, B.J., Maurice, S., Narendranath, S., Pieters, C., Okada, T., Rothery, D.A., Russell, S.S., Sreekumar, P., Swinyard, B., Wicczorek, M., Wilding, M., 2009. The scientific rationale for the C1XS X-ray spectrometer on India's Chandrayaan-1 Mission to the Moon. *Planetary and Space Science*, this volume, doi:10.1016/j.pss.2008.12.006.
- Gow, J., Smith, D.R., Holland, A.D., Maddison, B., Howe, C., Sreekumar, P., Huovelin, J., Grande, M., 2007. In: Characterisation of swept-charge devices for the Chandrayaan-1 X-ray Spectrometer (C1XS) instrument-art. no. 668601, OHW, UV, X-ray, and Gamma-ray Space Instrumentation for Astronomy XV 668616860-16860.
- Grande, M., 2001. The D-CIXS X-ray Spectrometer on ESA's SMART-1 mission to the Moon. *Earth Moon and Planets* 85–6, 143–152.
- Grande, M., et al., 2003. The D-CIXS X-ray mapping spectrometer on SMART-1. *Planetary and Space Science* 51, 427–433.
- Grande, M., et al., 2007. The D-CIXS X-ray spectrometer on the SMART-1 mission to the Moon—first results. *Planetary and Space Science* 55, 494.
- Howe, C.J., Drummond, D., Edeson, R., Maddison, B., Parker, D.J., Parker, R., Shrivastava, A., Spencer, J., Kellett, B.J., Grande, M., Sreekumar, P., Huovelin, J., Smith, D.R., Gow, J., Narendranath, S., d'Uston, L., 2009. Chandrayaan-1 X-ray spectrometer (C1XS): instrument design & technical details. *Planetary and Space Science*, this volume, doi:10.1016/j.pss.2009.01.011.
- Huovelin, J., Alha, L., Andersson, H., Andersson, T., Browning, R., Drummond, D., Foing, B., Grande, M., Hamalainen, K., Laukkanen, J., Lamsa, V., Muinonen, K., Murray, M., Nenonen, S., Salminen, A., Sipila, H., Taylor, I., Vilhu, O., Waltham, N., Lopez-Jorkama, M., 2002. The SMART-1 X-ray solar monitor (XSM): calibrations for D-CIXS and independent coronal science. *Planetary and Space Science* 50 (14–15), 1345–1353.
- Jolliff, B.L., Gillis, J.J., Haskin, L.A., Korotev, R.L., Wicczorek, M.A., 2000. Major lunar crustal terranes: surface expressions and crust-mantle origins. *Journal of Geophysical Research* 105, 4197.
- Joy, K.H., Crawford, I.A., Kellett, B., Grande, M.N., the C1XS Science Team, 2008. The Scientific Case for the Chandrayaan-1 X-ray Spectrometer. In: *Lunar and Planetary Science XXXVIX*, abstract no. 1070, 39th Lunar and Planetary Science Conference, Houston.
- Keating, C.F., 2008. Not to worry: solar magnetic activity for cycle 24 is increasing. *Eos Transactions* 89 (43).
- Kellett, B.J., et al., 2009. *Planetary and Space Science*, Manuscript, Submitted.
- Lawrence, D.J., Feldman, W.C., Barraclough, B.L., Binder, A.B., Elphic, R.C., Maurice, S., Thomsen, D.R., 1998. Global elemental maps of the Moon: the Lunar prospector gamma-ray spectrometer 4 Sept 1998. *Science* 281.
- Mewe, R., Gronenschild, E.H.B.M., van den Oord, G.H.J., 1985. *Astronomy and Astrophysics Supplement* 62, 197.
- Racca, G.D., Marini, A., Stagnaro, L., van Dooren, J., di Napoli, L., Foing, B.H., Lumb, R., Volp, J., Brinkmann, J., Grunagel, R., Estublier, D., Tremolizzo, E., McKay, M., Camino, O., Schoemaekers, J., Hechler, M., Khan, M., Rathsmann, P., Andersson, G., Anflo, K., Berge, S., Bodin, P., Edfors, A., Hussain, A., Kugelberg, J., Larsson, N., Ljung, B., Meijer, L., Mortsell, A., Nordeback, T., Persson, S., Sjöberg, F., 2002. SMART-1 mission description and development status. *Planetary and Space Science* 50 (14–15), 1323–1337.
- Swinyard, B.M., Joy, K.H., Kellett, B.J., Crawford, I.A., Grande, M., Howe, C.J., Fernandes, V.A., Gasnault, O., Lawrence, D.J., Russell, S.S., Wicczorek, M.A., Foing, B.H. The SMART-1 team. 2009. X-ray fluorescence observations of the moon by SMART-1/D-CIXS and the first detection of Ti K α from the lunar surface. *Planetary and Space Science*, this volume, doi:10.1016/j.pss.2009.01.009.



Contents lists available at ScienceDirect

Planetary and Space Science

journal homepage: www.elsevier.com/locate/pss

The Mercury Gamma and Neutron Spectrometer (MGNS) on board the Planetary Orbiter of the BepiColombo mission

I.G. Mitrofanov^{a,*}, A.S. Kozyrev^a, A. Konovalov^a, M.L. Litvak^a, A.A. Malakhov^a, M.I. Mokrousov^a, A.B. Sanin^a, V.I. Tret'ykov^a, A.V. Vostrukhin^a, Yu.I. Bobrovnikskij^b, T.M. Tomilina^b, L. Gurvits^c, A. Owens^d

^a Institute for Space Research, Profsojuznaja 84/32, 117997 Moscow, Russian Federation

^b A.A. Blagonravov Institute of Mechanical Engineering Research, M. Khariton'evskij, 4, 101990 Moscow, Russian Federation

^c Joint Institute for VLBI in Europe, PO Box 2, 7990 AA Dwingeloo, The Netherlands

^d European Space Agency, ESTEC, Keplerlaan 1, 2201 AZ Noordwijk, The Netherlands

ARTICLE INFO

Article history:

Received 27 February 2008

Received in revised form

15 January 2009

Accepted 15 January 2009

Keywords:

Gamma rays

Neutrons

Elemental composition

Radioisotopes

ABSTRACT

The main goals and objectives are presented for the Mercury Gamma and Neutron Spectrometer (MGNS) to be flown on board the Mercury Planetary Orbiter of ESAs BepiColombo mission. The instrument design is discussed and from an analysis of its properties, it is shown that the MGNS is capable of measuring the elemental composition of the shallow subsurface, providing a sensitive tool to discriminate between a number of proposed models for Mercury's origin. The instrument will also test for the presence of water ice deposits on the permanently shadowed polar craters of the planet.

© 2009 Elsevier Ltd. All rights reserved.

1. Introduction

Mercury is the third body of the solar system together with Moon and Mars, whose elementary composition might be studied by orbital observations of induced planetary gamma ray and neutron emission. The nuclear emission is produced by the bombardment of energetic cosmic rays, which freely propagate from interstellar space to the inner volume of the solar system. Particles collide with soil nuclei up to depths of 1–2 m of the subsurface and produce new nuclei and secondary high-energy neutrons in the 1–20 MeV energy range. In the leakage process, these secondary neutrons induce secondary gamma rays due to in-elastic scattering and capture reactions on soil nuclei. Natural radioactive isotopes of K, Th and U in the regolith, also produce gamma-ray lines by spontaneous radioactive decay. Therefore, nearby spacecraft may expect to detect these nuclear gamma-ray lines and from their relative strengths and energies determine elemental abundances and soil composition. One may also measure the energy spectrum of secondary neutrons from the surface to determine the hydrogen content of the subsurface, since hydrogenous material is extremely effective in moderating neutrons.

Measurements of nuclear emission from the Moon were pioneered by Vinogradov and Surkov from Luna-10 and 12 in 1966 (Vinogradov et al., 1966), and by Adler and colleagues from Apollo 15 and 16 in 1972 (Adler et al., 1969).

Much later the global mapping of lunar gamma rays and neutrons was performed by the instruments on the Lunar Prospector Orbiter (Lawrence et al., 1998; Feldman et al., 1998a, b). Maps of the nuclear lines of potassium, thorium, iron and other soil-composing elements were measured using a BGO scintillation detector which formed the central detection element of the gamma-ray spectrometer. The most intriguing result of the neutron measurements from the Moon was the detection of possible water ice in the bottom of permanently shadowed craters—both at the north and south poles. The possibility of water ice on the Moon was originally inferred from the analysis of radio data from Clementine (Nozette et al., 1996).

In 2002 NASA's Mars Odyssey started the global mapping of Martian gamma rays and neutrons. For the first time, a high-purity Ge detector was used as a remote-sensing gamma-ray spectrometer (the GRS) (Boynton et al., 2004). Maps of the regional variations of H, Si, Cl, Fe, etc. were produced, based on their nuclear line emission (Boynton et al., 2007). Gamma-ray data from the GRS also provided maps of the radioactive isotopes K and Th in the martian surface (Tailor et al., 2006a, b; Boynton et al., 2007). Neutron data from Mars Odyssey have also delivered surprising results, namely, two strong depressions in the detected

* Corresponding author. Tel.: +7495 3333489.

E-mail address: imitrofa@space.ru (I.G. Mitrofanov).

flux of epithermal neutrons from large areas of Mars: northward and southward from 60° of latitude, and also in two equatorial regions of Arabia and Memnonia (Boynton et al., 2002; Feldman et al., 2002; Mitrofanov et al., 2002, 2003a,b). The “dips” are interpreted as the signatures of subsurface water. Neutron data deconvolution (Mitrofanov et al., 2003b, 2004) indicated that both provinces above 60° are rich with water ice, whose content could be as high as 40–50 wt%. Thus water ice could be the major component of the soil in these regions. The creation of these regions in the past, and their influence on the present Martian climate are still the open questions requiring further studies of the planet.

This paper presents the concept and operation of the Mercury Gamma and Neutron Spectrometer (MGNS), which will carry out similar studies of gamma-ray and neutron emission from the planet Mercury. The experiment will be performed on board of the Mercury Planetary Orbiter (MPO), which is one of two spacecraft forming ESAs “BepiColombo” mission. The mission is scheduled for launch in 2014 (for further details see Benkhoff, 2009). The MGNS instrument is a contribution of the Federal Space Agency of Russia to this mission and its implementation is based on International agreement between the FSA and ESA.

2. Scientific goals of MGNS investigations

Because Mercury lacks a thick atmosphere, its natural nuclear emissions could be detected from orbit, i.e., gamma rays arising from cosmic-ray interactions and those arising from the natural radioactive decay of K, Th and U. Mercury has a very weak magnetic field with cut-off rigidity near the equator of ~ 1 MeV. Therefore, the galactic cosmic rays are essentially unimpeded and interact directly with the shallow subsurface producing copious secondary neutrons within the first 1–2 m of the surface (Fig. 1). These neutrons interact with the soil nuclei either by in-elastic scattering or capture reactions, producing secondary nuclear gamma rays. Each chemical element has a unique set of nuclear lines, so the data from a gamma-ray spectrometer in near-orbit can, in principle, uniquely identify the elemental composition of the Mercury shallow subsurface.

The intensity of a gamma-ray line of a particular element depends on the spectrum and flux of secondary neutrons and so knowledge of the spectral density of neutrons is also a necessary prerequisite for the determination of the elemental abundance. The energy spectrum of leakage neutrons, in turn, depends on the elemental composition of the soil. A neutron with a mass m , loses a small fraction of energy $\sim m/(M+m)$ in a collision with heavy nucleus of mass M . However, when $m = M$, the incident particle will lose half its energy, as is the case when a neutron collides with a hydrogen nucleus. Thus, it can be seen that the addition of even a little hydrogen into a soil will decrease the leakage flux of epithermal and high-energy neutrons while simultaneously increasing the flux of thermal neutrons.

That is why instrumentation for nuclear remote sensing should include both a gamma-ray spectrometer for measuring gamma-ray lines and a neutron spectrometer for measuring the flux of leakage neutrons. One has to perform a joint data deconvolution for both gamma rays and neutrons in order to evaluate the abundance of all major soil-composing elements, including hydrogen.

Mercury is arguably the most extraordinary planet in the Solar system. One reason behind some of its exceptional properties is its proximity to the Sun. It explains the largest range of surface temperatures from ~ 725 K at mid-day down to ~ 90 K at midnight, and its spin-orbit resonance with the ratio of $2/3$ between a day and a year. However, there are also some other mysterious features of Mercury, which do not result from its close proximity to the Sun. For example, Mercury has the largest uncompressed density among the planets of the solar system. It also has an anomalously high metal to silicate ratio, which may reveal the details of accretion of the early proto-planetary cloud into the planets (Siegfried and Solomon, 1974). Measurements of the elementary composition of the shallow subsurface in different regions over the planets surface may be the most important data to explain its anomalous composition. Data from the bottoms of impact craters and from the highlands may allow us to create a depth-dependent model of elemental abundances for the planet.

The second mystery of Mercury is the existence of a global magnetic field. The planet has a very slow rotation for the efficient generation of such a field. Mars with a much faster rotation has lost its field a long time ago. One may suspect that the dynamo

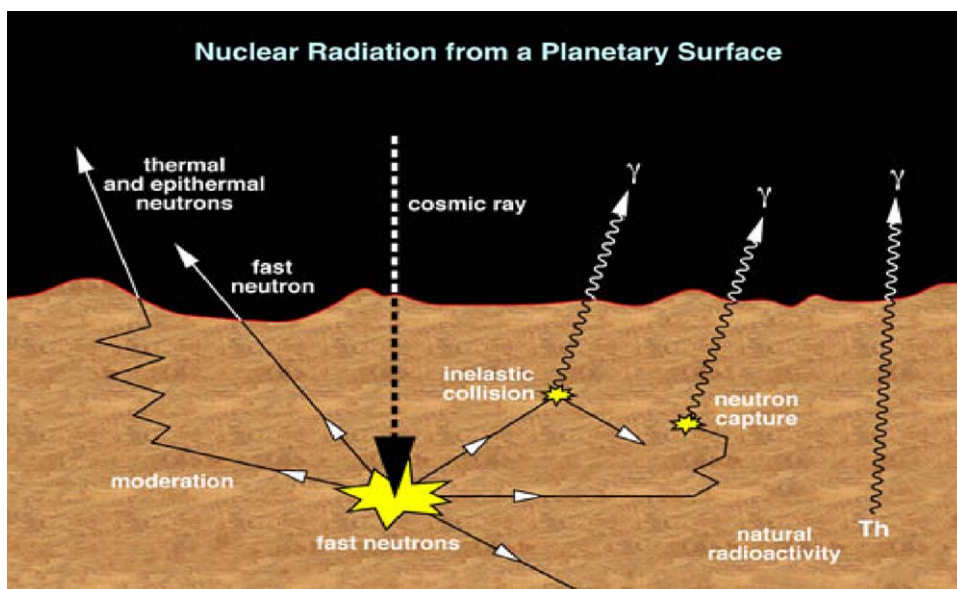


Fig. 1. Galactic cosmic rays produce secondary neutrons which induce gamma-ray line emission from the surface of Mercury. Line emission also results from natural radioactive isotopes in the surface regolith.

has resulted from a high-eccentricity orbit and/or from a possible composition anomaly at the so-called “hot meridians” of the planet (e.g. see Dolginov, 1988). The two opposite hot meridians of Mercury are known to be related to the spin–orbital resonance: at the point of orbital perihelion one hot meridian obtains the largest heating power from the Sun, and after 1 year the opposite meridian gets the same heating energy at the next perihelion passage.

Therefore, the first Goal I of the MGNS onboard the Mercury Planetary Orbiter is the following: *to determine the subsurface composition model(s) with a surface resolution of 400 km comparable with the relief features on Mercury and sufficient for testing composition anomalies at large impact basins and at the hot meridians on the planet.*

The radio data from the Goldstone/VLA radar (Morgan and Anders, 1980) have provided a possible signature of the third mystery of Mercury. The radiolocation experiment has pointed to polar deposits on Mercury, which may possibly consist of water ice. This signature of water on the Mercury poles is quite similar to that found by the Clementine radar on the poles of the Moon (Nozette et al., 1996). Deposits of water ice may have accumulated on the bottoms of shadowed craters which are never sunlit. According to popular hypothesis, the sources of water are comet impacts with Mercury, when a temporal cloud of water vapor covers the planet for a short time. A fraction of vapor is trapped in the cold crater bottoms, which accumulate a layer of water ice from each encounter with a comet. This process could be very much similar to the accumulation of water ice deposits on the Moon and the difference between the water deposition reservoirs on Mercury and on the Moon may tell us a lot about the history of

comet bombardment in the solar system. Another source of hydrogen on the Mercury surface is the solar wind. Implanted hydrogen is continuously accumulating in the subsurface soil, and regolith. However, reflection anomalies in the radio data from the Mercury poles may also be identified with sulfur deposits on the surface (Sprague et al., 1995). Therefore, the mapping of H abundance over the entire planet allows us to study the global evolution of the Mercury surface. Thus, Goal II of the MGNS is the following: *to determine of regional distribution of volatile deposits on the polar areas of Mercury, which are permanently shadowed from the Sun, and to provide a global map of hydrogen abundance.*

Therefore, the study of the elementary composition of the Mercury surface and tests of polar ice deposits are the two main Goals of the MGNS investigation. Below the two prime scientific objectives for the MGNS investigations are determined in accordance with these two Goals (Section 3). One has to be sure, that the design of the instrument and its performance is appropriate to accomplishment these Goals (see Section 6).

3. Objectives for the MGNS investigations

Nine “standard” models have been proposed to predict the elementary composition of Mercury (see Table 1). To test these models for particular geomorphological regions of Mercury, the MGNS should provide statistically significant data for a set of reference nuclear lines, which are the most distinct for these models. One should consider only four reference spectra of gamma-ray lines for comparison of these nine models: the energy spectra for models #3, #6 and #8 can be interpolated from 4 basic models #1 (Chondrite Model, ChM), #2 (Equilibrium Condensation Model, ECM), #7 (Refractory-Rich Model, RRM) and #9 (Volatile-Rich Model, VRM). Predictable elementary compositions for the 4 basic models are presented in Table 2.

One can also make use of, the known compositional data for Mars and the Moon to test between models. Indeed, Mercury is a planet of the terrestrial type and the difference of its regional compositions could be the same as the difference of individual planets. Therefore, there are another 2 testable models, the Moon (see Prettyman et al., 2006) and Mars (see Wänke et al., 2001). These models are also included in Table 2.

The accuracy of a comparison between particular composition models depends on the dynamic range of the variation in major elements (see estimated dynamic range (DR) in the last line of Table 2). It is clear that the larger the dynamic scale of elemental composition allows better discrimination between models. The most abundant elements Si and O have the smallest DR. However, the data for these elements is quite useful because they provide normalization values for other lines. There are three natural radioactive isotopes ^{40}K , ^{232}Th and ^{238}U , whose abundances may characterize the conditions at the planets creation and also allow us to select the best scenario of Mercury surface formation. Finally, we have to study the content of hydrogen on the surface of Mercury, which was either due to a billion years of solar wind and

Table 1
Known models of the Mercury composition.

Number	Model Type	Comment
# 1	Chondrite Model (see Harmon, 1997)	Basic model ChM
# 2	Equilibrium Condensation Model (see Basaltic Volcanism Study Project, 1981)	Basic model ECM
# 3	Equilibrium Condensation Model with feeding zones (see Basaltic Volcanism Study Project, 1981)	Similar to ECM, may be interpolated from ECM
#4	Dynamically Mixed Model (see Basaltic Volcanism Study Project, 1981)	It differs from other models mainly by the absence of Fe and Ti
#5	Collisionally Differentiated Model (see Basaltic Volcanism Study Project, 1981)	It differs from other models mainly by the absence of Al, Fe, Ti, Th and U
#6	Vaporization Model (see Fegley and Cameron, 1987)	It is similar to the model #7 RRM
#7	Refractory-rich Model (see Goettel, 1988)	Basic model RRM
#8	Intermediate Model (see Goettel, 1988)	May be interpolated between RRM and VRM
#9	Volatile-rich Model (see Goettel, 1988)	Basic model VRM

Table 2
Testing elementary composition for different models of surface composition.

Model	Na (%)	Mg (%)	Al (%)	Si (%)	O (%)	Ca (%)	Ti (%)	Cr (%)	Mn (%)	Fe (%)	K (ppm)	Th (ppm)	U (ppm)
ChM	0.06	20.3	3.4	22.1	45.1	3.7	0.20	2.3	0.05	2.9	6900	3.4	12
ECM	–	24.2	5.1	19.1	45.0	6.2	0.29	0.0	0.0	0.04	–	5.3	19
RRM	–	20.9	8.8	15.2	43.8	10.9	0.43	–	–	–	–	–	–
VRM	1.0	19.2	1.7	21.1	43.0	2.2	0.08	–	–	11.4	–	–	–
Moon	0.4	5.9	7.1	21.6	43.0	7.5	1.59	0.27	0.16	12.0	2700	–	–
Mars	2.4	4.1	5.5	21.2	42.0	4.7	0.54	0.14	0.03	15.2	6100	–	–
DR	~40	~6	~5	~1.5	~1.1	~5	~7	>2	>5	~40	~2.6	–	–

cosmic ray bombardment, or water ice deposition at the poles. Therefore, according to Goal I, the MGNS instrument has to satisfy the following Objective I: *to measure the nuclear lines of major soil-composing elements and natural radioactive isotopes with sufficient accuracy to test the basic composition models for distinctive geological regions over the entire surface of Mercury with a surface resolution of about 400 km.*

All hydrogen-containing deposits change the leakage flux of neutrons because of the efficient moderation of neutrons by hydrogen. According to numerical calculations (see Section 6), the flux of epithermal neutrons from the planet subsurface strongly depends on the content of water. It is shown that the addition of 0.1 wt% of water into the dry regolith leads to a 5% decrease in the flux of epithermal neutrons. The presence of water ice deposits over the dry soil also results in a similar decrease of the leakage flux of epithermal neutrons. Thus, to accomplish the goal II, the MGNS has to address the following Objective II: *to measure the spectral density of the neutrons leakage flux from thermal up to MeV energies to map the content of hydrogen over the entire planet surface with a resolution of 400 km and to test for the presence of spatially discrete water ice deposits at both poles.*

4. Physical implementation of the MGNS instrument

The instrument has been designed specifically to address objectives (I) and (II) based on the measurements and required precision outlined above. These, in turn, determine the set of detectors and initial data products of the MGNS instrument (see Table 3).

The MGNS has one detector (SCD/G) for gamma rays and four detectors (SD1, SD2, MD and (SCD/N) for neutrons. Additionally, the high-energy neutron detector (SCD/N) is surrounded by anticoincidence plastic scintillator (APS), to protect the sensitive volume of SCD/N from external charged particles. All these detectors are integrated into a single module, which also contains the electronic boards for analog signal processing, HV and LV provision, data storage, logic and interface support.

The choice of neutron detectors is based on our current understanding of the neutron leakage flux from Mercury and on the available heritage of neutron sensors; namely the High Energy Neutron Detector (HEND) onboard NASA's Mars Odyssey (see Mitrofanov et al., 2002, 2003a, b). ^3He proportional counters were used for SD1, SD2 and MD. The relevant detection reaction is $^3\text{He}+n \Rightarrow ^3\text{H}+p$. These counters are most sensitive to thermal and epithermal neutrons. The counter of SD1 has a surrounding Cd shield, which absorbs all neutrons below the threshold of 0.4 eV. This detector detects epithermal neutrons with the energies above this threshold. The counter of SD2 has no shield and detects both thermal and epithermal neutrons. The difference between counts from SD2 and SD1 corresponds to thermal neutrons. Detector MD is surrounded by a thick polyethylene enclosure inside the Cd shield. An external Cd shield rejects external thermal neutrons, and polyethylene moderates external neutrons epithermal and high-energy neutrons. Due to this moderation, detector MD is sensitive over a higher-energy range in comparison with SD1. Detector SCD/N uses a stilbene crystal for the detection of high-energy neutrons. The detection reaction is $n+H \Rightarrow n'+p$. The stilbene sensor is surrounded by a plastic scintillator, which reject external protons. Light flashes in the stilbene from recoil protons are electronically separated from light flashes from electrons produced by gamma rays. The initial data products from all four detectors SD1, SD2, MD and SCD/N allow the determination of the spectral density of neutron emission over a very broad energy range from thermal energies up to 10 MeV.

Table 3
Measurements, detectors and initial data products of MGNS.

Physical characteristics of Mercury nuclear emission	Requirements for MGNS measurements	Detectors and initial data products of MGNS instrument
Flux of gamma-ray lines from the Mercury subsurface	To measure the set of the most intense gamma-ray lines, which characterize the content of soil-composing elements and natural radioisotopes	Scintillation detector of gamma-rays SCD/G with the high spectral resolution and high efficiency for gamma-rays Data product is energy spectrum of counts for gamma-rays with 4096 linear channels at the energy range 0.3–10.0 MeV
Flux of thermal neutrons from the Mercury surface	To measure the flux of thermal neutrons below the threshold of 0.4 eV	Detectors SD1 and SD2 with ^3He proportional counters, with and without Cd shielding, respectively Data product is the time profile of counts for thermal neutrons, which is determined, as difference of counts from SD2 and SD1
Flux of epithermal neutrons from the Mercury surface	To measure the flux of epithermal neutrons in two energy ranges 0.4 eV–1 keV and 0.4 eV–500 keV	Detector SD2 with ^3He proportional counter and with Cd shielding for energy range 0.4 eV–1 keV Detector MD with ^3He counter and polyethylene moderator inside Cd shield for energy range 0.4 eV–500 keV Data products are two time profiles of counts for epithermal neutrons from SD2 and MD
Flux of high-energy neutrons from the Mercury surface	To measure the flux of high-energy neutrons in the energy range 0.3–10.0 MeV	Stilbene scintillator SCD/N within a anticoincidence plastic scintillator APC Data product is the energy spectrum of counts for high-energy neutrons with 16 energy channels for energy range 0.3–10.0 MeV

The selection of a detector for gamma-ray spectroscopy has been much more difficult. This detector has to simultaneously provide high efficiency and high resolution for the conclusive detection of all major gamma-ray lines emanating from the surface of Mercury. This is an essential prerequisite for testing models (see Table 1). It is well known that any scintillation crystal has worse results for the detection of nuclear lines compared to a high-purity germanium sensor (HP Ge) of similar mass. However, a HP Ge sensor needs an additional system for cryogenic cooling, because it only begins to work as a detector when cooled to below 130 K and preferably at temperatures below 100 K. Also, HP Ge sensors are known to degrade with increasing radiation dose, so one has to provide one more supporting system for annealing, which can heat the crystal up to about 100 °C to remove accumulated radiation damages and to recover the spectral resolution back to the perfection of the original unit. Therefore, there are two essential “overhead” costs, which one has to pay for the perfection of a HP Ge sensor: the mass and power for a cryogenic cooler and the mass and power for an annealing system.

We know that there was no way to build the MGNS instrument with a HP Ge sensor within the allocated mass and power limits of 4.3 kg and 3 W, respectively. In fact, one may expect the mass at least about 8–9 kg for the instrument. Indeed, the mass of the HP Ge gamma-ray spectrometer onboard NASA's Messenger mission is 9 kg (e.g. see Solomon et al., 2007). The largest fraction of this mass is assigned to the active cryogenic cooler. The power for the cooler is related to another limited resource from the spacecraft: to cool Ge sensor, one has to add about 15 W to the currently allocated 3 W for MGNS. Also, one should take into account the necessity of an annealing procedure for the Ge sensor after 6 years cruise flight to Mercury.

Therefore, a scintillation sensor is used for the gamma-ray spectrometer of the MGNS. To obtain the best possible efficiency

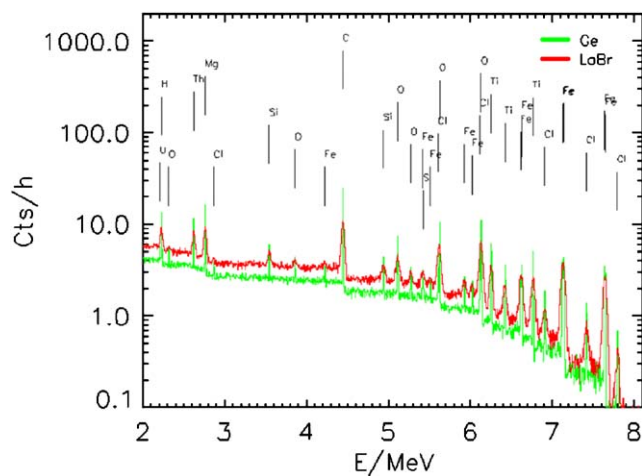


Fig. 2. Simulated energy loss spectra of gamma-ray emission from Mercury. The green shows the calculated spectra measured by a Ge detector of size $6.5 \times 6.5 \text{ cm}^2$, while the red line shows the spectra measured by a $300 \text{ cm}^3 \text{ LaBr}_3(\text{Ce})$ detector.

and spectral resolution, a new innovative scintillation material was used (LaBr_3) with a size of 3 in. When the MGNS proposal was selected in 2004, industry had not been able to produce lanthanum halide crystals of this size. However, progress was very fast, and ESA's experts accepted the arguments that crystals of the necessary size would become available in 2007, or earlier. In fact, 3 LaBr_3 crystals of the required size were produced for the MGNS in 2007.

We believe that $\text{LaBr}_3(\text{Ce})$ is the best choice among all existing scintillators because of its high-energy resolution of about 3% at 662 keV, sufficiently good photo-absorption efficiency of about 15% at 6 MeV and very good light collection. The radiation hardness of $\text{LaBr}_3(\text{Ce})$ has been the subject of space flight tests on the International Space Station (Tret'yakov et al., 2009). No evidence for radiation damage has been found in a test crystal of $\text{LaBr}_3(\text{Ce})$ after 1 year in orbit. Numerical simulation of count spectrum has been performed for gamma rays from the Mercury surface measured by a Ge sensor and a scintillation sensor based on LaBr_3 (Fig. 2). Virtually all nuclear lines, that would be detectable by the Ge sensor, would also be resolved by a LaBr_3 sensor. So, we may conclude that the MGNS with a crystal of LaBr_3 of size about 8 cm is able to measure spectral data with the necessary quality to accomplish Objective 1 of this experiment.

5. Design of the MGNS instrument

The MGNS design is based on the heritage of the High Energy Neutron Detector (HEND) flown on NASA's "Mars Odyssey" mission. The HEND has successfully operated for more than 7 years in space and has returned more than 3 Gbytes of scientific data. The concept of the MGNS design and its sensors are shown in Fig. 3(a)–(d). A schematic of the MGNS electronics is presented in Fig. 4. It consists of two detection segments: the Mercury Gamma-Ray Spectrometer (MGRS) and the Mercury Neutron Spectrometer (MNS) supported by the Digital and Logic Segment

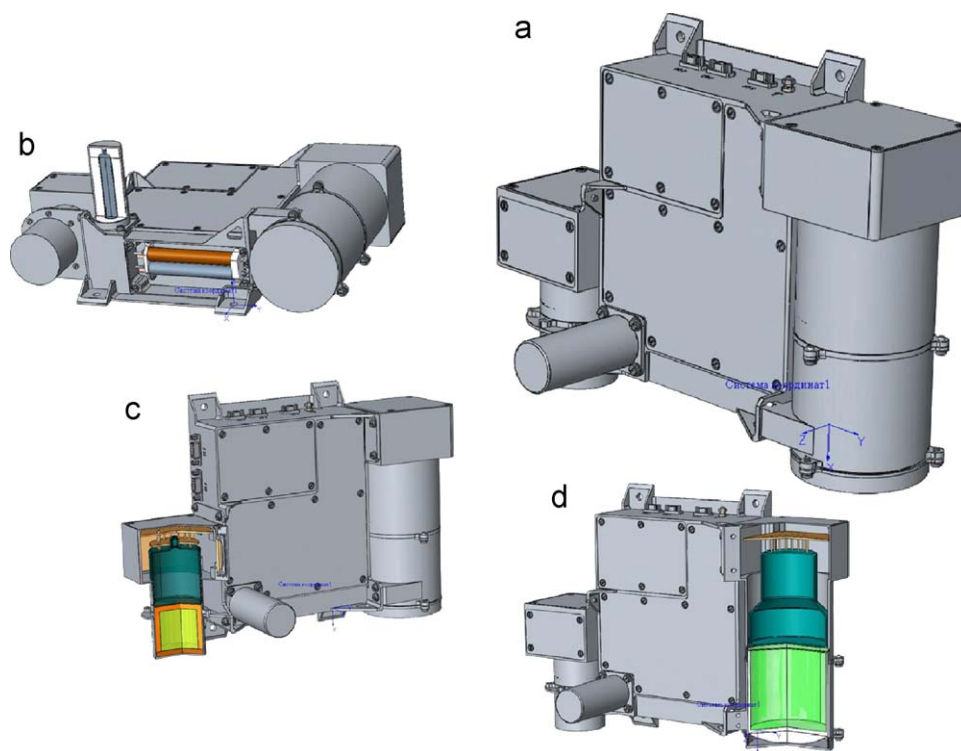


Fig. 3. Schematic views of the MGNS.

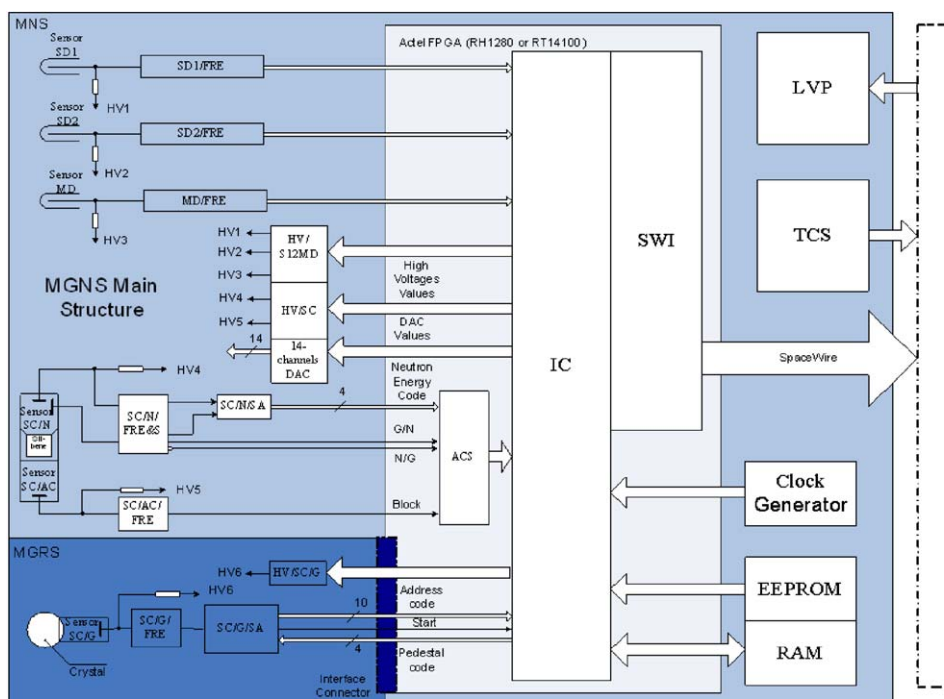


Fig. 4. The main segments and units of the MGNS.

(DLS), which is based on an FPGA. The overall dimensions of the MGNS correspond to $257 \times 342 \times 140 \text{ mm}^3$.

All three detectors SD1, SD2 and MD (Fig. 3(b)) have identical ^3He proportional counters and analog electronics. They are based on the HEND prototype elements with counter LND 2517 having a diameter of 12.7 mm, length of 94 mm and pressure of 6 atm. The digitalization of counts allows us to record the well-known two-peak energy spectrum from ^3H and p. The energy peak at 764 keV corresponds to full energy deposition of both particles, the low-energy peak at 191 keV corresponds to the energy of ^3H only, when a proton escapes from the detection volume. If necessary, one may reject the contribution of low-amplitude noise by a commendable lower-energy threshold. The front-end read-out electronics for SD1, SD2 and MD are quite simple and identical for all three sensors.

The MGNS has two scintillation sensors, SC/N and SC/G (Fig. 3(c) and (d)). The sensor SC/N has a stilbene scintillator. It is also based on the HEND heritage. Recoil protons have randomly distributed energies from 0 up to the total energy of the neutron, E_n , and produce a scintillation flash in the stilbene. The light is easily detected for energetic protons above energy of $\sim 300 \text{ keV}$. The low-energy cut-off of the sensor SC/N is determined by this threshold. The high-energy cut-off is governed by the decreasing cross section of the recoil reaction with increasing neutron energy. We use a cylindrical stilbene crystal of size $\varnothing 30 \times 40 \text{ cm}$ for detector SC/N. The efficiency curve for neutron detection by the SC/N has a maximum of about a few cm^2 around 2.0 MeV.

Electrons, either external, or produced by gamma rays, also generate scintillation light in the stilbene crystal, as well as protons. However, the time profiles of the scintillation flash are quite different for electrons and protons, and a special analog board of the MNS segment separates counts into these two categories. It has a high accuracy for separating electrons and protons with a misidentification of only 1 case in 2000. External cosmic ray protons have also to be separated from recoil protons. Similarly to the design of HEND, a plastic scintillator surrounds the stilbene crystal for the rejection of external protons. An event

in the plastic is used for the generation of a veto signal for rejecting cosmic ray events in the stilbene.

The gamma-ray spectrometer of the MGRS (Fig. 3(d)) is based on LaBr_3 scintillation crystal with a size of about 8 cm (both in diameter and length). For a spectral resolution of 3% at 662 keV, one would like to have about 8 energy channels over the Gaussian profile of the spectral line. Therefore, events from this sensor are converted into an energy spectrum with 4096 linear channels over the energy range 300 keV–10.0 MeV.

The architecture of the digital and logic segment (DLS) is based on a radiation-resistant Actel FPGA (Fig. 4). The logic of the FPGA is developed in accordance with project requirements and specifications. Low- and high-voltage supply units are operated by the DLS with the possibility of changing the levels of HV by commands. The DLS unit also provides the interface with spacecraft systems for power, thermal control, data readout and commanding.

6. The MGNS instrument capability

A Monte Carlo simulation of gamma-ray emission from Mercury has been performed according to six basic models of surface composition: ChM, ECM, RRM, VRM, the Moon and Mars (Table 1). The flux of the gamma-ray continuum from Mercury has to be combined with the local background from the MPO spacecraft. One cannot know the actual gamma-ray background for the real case of MGNS onboard MPO, until the first data is obtained during the orbital flight around Mercury. However, data from NASA's Mars Odyssey helps to perform qualitative estimations of the continuum, because data from the GRS both before and after deployment are available to the MGNS team. Numerical simulation of the MGNS sensitivity for gamma-ray lines have been performed for a $\text{LaBr}_3(\text{Ce})$ gamma-ray sensor of volume 300 cm^3 . The possibility of detecting intrinsic activation lines in the crystal has not been taken into account in this analysis, because it depends on the content of radioactive nuclei in the particular

crystal (e.g. see Kernan, 2006). During the development stage of the MGNS instrument a special program of physical measurements will be performed to select the best crystal from a set of available units with minimal radioactive contaminants for the flight instrument, and also to characterize the main intrinsic lines of the instrumental background. The instrument gamma-ray background will also contain lines from materials of the spacecraft itself—so another program of in-flight measurements and numerical simulations will be carried out during the cruise and orbital stage of the mission to determine the energy and intensity of these background lines for their proper exclusion.

Also these simulations did not take into account potential overlapping of several nuclear lines due to close energy values. For example, two lines of Si and U have very close energies of 1779 and 1764 keV, respectively. The overlap will affect the MGNS sensitivity for these lines because of added uncertainties in the evaluated counts for each line. The problem, which is a well-known problem in gamma-ray spectroscopy, will be taken into account at the stage of MGNS data deconvolution, when several different lines for the same element may be analysed together for the most reliable estimation of its content at the surface.

Table 4 represents the estimated detection time t_{det} for nuclear lines from the major elements on Mercury surface (3σ detection limit) in correspondence with the six basic models of subsurface composition (Table 1). The detection time, t_{det} , of an individual nuclear line radiated by a particular surface element (pixel) should be compared with the total exposure time, t_{exp} , for this pixel. The time, t_{exp} , could be evaluated, as the sum of all time intervals, when the MPO flies above the pixel along the predicted elliptical orbit. The mapping stage of MPO is assumed to be 1 Earth year. We assume a pixel size of about 400 km on the surface, which corresponds to the MPO altitude at the pericenter part of the orbit. The exposure time of a pixel depends on its latitude. The shortest exposure time corresponds to pixels near the equator (10 h for a 400 km pixel), and the largest exposure corresponds to poles (193 h for a 400 km pixel).

If the detection time t_{det} for testing nuclear line emission for a particular pixel is smaller than t_{exp} for this pixel, it can be measured with a significance of $>3\sigma$ during the whole period of the mapping stage. On the other hand, if the exposure time of a particular pixel is smaller than the estimated detection time for a line, it can not be measured with a high significance $>3\sigma$. One may introduce three ranges of intensity for gamma-ray lines from the surface of Mercury, which corresponding to different levels of detection accuracy by the MGNS. The total time of one Earth year of the orbital mapping phase corresponds to a maximal exposure time $t_{\text{exp}}^{(\text{max})} = 8760$ h for the entire surface of the planet. The weakest lines with a detection time longer than $t_{\text{exp}}^{(\text{max})}$ would not be detectable by the MGNS during the one Earth year of the orbital flight.

The exposure time of a polar surface element with a size of 400 km corresponds to $t_{\text{exp}}^{(\text{pole})} = 193$ h. One may introduce a *Weak Intensity Range (WIR)* for lines, for which the detection time corresponds to the condition $t_{\text{exp}}^{(\text{max})} > t_{\text{det}} > t_{\text{exp}}^{(\text{pole})}$. The lines with the minimal intensity of the WIR could be measured for the entire planet with a significance of about 3σ . On the other hand, lines of the WIR with a maximal intensity could be mapped with 400 km resolution around poles and with worse resolution at moderate latitudes.

The exposure time of a 400 km pixel at the equator is $t_{\text{exp}}^{(\text{equ})} = 10$ h. The lines from the *Moderate Intensity Range (MIR)* have a detection time, which corresponds to the condition $t_{\text{exp}}^{(\text{pole})} > t_{\text{det}} > t_{\text{exp}}^{(\text{equ})}$. The weakest lines in the MIR could be measured with 3σ significance from a surface element of 400 km at the pole, and brightest lines could be measured at the same surface elements at the equator. Finally, lines of the *Bright Intensity Range (BIR)* have a short enough detection time for the condition $t_{\text{det}} < t_{\text{exp}}^{(\text{equ})}$. These lines could be measured over the entire surface with resolution of 400 km and a high significance $>3\sigma$.

The data of Table 4 characterize the scientific performance of the MGNS for the measurement of the main nuclear lines. The

Table 4

Estimated detection times t_{det} (3σ significance level, in hours) for major nuclear lines of three ranges if intensity WIR, MIR and BIR in correspondence to the basic testing models of Mercury composition.

Model	Intensity range	Na 0.44 MeV	Fe 0.847 MeV	Ti 0.984 MeV	Al 1.01 MeV	Mg 1.34 MeV	Si 1.78 MeV	Ca 3.74 MeV	O 6.13 MeV	K 1.46 MeV	U 1.76 MeV	Th 2.61 MeV
ChM	WIR							891				
	MIR	16		54						12	116	19
	BIR		1.5		1.5	0.01	0.01		0.3			
ECM	WIR							546				
	MIR			187							48	
	BIR				1.4	0.01	0.02		0.3			7.7
RRM	WIR							464				
	MIR			175								
	BIR				0.6	0.01	0.03		0.3			
VRM	MIR	15		40								
	BIR		0.08		2.8	0.01	0.01		0.3			
Moon	WIR							513				
	MIR	22		65								
	BIR				0.6	0.06	0.01		0.3	0.01		0.01
Mars	WIR							2292				
	MIR			54								
	BIR	5	0.04		0.7	0.09	0.01		0.3	0.01		0.6

detection times are estimated for the different basic models of Mercury subsurface (see Table 1). Due to the different detection times, three different ranges of line intensity correspond to the different mapping capabilities of the MGNS. Summarizing: there is little capability for mapping the emission of lines in the WIR category, except close to the poles. If lines belong to the MIR category, one can create emission maps with a surface resolution of 400 km at the poles and some worse resolution at moderate latitudes. If lines are sufficiently bright and belong to the BIR category, the maps will be created with 400 km resolution over the entire planet.

It is evident from Table 4 that the MGNS measurements of the Fe, Ti, Al and Si lines allow a conclusive comparison between all four test models of Mercury's composition and to distinguish them from Lunar and Martian models. For example, the Al line at 1.01 MeV allows us to distinguish between three groups of models: RRM, VRM and (ChM+ECM). The Fe line at 0.847 MeV is important to selection between the ChM and VRM models. Comparison between the ChM and ECM models could be based on the Si line at 1.78 MeV. The MGNS sensitivity would allow us to resolve surface variations of all these lines with a resolution of about the altitude of the orbit, which varies from 400 km up to 1500 km. This should be sufficient for testing particular composition models for large-scale morphological structures on the planet and for testing the composition anomalies along the hot meridians. Measurements of weak Na, Ti and Ca lines may characterize the average composition over the entire surface, but the dynamic ranges of these lines are sufficiently large for different test models, that they could also be useful when comparing the geochemical properties of Mercury, Mars and the Moon.

According to the available data for Mars and the Moon, the lines of the natural isotopes K and Th could be sufficiently strong for mapping with the best possible resolution of about 400 km. Large provinces were found on the Moon with a high content of K and Th, which are interpreted as signatures of the basalt with a high content of KREEP elements (K is potassium, REE is rare earth elements and P is phosphorus). The existence of such provinces is thought to be the result of a huge catastrophic outflow of magma on the young Moon. The same provinces on Mercury could be tested by the MGNS using radioactive isotope data. The most interesting regions for these tests are giant impact craters and longitude strips along the hot meridians.

So, one may conclude that the MGNS has enough capabilities to provide data on the emission of nuclear lines from Mercury, which would be statistically sufficient to accomplish *Objective 1* of this investigation—to determine the best composition models, either for the main geological provinces, or for the entire planet.

To characterize the capability of the MGNS to test for the presence of implanted hydrogen, or water ice deposits and to map the content of hydrogen over the planet, a numerical simulation of the neutron flux from Mercury has been performed using the

MCNPX code, assuming the abundance of soil-composing elements according to the Moon model (Table 1). Fig. 5 represents the calculated decrease of the leakage flux of epithermal neutrons for increasing content of hydrogen in the soil (as water equivalent weight %). One can characterize the accuracy of the MGNS measurements of neutrons by the detectable relative variation $\delta F/F$ of epithermal neutron flux (3σ significance) from a surface pixel of 400 km size.

According to numerical simulations of the neutron leakage flux from Mercury, the average flux from the dry surface corresponds to $3.4 \text{ counts s}^{-1}$ of epithermal neutrons and $6.0 \text{ counts s}^{-1}$ of high-energy neutrons. We know from the experience of Mars Odyssey that the local background rate of neutrons from the spacecraft is comparable with the rate of the counts from the planet. Taking into account the estimated exposure time of a pixel of 400 km at the equator, one may conclude that the MGNS has enough capability to map the content of water with accuracy better than 0.1 wt% over the entire surface of the planet with a resolution of about 400 km. The surface deposition of water ice may also be measured by the MGNS with an accuracy of about 0.1 g cm^{-2} of ice top layer and a surface resolution of about 400 km. The numerical simulation proves that the MGNS satisfies the requirements of Objective II of the project.

7. Conclusions

NASA has already launched the Messenger mission to Mercury, which will deliver a high-purity germanium gamma-ray spectrometer and neutron detector into orbit around the planet (Solomon et al., 2007). In 2008 the first data on Mercury nuclear line emission is returned to Earth, but the mapping coverage of Mercury will not be complete. Messenger will have highly elliptical, 12 h orbit around Mercury with its pericenter at north polar region. The mission will not be able to provide global coverage of nuclear emission from Mercury, and it will not measure the nuclear data from the south pole region at all.

The MGNS instrument is shown to have necessary capabilities to characterize the elementary composition of the subsurface layer of the entire planet and to test for the presence of water ice deposits at both polar regions of the planet. Data from the MGNS are complementary with data from other instruments onboard Mercury Planetary Orbiter, which constitute a group of instruments for studies of the geochemistry of the subsurface (see Benkhoff, 2009). These are SIMBIO-SYS and MERTIS for mineralogy and MIXS for elemental abundance. The data from BELA (the Mercury laser altimetry) will also be very useful to determine the contours of permanently shadowed polar regions, which are possible cold traps for water vapor deposition. Therefore, the synergy of the suite of MPO science instrumentation will enhance the capability of each particular investigation, so one can be confident that the data from the MGNS will provide an essential contribution to the science output of BepiColombo mission. The MGNS instrument is a Russian-made, Russian-paid contribution of Federal Space Agency to ESA's BepiColombo mission to Mercury.

The MGNS instrument will have a space protoflight. A very similar neutron and gamma-ray spectrometer (HEND NS) will be installed onboard the Russian spacecraft "Phobos-Grunt" for a Phobos landing and soil return. The HEND NS instrument will have essentially the same set of neutron sensors as the MGNS. The only difference is that its gamma-ray spectrometer will be a down-scaled version of the MGNS one. A LaBr_3 crystal of 2 in will be used for HEND NS in comparison with a 3 in crystal used for the MGNS. The main measurements of the HEND NS will be performed on the surface of Phobos, when the exposure time at

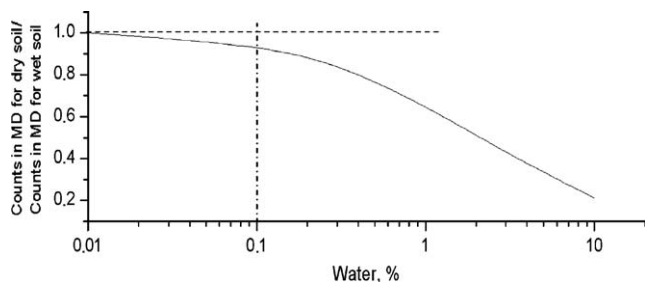


Fig. 5. The measured fractional variation of counts due to epithermal neutrons ($\delta F/F$) as a function of water content in the subsurface.

the landing site could be as long as the time of surface operations. Therefore, the smaller sensitivity of the HEND NS gamma-ray detector for the HEND NS will be offset by the much longer exposure time for measurements of the gamma-ray spectrum.

Experiments with the HEND NS will allow the main design elements of the MGNS to be tested in the conditions of space flight. The scheduled “Phobos-Grunt” launch date of October 2009 still allows us to take into account any design issues or peculiarities of the HEND NS operations, which could be faced during the first period of space flight of the HEND NS. The data from these two similar experiments would be very useful for a direct comparison of the elemental composition of Mercury and Phobos. Differences and/or similarities in elemental abundances of these two bodies, together with the available data for the Moon and Mars, will allow us to make an important step in the understanding of the origin and evolution of celestial bodies in the internal part of the Solar System.

Acknowledgments

The authors are thankful to Drs. Benkhoff, Bodo Gramkow, Marc Schwetterle together with all other professional people of the team of the Mercury Planetary Orbiter of ESA BepiColombo mission, who closely cooperated with us throughout the process of instrument design and development. We also wish to acknowledge the anonymous referees of this paper for very valuable comments and suggestions. The part of this work was supported by the Russian Foundation for Basic Research (Grant 08-08-90473).

References

- Adler, I., et al., 1969. *Earth, Moon and Planets* 7, 487.
- Basaltic Volcanism Study Project: Basaltic Volcanism on the Terrestrial Planets, 1981. *Geophysical and Cosmochemical Constraints on Properties of Mantles of the Terrestrial Planets*. Pergamon Press, Oxford, pp. 634–699 (Chapter 4).
- Benkhoff, J., 2009. *Planetary and Space Science*, this issue.
- Boynton, W., et al., 2002. *Science* 297 (5578), 81–85.
- Boynton, W., et al., 2004. *Space Science Reviews* 110 (1), 37–83.
- Boynton, W., et al., 2007. *Journal of Geophysical Research* 112 (E12).
- Dolginov, A.Z., 1988. *Physics Reports* 162 (6), 337–416.
- Fegley, B., Cameron, A., 1987. *Earth and planet. Science Letters* 82 (3–4), 207–222.
- Feldman, W., et al., 1998a. *Science* 281, 1489.
- Feldman, W., et al., 1998b. *Science* 281, 1496.
- Feldman, W., et al., 2002. *Science* 297 (5578), 75–78.
- Goettel, K., 1988. In: Vilas, F., Chapman, C.R., Mathews, M.S. (Eds.), *Mercury*. University of Arizona Press, Tucson, pp. 613–621.
- Harmon, J., 1997. *Advances in Space Research* 19, 1487.
- Kernan, W.J., 2006. *IEEE Transactions on Nuclear Science* 53 (1).
- Lawrence, D., et al., 1998. *Science* 281, 1484.
- Mitrofanov, I., et al., 2002. *Science* 297 (5578), 78–81.
- Mitrofanov, I., et al., 2003a. *Science* 300, 2081–2084.
- Mitrofanov, I., et al., 2003b. *Solar System Research* 37 (5), 366–377.
- Mitrofanov, I., et al., 2004. In: 35th Lunar and Planetary Science Conference, March 15–19, League City, Texas, abstract no.1640.
- Morgan, J., Anders, E., 1980. *Chemical composition of Earth, Venus, and Mercury*. Proceedings of the National Academy of Sciences United States of America E—Physical Sciences 77, 6973–6977.
- Nozette, S., et al., 1996. *Science* 274, 1495.
- Prettyman, T., et al., 2006. *Journal of Geophysical Research* 111 (E12).
- Siegfried, R., Solomon, S., 1974. *Icarus* 23, 192.
- Solomon, S., et al., 2007. *Space Science Reviews* 131 (1–4), 3–39.
- Sprague, A., et al., 1995. *Icarus* 118, 211–215.
- Taylor, J., et al., 2006. *Journal of Geophysical Research* 111 (E3).
- Tret'yakov, V., et al., 2009. *Kosmicheskie Issledovaniya* (in Russian), in press.
- Vinogradov, A., et al., 1966. *Space Research* 4, 871.
- Wänke, H., et al., 2001. *Space Science Review* 96, 317–330.



Contents lists available at ScienceDirect

Planetary and Space Science

journal homepage: www.elsevier.com/locate/pss

X-ray fluorescence observations of the moon by SMART-1/D-CIXS and the first detection of Ti K α from the lunar surface

B.M. Swinyard^{a,*}, K.H. Joy^{a,b,c}, B.J. Kellett^a, I.A. Crawford^b, M. Grande^d, C.J. Howe^a, V.A. Fernandes^{e,f}, O. Gasnault^g, D.J. Lawrence^h, S.S. Russell^c, M.A. Wieczorekⁱ, B.H. Foing^j, The SMART-1 team

^a Space Science and Technology Department, Rutherford Appleton Laboratory, Didcot, Oxon, OX11 0QX, UK

^b UCL/Birkbeck Research School of Earth Sciences, UCL, Gower Street, London, WC1E 6BT, UK

^c IARC, The Department of Mineralogy, The Natural History Museum, Cromwell Road, London SW7 5BD, UK

^d Institute of Mathematical and Physical Sciences, University of Wales, Aberystwyth, Ceredigion, SY23 3BZ, UK

^e Isotope Geochemistry and Cosmochemistry Group, SEAES, University of Manchester, Oxford Road Manchester, M13 9PL, UK

^f Berkeley Geochronology Center, Berkeley, USA

^g Centre d'Etude Spatiale des Rayonnements, CNRS/UPS, Toulouse, France

^h Johns Hopkins University, Applied Physics Laboratory, Laurel, MD, USA

ⁱ Institut de Physique du Globe de Paris, France

^j ESA Research and Scientific Support Department, ESTEC/SCI-S, Postbus 299, NL-2200 AG Noordwijk, The Netherlands

ARTICLE INFO

Article history:

Received 4 September 2008

Received in revised form

10 December 2008

Accepted 25 January 2009

Keywords:

XRF spectroscopy

Moon

Space missions

Lunar science

ABSTRACT

The demonstration of a compact imaging X-ray spectrometer (D-CIXS), which flew on ESA's SMART-1 mission to the Moon (Racca et al., 2001; Foing et al., 2006), was designed to test innovative new technologies for orbital X-ray fluorescence spectroscopy. D-CIXS conducted observations of the lunar surface from January 2005 until SMART-1 impacted the Moon in September 2006. Here, we present scientific observations made during two solar flare events and show the first detection of Titanium K α from the lunar surface. We discuss the geological implications of these results. We also discuss how experience from D-CIXS has aided the design of a similar instrument (Chandrayaan-1 X-ray Spectrometer (C1XS)) that was launched on the 22nd October 2008 on India's Chandrayaan-1 mission to the Moon.

© 2009 Elsevier Ltd. All rights reserved.

1. Introduction

Global geochemical information is a requirement for understanding the complex compositional makeup of differentiated planetary bodies like the Moon. Theories of lunar evolution derived from petrological investigations of the Apollo and Luna samples have been greatly refined by the global elemental and mineralogical datasets provided by the Apollo X-ray fluorescence (XRF) and Gamma-ray experiments (Adler et al., 1973; Adler and Trombka, 1977; Andre et al., 1977), the Clementine (Lucey et al., 1998, 2000; Lucey, 2004; Pieters et al., 2006) and Lunar Prospector (Lawrence et al., 2002, 2003; Prettyman et al., 2006) missions, combined with studies of lunar meteorites. The Moon can no longer be thought of as simply being comprised of feldspathic highland (primary crust) and mare basalt (secondary crust) lithologies. Instead several different geochemically defined terranes have been identified (Clark and Hawke, 1981, 1991; Jolliff

et al., 2000), necessitating a re-examination of lunar geological history (Wieczorek et al., 2006; Shearer et al., 2006). However, the global perspective is by no means complete yet, and new lunar orbital mapping missions are providing better spatially resolved data sets and the distribution of previously unmapped elements, helping to complete the global view of lunar crustal compositional heterogeneity.

X-ray spectroscopy is a powerful method for studying the major element concentration of geological materials. In a laboratory environment, a stabilised, and well characterised, X-ray or electron beam is used to provide the necessary energy for excitation of X-ray emission. In the case of an X-ray stimulus, the technique is referred to as X-ray fluorescence (XRF) spectroscopy. In planetary XRF studies, solar X-rays are the prerequisite exciting source (Yin et al., 1993), and typical levels of solar intensity will result in the excitation of low atomic number elements, including Mg, Al and Si. In periods of more intense activity (i.e. solar flares), excitation of heavier elements like P, K, Ca, Ti, Mn, Fe and Co can also occur (Yin et al., 1993). The technique can therefore be employed to study a range of different planetary inner solar system bodies like the Moon, Mercury and

* Corresponding author. Tel.: +44 0 1235 446271; fax: +44 0 1235 446667.
E-mail address: B.M.Swinyard@rl.ac.uk (B.M. Swinyard).

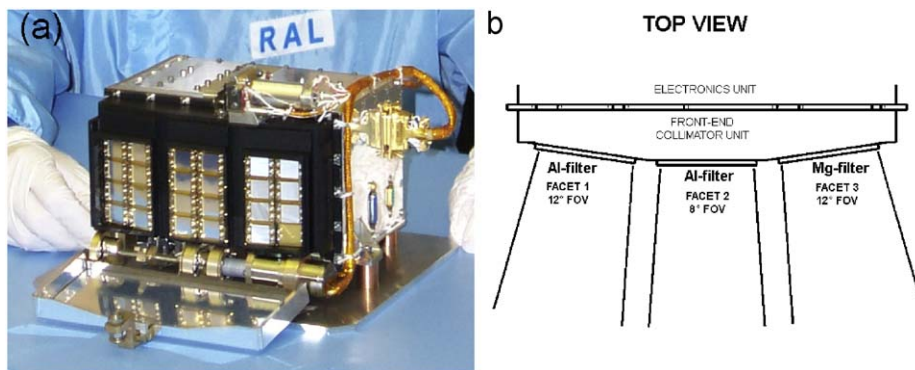


Fig. 1. (a) Photograph of the D-CIXS flight model (Image: RAL). (b) Schematic diagram of the D-CIXS front end assembly where—the view is shown looking down from the top of the instrument. The three Facet orientations are illustrated with their different opening angles and filter types.

asteroids (Adler et al., 1973; Adler and Trombka, 1977; Clark and Trombka, 1997a; Nittler et al., 2001; Grande et al., 2001, 2003; Okada et al., 2006; Schlemm et al., 2007; Okada et al., 2008; Fraser et al., Forthcoming), where there are no atmospheres to absorb the low energy incident and fluorescent X-rays, and where the solar flux is sufficiently high (Yin et al., 1993). XRF spectroscopy was first successfully demonstrated on the Moon by the Russian Luna 12 mission in 1968 (Mandel'Shtam et al., 1968), and the 1971 Apollo 15 and the 1972 Apollo 16 missions carried simple proportional counter experiments (Adler et al., 1972a, 1972b), measuring the X-ray photon count-rate from a limited area of the lunar surface (Adler et al., 1973). These data sets provided an initial understanding of the variable geochemistry of the lunar surface, paving the way for a new generation of lunar X-ray spectrometers. Note that the incident solar X-rays only penetrate into the upper few microns of a planetary surface, typically producing fluorescent X-rays from the outer layers of individual mineral grains (Clark and Trombka, 1997b).

The D-CIXS instrument (Fig. 1a, Grande et al., 2003; Dunkin et al., 2003) demonstrated a new approach to building miniaturized X-ray detectors, based around the use of innovative swept charge device (SCD) solid-state detectors (Holland et al., 2004). D-CIXS used 24 SCD detectors mounted in three facets consisting of eight detectors each. In an attempt to cover as much of the lunar surface as possible, these facets pointed in different directions—the central facet (Facet 2) pointed towards the spacecraft nadir, while adjacent facets (1 and 3) were angled by $\pm 10^\circ$ with respect to this (Fig. 1b). Each detector was equipped with a collimator giving a field of view of 8° for the central facet and 12° for the other two. Each collimator assembly on Facet 1 and 2 included two Al-filters (each $0.2\ \mu\text{m}$ thick) to prevent light and low energy electrons from interacting with the SCDs. Facet 3 was also covered with a Mg filter, making these detectors relatively more sensitive to Mg fluorescence at low energy as the Al line is blocked (transmission at 1.49 keV is $\sim 1/20$ that of Mg) and the Si line is also very attenuated (transmission at 1.74 keV is $\sim 1/4$ that of Mg); mapping the distribution of Mg on the lunar surface was a high scientific priority for D-CIXS (Dunkin et al., 2003). D-CIXS was accompanied by an X-ray solar monitor (XSM) designed to monitor the solar input X-ray flux (Huovelin et al., 2002).

While successfully demonstrating the technology, the scientific results from D-CIXS (Grande et al., 2007) were limited by (i) the large and variable lunar footprint resulting from SMART-1's high, elliptical orbit ($\sim 300 \times \sim 3000$ km); (ii) radiation damage to the detectors during the long (15 month) journey to the Moon through the Earth's energetically charged particle belts; and (iii) unanticipated instrument and pre- and post-launch calibra-

tion problems (Grande et al., 2007). In addition to these operational constraints, D-CIXS orbited the Moon during a period (2005–2006) of very low solar activity (approaching the 2007 solar minimum), which both limited the X-ray signal and restricted the surface coverage to localities that were over flown during flare events. Even during solar flares other issues could cause the data to be difficult to interpret for one or more of the following reasons: (a) the observation viewing geometry was poor (i.e. near the lunar terminator); (b) the SCDs were flooded by incoming particles (electrons, protons, etc.) from the Sun, swamping any lunar XRF signal; (c) the instrument was turned off due to spacecraft temperature issues; or (d) sporadic interference of the SCD data processing produced a 'double peaked' spectrum which was difficult to retrospectively deconvolve.

During the mission, it also became clear that some individual detectors performed much better than others; in particular detectors 0 and 6 on Facet 1 displayed the lowest noise and narrowest spectral response. All observations reported here are based on X-ray flux measured by these two detectors. Calibration of the instrument response versus energy was carried out in flight using the Crab nebula as a calibration standard (Grande et al., 2007). This observation was only possible on Facet 2 (with aluminium filters), but, as the general shape of the response was similar between the detectors on Facet 2 and Facet 1, this response curve is taken as the average calibration for Facet 1 as well; no in-flight response calibration was possible for Facet 3 and these data are not considered calibrated.

The entire D-CIXS dataset has now been examined and a set of flare events during the lunar science mission were selected for analysis based upon their having suitable data with strong low-energy (Mg, Al and Si) lines and a line feature at ~ 3.7 keV associated with the Ca $K\alpha$ line (Grande et al., 2007). Observations on the following two dates are of primary interest, as they coincide with large flares (M-class or above: Table 1) and contain suitable data for initial science analysis.

2. Observations

2.1. 'Farside flare' on July 27th 2005

An M1 to M2 class flare occurred between 04:45 and 04:52 UT when SMART-1 was orbiting over the central portion of the lunar farside Feldspathic Highlands Terrane ('FHT'; Fig. 2, Table 1). This region of the Moon is thought to be dominated by ferroan anorthosite (FAN) lithologies, representing primary crust formed at ~ 4.5 Ga during lunar differentiation (Taylor, 1982; Taylor et al., 1991; Jolliff et al., 2000). The terrane is heavily cratered,

Table 1
Viewing geometry solar flare state for the observations discussed in the text.

Time (UT)	Altitude (km)	Latitude (deg.)	Longitude (deg.)	Solar incidence angle (°)	GOES (XL Band)	GOES (XS Band)	Flare state
<i>Nearside flare (18th November 2005)</i>							
00:25	1014	−15.83	−23.38	14.93	1.54E-06	7.73E-08	C2
00:26	1037	−14.03	−23.51	13.07	1.77E-06	1.09E-07	C2
00:27	1060	−12.22	−23.67	10.97	2.72E-06	2.45E-07	C2
00:28	1084	−10.39	−23.86	9.19	4.28E-06	5.50E-07	C4
00:29	1108	−8.54	−24.06	7.34	6.15E-06	9.62E-07	C6
00:30	1133	−6.67	−24.36	5.25	8.05E-06	1.38E-06	C8
00:31	1157	−4.78	−24.46	3.38	1.02E-05	1.91E-06	M1
00:32	1182	−2.86	−24.65	1.94	1.19E-05	2.28E-06	M1
<i>Farside flare (27th July 2005)</i>							
04:45	1373	37.88	−136.93	70.33	1.05E-05	1.71E-06	M1
04:46	1344	36.33	−137.10	70.19	1.26E-05	2.11E-06	M1
04:47	1316	34.75	−137.27	70.04	2.47E-05	2.50E-06	M1
04:48	1287	33.15	−137.42	69.89	1.65E-05	2.90E-06	M2
04:49	1259	31.52	−137.57	69.61	1.85E-05	3.30E-06	M2
04:50	1230	29.86	−137.71	69.33	2.06E-05	3.67E-06	M2
04:51	1202	28.17	−137.85	69.04	2.25E-05	4.02E-06	M2
04:52	1173	26.45	−137.98	68.76	2.43E-05	4.63E-06	M2

Lunar coordinates and altitudes are given for the centre of Facet 1. The solar incidence angle is measured with respect to the surface normal. GOES XL (4.5 Å) and XS (1.75 Å) band fluxes are measured in W m^{-2} .

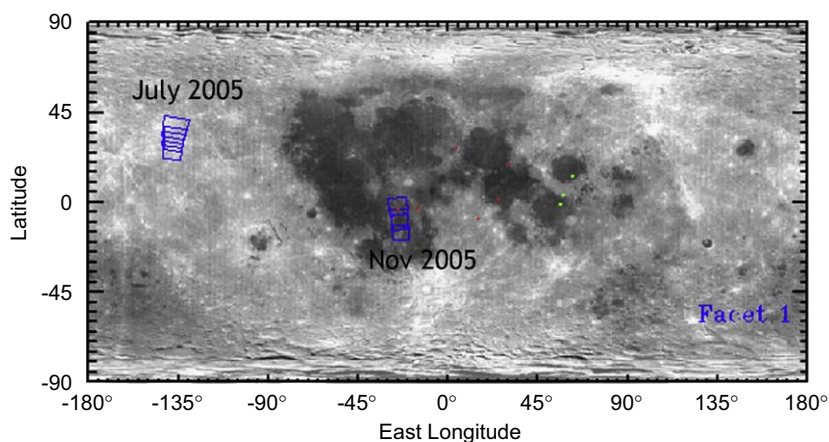


Fig. 2. Surface footprints of D-CIXS during the ‘farside’ (July 2005) and ‘nearside’ (November 2005) flare events discussed in this paper. Latitudes and Longitudes are provided in Table 1. Red points illustrate Apollo landing sites on the near-side of the Moon, and green points indicate the locality of the Luna sample return landing sites on the near-side Eastern limb. (For interpretation of the references to colour in this figure legend, the reader is referred to the web version of this article.)

but low-Fe concentrations (generally <7 wt% FeO) measured by Lunar Prospector (Lawrence et al., 2003) indicate that these impacts did not excavate mafic lower crustal rocks; modelling (Wieczorek et al., 2006) indicates a crustal thickness of 60–100 km in this region.

The X-ray spectrum for this flare is shown in Fig. 3 as the combined time-averaged spectra from detectors 0 and 6 on Facet 1. To determine the nature of the material giving rise to this spectrum, we have employed a forward modelling technique based on the method discussed in Clark and Trombka (1997b); further details of our modelling methods will be provided elsewhere (Swinyard et al., in preparation). The modeling requires knowledge of the incident solar spectrum from the flare (Clark and Adler, 1978; Clark and Trombka, 1997b). During the period of the flares, the XSM was not operational due to count rate saturation from the solar X-ray flux. Instead, we use X-ray flux data from the Geostationary Operational Environment Satellites (GOES: <http://sxi.ngdc.noaa.gov/>) for the period of the observation. From the GOES data, a flare temperature and brightness was

derived that was used to construct a featureless spectrum based on the method described in Mewe et al. (1985). During the period of the observation, the flare temperature only varied by 10%, and although the overall intensity increased significantly, the normalisation procedure described below accounted for this: we therefore used the flare conditions at the end of the observation period, 00:52 UT, as representative of those prevalent during the entire observation. The model flare spectrum, together with the knowledge of the solar aspect angle (Table 1), was used to derive both the line flux and the Thomson-scattered X-ray flux. We have used a featureless spectrum as the absence of spectral information from the XSM, makes estimation of the line contribution difficult to assess. The only significant flare feature that is likely to impact on the model results is the Fe complex around 6.7 keV. Reuven Ramaty High Energy Solar Spectroscopic Imager (RHESSI) observations and comparisons to model predictions show that although the line intensity can vary considerably over the duration of a flare, the line to continuum for this line from flares in the $10\text{--}20 \times 10^6$ K temperature range, typical for an M-class

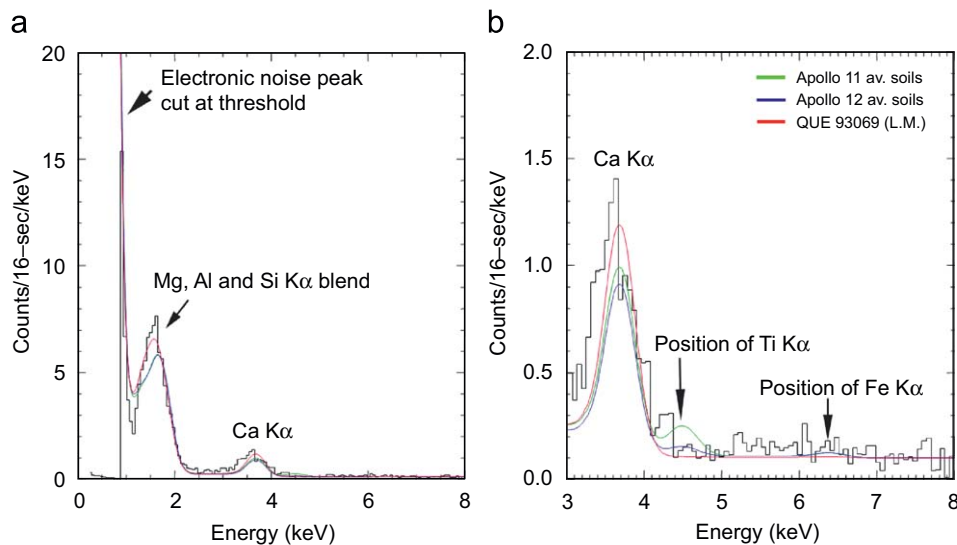


Fig. 3. Co-added spectra from detector 0 and detector 6 from the 27th July farside flare event (2005-07-27, UT 04:45 to 04:54) overlain with model predictions based on the composition of Apollo 11 (green), Apollo 12 (blue) soils and the feldspathic lunar meteorite (L.M.) QUE 93069 (red). (a) Full spectrum from 0 to 8 keV. (b) Scaled close-up of measured X-ray flux and models from 3 to 8 keV, illustrating the Ca $K\alpha$ peak (3.7 keV). Note that, as expected for the farside, the model using lunar meteorite QUE 93069 gives the best agreement; the compositions adopted for the models are listed in Table 2. (For interpretation of the references to colour in this figure legend, the reader is referred to the web version of this article.)

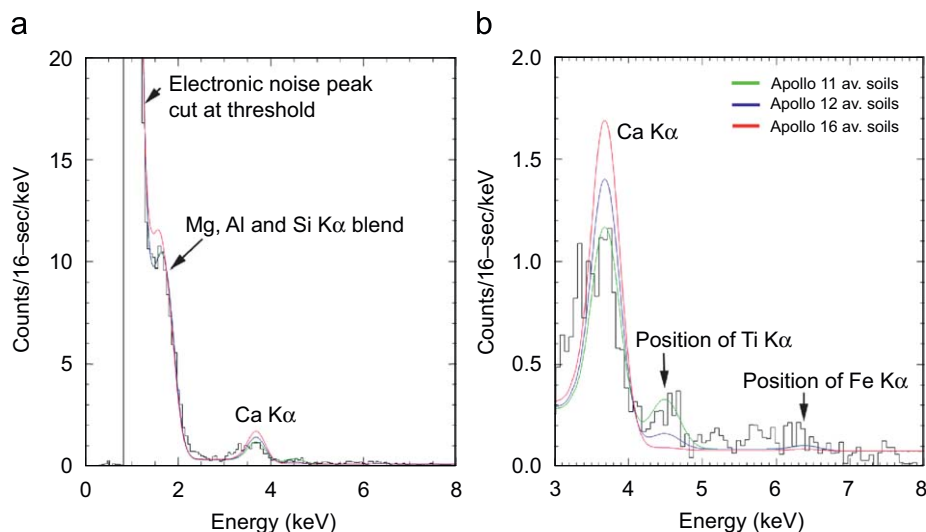


Fig. 4. Co-added spectra from detector 0 and detector 6 from the 18th November near-side flare event (2005-11-18, UT 00:28 to 00:32) overlain with model predictions of Apollo 11 (green), Apollo 12 (blue) and Apollo 16 (red) average soil compositions (Table 2). (a) Full spectrum from 0 to 8 keV. (b) Linear scaled close up of measured X-ray flux and models from 3 to 8 keV, illustrating the fit to the Ca $K\alpha$ peak (3.7 keV) and a Ti $K\alpha$ peak (4.5 keV). Note that the Ti concentration is intermediate between the Apollo 11 and Apollo 12 compositions; a least-variance fit to the data yields a Ti abundance of 3 ± 2 wt% (see text for details). (For interpretation of the references to colour in this figure legend, the reader is referred to the web version of this article.)

flare is never more than 10:1 (Phillips et al., 2006). Adding a line with intensity of 10 times the local continuum at the location of the Fe $K\alpha$, had no significant impact on the results for the predicted lunar fluorescence spectrum, showing that the approximation of using a featureless spectrum appears valid.

The model scattered solar continuum and fluorescent line fluxes were co-added, multiplied by the detector response versus energy derived from the Crab nebula, and convolved with an instrument spectral response function. This consisted of a 420 eV full width at half maximum (FWHM) Gaussian portion centred on the line energies plus a pedestal section corresponding to charge collection efficiency loss characteristic of the SCDs. The proportion of Gaussian to pedestal counts varies as a function of energy between 0.5 (at Mg, Al and Si) to ~ 0.2 at Fe. A noise peak is added at low energies with the position and height varied to fit the noise

tail in the data and an overall fixed particle background is added to make the model coincide with the data at energies > 10 keV. The latter was always between 0.05 and 0.1 counts/channel in 16 s integrations. Finally the model X-ray and noise spectrum, before addition of the particle background, was normalised to the data at the location of the Si $K\alpha$ line at 1.74 keV. This process was carried out iteratively to ensure the noise peak in the model spectrum, matched the data. The apparent mismatch between the data and the model for the red (Apollo 16 type—see below) curve in Fig. 4 is due to the difference in magnesium concentration, not to a difference in the normalisation procedure. The same difference can be seen in Fig. 3, where the Apollo 16 model fits the data rather better than 11 or 12, but the noise peak for this spectrum was at a lower effective energy causing less interference with the fitting procedure.

Table 2

Geological compositions (elemental wt%) used for the X-ray modelling shown in Figs. 3 and 4.

Element wt%	Average bulk soils			Lunar meteorite
	Apollo 11	Apollo 12	Apollo 16	QUE 93069
Si	19.63	21.60	20.98	20.90
Ti	4.76	1.57	0.32	0.17
Al	6.66	6.42	14.41	15.50
Fe	12.75	13.36	3.87	3.24
Mg	4.78	6.28	3.62	2.70
Ca	8.39	7.04	10.41	11.80
Na	0.17	0.15	0.17	0.24
O	41.91	42.40	44.88	45.22
Total	99.05	98.82	98.66	99.77

The Apollo compositions are taken from bulk average landing site soil compositions as listed by Haskin and Warren (1991). Lunar meteorite QUE 93069 was selected as a best match to the composition of the lunar far side Feldspathic Highlands Terrane, and its bulk element bulk composition was taken from Warren et al. (2005).

The modelled line flux data were generated using the average composition (in elemental weight % concentrations) of Apollo landing site soils and lunar meteorites (Table 2, see also Korotev, 2005). The results of the model for Apollo 11 and Apollo 12 soils and a feldspathic lunar meteorite (QUE 93069; bulk composition taken from Warren et al., 2005) are overlaid on the data in Fig. 3. Whilst deriving concentration ratios is hampered by the poor spectral resolution of the instrument, these models indicate that a surficial regolith composition rich in aluminium and calcium (i.e. similar to lunar FAN meteorite QUE 93069) is required to best match the profile of the blended low-energy lines and the Ca K α peak. The non-detection of Ti and Fe (Fig. 3b) in these data is also consistent with the expected Al-rich, Fe-poor, Ti-poor nature of the FHT inferred from interpretations of other remote sensing missions (Jolliff et al., 2000; Lucey et al., 2000; Prettyman et al., 2006).

2.2. 'Nearside flare' on the November 18th, 2005

The observations were made during a C2 to M1 class flare between 00:25 and 00:32 UT, when SMART-1 was over-flying the southern-central portion of the lunar near-side (Fig. 2, Table 1). The Facet 1 footprint included a mixed highlands-mare region south of and through Mare Cognitum, and over the Apollo 12 landing site area (Fig. 2). The co-added X-ray spectrum for this whole flare period, as measured by detectors 0 and 6, is shown in Fig. 4. Again, we have overlaid model spectra using the same method as described above and using the relevant viewing geometries and solar conditions listed in Table 1; the illustrated input model compositions used are average Apollo 11, 12 and 16 soils (Table 2). The flare temperature and intensity varied over the period of the observation. We elected to take the midpoint of the flare at 00:29 UT as representative of the average conditions during the observation (C6 class flare conditions: Table 1).

The low-energy lines (Mg, Al and Si) are best matched by models (Fig. 4a) with similar amounts of Mg and Al to the Apollo 11 and 12 soils (where Mg/Al = 0.72 and 0.98, respectively; Table 2), rather than compositions that are poorer in Mg and richer in Al (like the Apollo 16 site soils, where Mg/Al = 0.25; Table 2). Moreover, the Ca K α line flux (Fig. 4b) is most similar to models with lower Ca abundances (i.e. appropriate for mare soils), compared with regoliths dominated by feldspathic material (i.e. Apollo 16 FAN-rich compositions). Significantly, and reported

here for the first time for lunar XRF observations, we have clearly observed a feature at 4.5 keV coincident with the Ti K α line. The signal-to-noise at the centre of the feature is ~ 4 . We have performed a minimised variance fit to this feature and found that detection is at a confidence level of $>95\%$ (i.e. there is only a 5% chance of 0% concentration being compatible with the measurement). There is some evidence of an excess at the location of the Fe K α line, which is above the prediction of the model due to fluorescence from the lunar surface alone; however, the low count rate and the presence of a noise excess over the 5–7 keV range, both in this and the far side spectrum, means that no real statistical certainty can be associated to the feature. The noise excess is not understood but is most likely due to the penetrating background events. (We note that D-CIXS was able to detect an Fe-line feature in much higher solar M-class and low X-flare observations of Mare Crisium, as discussed in Grande et al., 2007).

The minimum variance D-CXS Ti concentration is found to be 3 ± 2 wt% Ti (5 ± 3 wt% TiO₂). For comparison, the average Ti concentration obtained by the Lunar Prospector gamma-ray instrument is 1.95 ± 0.42 Ti wt% (1 standard deviation based on averaging 5° per pixel data within the D-CIXS footprints using data from the Prettyman et al., 2006 dataset), while that derived from Clementine using the Lucey et al., 2000 algorithm, and converting TiO₂ to Ti concentrations was 2.5 ± 0.9 wt% Ti (1 standard deviation based on averaging Clementine 1° per pixel data within the D-CIXS observation footprints). The D-CIXS value presented here is consistent with both these previous measurements and is similar to, although slightly higher than (probably as our field of view extends to mare regions beyond the landing site) the average Ti content (Table 2) of the Apollo 12 soils (1.57 ± 0.06 wt% Ti; Haskin and Warren, 1991).

3. Conclusions

This demonstration of a successful Ti concentration measurement is especially important given that Ti content is one of the primary diagnostics of mare basalt petrogenesis (Neal and Taylor, 1992). Although the Lunar Prospector and Clementine values are in good agreement in the region observed here; in general, significant discrepancies exist between these two data sets (e.g. Elphic et al., 2001) and XRF spectroscopy provides an independent means of determining the abundance of this important element. While, for the reasons outlined above, the spatial coverage and signal-to-noise ratio of the D-CIXS measurements are such that they cannot add significantly to the Clementine and Prospector results, they do augur well for the higher quality data expected from future instruments (see below).

Although the scientific results of D-CIXS were limited to favourable conditions, the instrument did fulfil its function as a technology demonstrator. Indeed, experience with D-CIXS has led to a significantly improved design for a similar instrument, the Chandrayaan-1 X-ray spectrometer (C1XS) that is now in orbit around the Moon onboard India's Chandrayaan-1 mission. C1XS will be a scientifically more powerful instrument than D-CIXS for several reasons (Crawford et al., 2009; Grande, 2009): (1) the short travel-time (c. 17 days) means that the detectors will be exposed to only 1% of the radiation damage that occurred in D-CIXS (based on laboratory calibrations, we anticipate an energy resolution of about 110 eV (at Al-K α at $< -20^\circ\text{C}$) rather than 420 eV for the D-CIXS data presented here); (2) Chandrayaan-1's low circular orbit ($100 \times 100 \text{ km}^2$) will result in higher spatial resolution of the lunar surface ($\sim 25 \text{ km}$ FWHM compared to 60–600 km for D-CIXS); (3) C1XS will operate during a more active period of the solar cycle, resulting in higher X-ray fluxes and greater sensitivity to compositional variations; and (4)

experience gained with D-CIXS has ensured that many of the instrumental and calibration problems have been eliminated from C1XS. Based on activity during previous cycles, we anticipate that more than 80% of the C1XS footprints will be illuminated at some time over a two-year mission by flare levels of C1 or above, permitting good detections of Mg, Al, Si, Ca, Ti and Fe (see Fig. 3 of Crawford et al., 2009). The latter two elements will be detectable, whenever its concentration in the surface is greater than about 1 wt% (as discussed in Section 3.5 of Crawford et al., 2009), facilitating the mapping and classification of mare basalt lava flows on a 25 km spatial scale. For these reasons, and largely building on the legacy of D-CIXS, we anticipate that C1XS will realise the full potential of lunar XRF spectroscopy and make significant contributions to lunar science.

Acknowledgements

We acknowledge the contributions of the entire D-CIXS team, the SMART-1 teams from ESA/ESTEC project, industrial teams, STOC Science and Technology Operations Centre and ESOC spacecraft operations, for their dedicated work in developing and navigating the spacecraft to reach the Moon and operation of the instruments. The D-CIXS instrument development was supported with SMART-1 funding from ESA Science and Technology Research Programmes, and funding sources (BNSC, RAL, PPARC/STFC). Additional hardware was provided by CESR, Toulouse, University of Helsinki observatory and IRF Kiruna, Sweden. We acknowledge exchange with instruments teams from SMART-1 Science and Technology Working Team (STWT). We also would like to thank the two anonymous reviewers, whose helpful comments improved the quality of this manuscript.

References

- Adler, I., Trombka, J.I., 1977. Orbital chemistry—lunar surface analysis from the X-ray and gamma ray remote sensing experiments. *Phys. Chem. Earth* 10, 17.
- Adler, I., Trombka, J., Gerard, J., Lowman, Schmadebeck, R., Blodget, H., Eller, E., Yin, L., Lamothe, R., Gorenstein, P., Björkholm, P., 1972a. Apollo 15 geochemical X-ray fluorescence experiment—preliminary report. *Science* 175, 436.
- Adler, I., Trombka, J., Gerard, J., Lowman, P., Schmadebeck, R., Blodget, H., Eller, E., Yin, L., Lamothe, R., Osswald, G., Gorenstein, P., Björkholm, P., Gursky, H., Harris, B., 1972b. Apollo 16 geochemical X-ray fluorescence experiment—preliminary report. *Science* 177, 256.
- Adler, I., Trombka, J.I., Lowman, P., Schmadebeck, R., Blodget, H., Eller, E., Yin, L., Lamothe, R., Osswald, G., Gerard, J., Gorenstein, P., Björkholm, P., Gursky, H., Harris, B., Arnold, J., Metzger, A., Reedy, R., 1973. Apollo 15 and 16 results of the integrated geochemical experiment. *The Moon* 7, 487.
- Andre, C.G., Bielefeld, M.J., Eliason, E., Soderblom, L.A., Adler, I., Philpotts, J.A., 1977. Lunar surface chemistry: a new imaging technique. *Science* 197, 986.
- Clark, P.E., Hawke, B.R., 1981. Compositional variation in the Hadley Apennine region. *Proc. Lunar Planet. Sci. Conf. 12th*, 727.
- Clark, P.E., Hawke, B.R., 1991. The lunar farside: the nature of the highlands east of Smythii. *Earth, Moon Planets*, 93 (appropriate for).
- Clark, P.E., Trombka, J.I., 1997a. Remote X-ray fluorescence experiments for future missions to Mercury. *Planet. Space Sci.* 45, 57.
- Clark, P.E., Trombka, J.I., 1997b. Remote X-ray spectrometry for NEAR and future missions: modeling and analyzing X-ray production from source to target. *J. Geophys. Res.* 102, 16631.
- Clark, P.E., Adler, I., 1978. Utilization of independent solar flux measurements to eliminate nongeochemical variation in X-ray fluorescence data. *Proc. Lunar Planet. Sci. Conf. 9th* 3, 3029.
- Crawford, I.A., Joy, K.H., Kellett, B.J., Grande, M., Anand, M., Bhandari, N., Cook, A.C., d'Uston, L., Fernandes, V.A., Gasnault, O., Goswami, J., Howe, C.J., Huovelin, J., Koschny, D., Lawrence, D.J., Maddison, B.J., Maurice, S., Narendranath, S., Pieters, C., Okada, T., Rothery, D.A., Russell, S.S., Sreekumar, P., Swinyard, B., Wieczorek, M., Wilding, M., 2009. The Scientific Rationale for the C1XS X-Ray Spectrometer on India's Chandrayaan-1 Mission to the Moon. *Planet. Space Sci.* (2009) in press, doi:10.1016/j.pss.2008.12.006.
- Dunkin, S.K., Grande, M., Casanova, I., Fernandes, V., Heather, D.J., Kellett, B., Muinonen, K., Russell, S.S., Browning, R., Waltham, N., Parker, D., Kent, B., Perry, C.H., Swinyard, B., Perry, A., Feraday, J., Howe, C., Phillips, K., McBride, G., Huovelin, J., Muhli, P., Hakala, P.J., Vilhu, O., Thomas, N., Hughes, D., Alleyne, H., Grady, M., Lundin, R., Barabash, S., Baker, D., Clark, P.E., Murray, C.D., Guest, J., d'Uston, L.C., Maurice, S., Foing, B., Christou, A., Owen, C., Charles, P., Laukkanen, J., Koskinen, H., Kato, M., Sipila, K., Nenonen, S., Holmstrom, M., Bhandari, N., Elphic, R., Lawrence, D., 2003. Scientific rationale for the D-CIXS X-ray spectrometer on board ESA's SMART-1 mission to the Moon. *Planet. Space Sci.* 51, 435.
- Elphic, R.C., Lawrence, D.J., Maurice, S., Feldman, W.C., Barraclough, B.L., Gasnault, O.M., Binder, A.B., Lucey, P.G., Blewett, D.T., 2001. Lunar Prospector neutron measurements and lunar TiO₂. *Lunar Planet. Sci. Conf. XXXII Abstract #1487*.
- Foing, B.H., Racca, G.D., Marini, A., Evrard, E., Stagnaro, L., Almeida, M., Koschny, D., Frew, D., Zender, J., Heather, J., Grande, M., Huovelin, J., Keller, H.U., Nathues, A., Josset, J.L., Malkki, A., Schmidt, W., Noci, G., Birk, R., Less, L., Sodnik, Z., McManamon, P., 2006. *Adv. Space Res.* 37, 6.
- Fraser, G.W., Carpenter, J.D., Rothery, D.A., Pearson, J.F., Huovelin, J., Treis, J., Anttila, M., Ashcroft, M., Benkoff, J., Bowyer, A., Bradley, A., Bridges, J., Brown, C., Bulloch, C., Bunce, E.J., Christensen, U., Evans, M., Fairbend, R., Feasey, M., Giannini, F., Hermann, S., Hesse, M., Hilchenbach, M., Jordan, T., Joy, K., Kaipiainen, M., Kitchingman, I., Lechner, P., Lutz, G., Malkki, A., Martindale, A., Muinonen, K., Näränen, J., Portin, P., Prydderch, M., San Juan, J., Sclater, E., Schyns, E., Stevenson, T.J., Strüder, L., Syrjasuo, M., Talboys, D., Thomas, P., Whitford, C., Whitehead, S., forthcoming. The Mercury Imaging X-ray Spectrometer (MIXS) on BepiColombo. *Planet. Space Sci.*, in revision.
- Grande, M., Dunkin, S.K., Kellett, B., 2001. Opportunities for X-ray remote sensing at Mercury. *Planet. Space Sci.* 49, 1553.
- Grande, M., Browning, R., Waltham, N., Parker, D., Dunkin, S.K., Kent, B., Kellett, B., Perry, C.H., Swinyard, B., Perry, A., Feraday, J., Howe, C., McBride, G., Phillips, K., Huovelin, J., Muhli, P., Hakala, P.J., Vilhu, O., Laukkanen, J., Thomas, N., Hughes, D., Alleyne, H., Grady, M., Lundin, R., Barabash, S., Baker, D., Clark, P.E., Murray, C.D., Guest, J., Casanova, I., d'Uston, L.C., Maurice, S., Foing, B., Heather, D.J., Fernandes, V., Muinonen, K., Russell, S.S., Christou, A., Owen, C., Charles, P., Koskinen, H., Kato, M., Sipila, K., Nenonen, S., Holmstrom, M., Bhandari, N., Elphic, R., Lawrence, D., 2003. The D-CIXS X-ray mapping spectrometer on SMART-1. *Planet. Space Sci.* 51, 427.
- Grande, M., Kellett, B.J., Howe, C., Perry, C.H., Swinyard, B., Dunkin, S.K., Huovelin, J., Alha, L., d'Uston, L.C., Maurice, S., Gasnault, O., Couturier-Doux, S., Barabash, S., Joy, K.H., Crawford, I.A., Lawrence, D., Fernandes, V., Casanova, I., Wieczorek, M., Thomas, N., Mall, U., Foing, B., Hughes, D., Alleyne, H., Russell, S.S., Grady, M., Lundin, R., Baker, D., Murray, C.D., Guest, J., Christou, A., 2007. The D-CIXS X-ray spectrometer on the SMART-1 mission to the moon—first results. *Planet. Space Sci.* 55, 494.
- Grande, M., Maddison, B.J., Howe, C.J., Kellett, B.J., Sreekumar, P., Huovelin, J., Crawford, I.A., Duston, C. L., Smith, D., Anand, M., Bhandari, N., Cook, A., Erd, C., Fernandes, V., Foing, B., Gasnault, O., Goswami, J.N., Holland, A., Joy, K.H., Kochney, D., Lawrence, D., Maurice, S., Narendranath, S., Okada, T., Pieters, C., Rothery, D., Russell, S.S., Shrivastava, A., Swinyard, B.M., Wieczorek, M., Wilding, M., 2009. The C1XS X-ray spectrometer on Chandrayaan-1. *Planet. Space Sci.* (2009), in press, doi:10.1016/j.pss.2009.01.016.
- Haskin, L., Warren, P., 1991. Lunar chemistry. In: Heiken, G.H., Vaniman, D., French, B.M. (Eds.), *Lunar Sourcebook: A user's Guide to the Moon*. Cambridge University Press, Cambridge, p. 357.
- Holland, A.D., Hutchinson, I.B., Smith, D.R., Pool, P., 2004. Photon damage in the E2V swept charge device. *Nucl. Instrum. Methods Phys. Res.* 521, 393.
- Huovelin, J., Alha, L., Andersson, H., Andersson, T., Browning, R., Drummond, D., Foing, B., Grande, M., Hämäläinen, K., Laukkanen, J., Lämsä, V., Muinonen, K., Murray, M., Nenonen, S., Salminen, A., Sipilä, H., Taylor, I., Vilhu, O., Waltham, N., Lopez-Jorkama, M., 2002. The SMART-1 X-ray solar monitor (XSM): calibrations for D-CIXS and independent coronal science. *Planet. Space Sci.* 50, 1345.
- Jolliff, B.L., Gillis, J.J., Haskin, L.A., Korotev, R.L., Wieczorek, M.A., 2000. Major lunar crustal terranes: surface expressions and crust-mantle origins. *J. Geophys. Res.* 105, 4197.
- Korotev, R.L., 2005. Lunar geochemistry as told by lunar meteorites. *Chem. Erde* 65, 297.
- Lawrence, D.J., Feldman, W.C., Elphic, R.C., Little, R.C., Prettyman, T.H., Maurice, S., Lucey, P.G., Binder, A.B., 2002. Iron abundances on the lunar surface as measured by the Lunar Prospector gamma-ray and neutron spectrometers. *J. Geophys. Res.* 107, 5130.
- Lawrence, D.J., Elphic, R.C., Feldman, W.C., Prettyman, T.H., Gasnault, O., Maurice, S., 2003. Small-area thorium features on the lunar surface. *J. Geophys. Res.* 108, 5102.
- Lucey, P.G., Blewett, D.T., Hawke, B.R., 1998. Mapping the FeO and TiO₂ content of the lunar surface with multispectral imagery. *J. Geophys. Res.* 103, 3679.
- Lucey, P.G., Blewett, D.T., Jolliff, B.L., 2000. Lunar iron and titanium abundance algorithms based on final processing of Clementine ultraviolet-visible images. *J. Geophys. Res.* 105, 20297.
- Lucey, P.G., 2004. Mineral maps of the moon. *Geophys. Res. Lett.* 31, L08701.
- Mandel'Shtam, S.L., Tindo, I.P., Cheremukhin, G.S., Sorokin, L.S., Dmitriev, A.B., 1968. Lunar X-ray and the cosmic X-ray background measured by the lunar satellite LUNA-12. *Cosmic Res.* 6, 100.
- Mewe, R., Gronenschild, E.H.B.M., van den Oord, G.H.J., 1985. Calculated X-radiation from optically thin plasmas. *V. Astron. Astrophys. Suppl.* 62, 197.
- Neal, C.R., Taylor, L.A., 1992. Petrogenesis of mare basalts: a record of lunar volcanism. *Geochim. Cosmochim. Acta* 56, 2177.
- Nittler, L.R., Starr, R.D., Lim, L., McCoy, T.J., Burbine, T.H., Reedy, R.C., Trombka, J.I., Gorenstein, P., Squyres, S.W., Boynton, W.V., McClanahan, T.P., Bhangoo, J.S., Clark, P.E., Murphy, M.E., Killen, R., 2001. X-ray fluorescence measurements of the surface elemental composition of asteroid 433 Eros. *Meteorit. Planet. Sci.* 36, 1673.

- Okada, T., Shirai, Kei, Yamamoto, Y., Arai, T., Ogawa, K.i., Hosono, K., Kato, M., 2006. X-ray fluorescence spectrometry of asteroid Itokawa by Hayabusa. *Science* 312, 1338.
- Okada, T., Shirai, K., Yamamoto, Y., Arai, T., Ogawa, K., Shiraishi, H., Iwasaki, M., Kawamura, T., Morito, H., Kato, M., The SELENE XRS Team, 2008. X-ray fluorescence experiments on the SELENE (KAGUYA) spacecraft. 39th Annu. Lunar Planet. Sci. Conf. Abstract #1960.
- Pieters, C., Shkuratov, Y., Kaydash, V., Stankevich, D., Taylor, L., 2006. Lunar soil characterization consortium analyses: pyroxene and maturity estimates derived from Clementine image data. *Icarus* 184, 83.
- Phillips, K.J.H., Chifor, C., Dennis, B.R., 2006. RHESSI observations of the solar flare iron-line feature at 6.7 keV. *Astrophys. J.* 647, 1480.
- Prettyman, T.H., Hagerty, J.J., Elphic, R.C., Feldman, W.C., Lawrence, D.J., McKinney, G.W., Vaniman, D.T., 2006. Elemental composition of the lunar surface: analysis of gamma-ray spectroscopy data from Lunar Prospector. *J. Geophys. Res.—Planets* 111, E12007.
- Racca, G.D., Foing, B.H., Coradini, M., 2001. SMART-1: the first time of Europe to the moon. *Earth, Moon Planets* 85–86, 379.
- Schlemm II, C.E., Starr, R.D., Ho, G.C., Bechtold, K.E., Benedict, S.A., Boldt, J.D., Boynton, W.V., Bradley, W., Fraeman, M.E., Gold, R.E., Goldsten, J.O., Hayes, J.R., Jaskulek, S.E., Rossano, E., Rumpf, R.A., Schaefer, E.D., Strohhahn, K., Shelton, R.G., Thompson, R.E., Trombka, J.L., Williams, B.D., 2007. The X-ray spectrometer on the MESSENGER spacecraft. *Space Sci. Rev.* 131, 393.
- Shearer, C.K., Hess, P.C., Wieczorek, M.A., Pritchard, M.E., Parmentier, E.M., Borg, L., Longhi, J., Elkins-Tanton, L.T., Neal, C.R., Antonenko, I., Canup, R.M., Halliday, A.N., Grove, T.L., Hager, B.H., Less, D.-C., Wiechert, U., 2006. Thermal and magmatic evolution of the Moon. In: Jolliff, B.L., Wieczorek, M.A., Shearer, C.K., Neal, C.R. (Eds.), *New Views Moon. Rev. Mineral. Geochem.*, vol. 60, p. 365.
- Swinyard, B.M., et al., in preparation.
- Taylor, G.J., Warren, P., Ryder, G., Delano, J., Pieters, C., Lofgren, G., 1991. Lunar rocks. In: Heiken, G., Vaniman, D., French, B. (Eds.), *The Lunar Sourcebook: A User's Guide to the Moon*. Cambridge University Press, Cambridge, p. 183 (Chapter 6).
- Taylor, S.R., *Planetary Science: A Lunar Perspective*, 1982, Lunar Planet. Inst., Houston.
- Warren, P.H., Ulf-Møller, F., Kallemeyn, G.W., 2005. "New" lunar meteorites: impact melt and regolith breccias and large-scale heterogeneities of the upper lunar crust. *Meteorit. Planet. Sci.* 40, 989.
- Wieczorek, M.A., Jolliff, B.L., Khan, A., Pritchard, M.E., Weiss, B.P., Williams, J.G., Hood, L.L., Richter, K., Neal, C.R., Shearer, C.K., McCallum, I.S., Tompkins, S., Hawke, B.R., Peterson, C., Gillis, J.J., Bussey, B., 2006. The constitution and structure of the lunar interior. *Rev. Mineral. Geochem.* 60, 221.
- Yin, L.L., Trombka, J.L., Adler, I., Bielefeld, M., 1993. X-ray remote sensing techniques for geochemical analysis of planetary surfaces. In: Pieters, C.M., Englert, P.A. (Eds.), *Remote Geochemical Analysis: Elemental and Mineralogical Composition*. Cambridge University Press, Cambridge Website <<http://sxi.ngdc.noaa.gov/>> Last accessed 30th April 2008.

Remote X-ray fluorescence experiments for future missions to Mercury

P. E. Clark and J. I. Trombka

NASA/Goddard Space Flight Center, Code 691, Greenbelt, MD 20771, U.S.A.

Received 12 October 1995; revised 18 April 1996; accepted 12 June 1996

Abstract. To date, the only deep space mission to Mercury, Mariner 10, as well as ground-based observations have failed to provide direct measurements of that planet's composition. Such measurements are fundamental for the understanding of Mercury's origin and the inner solar system's history. The spin-stabilized Mercury Orbiter proposed for launch in the first or second decade of the twenty-first century as part of the ESA's Horizon 2000-plus plan could address this problem by including the X-ray spectrometer proposed here. X-ray spectrometers act as detectors for the X-ray emission induced by the solar flux incident on planetary surfaces. This emission is strongly dependent on the chemical composition of the surface as well as on the solar spectrum. Characteristic fluorescent lines, the most prominent being the K-alpha lines, are of sufficient intensity for major elements (Mg, Al, Si, Ca, Fe) to allow orbital measurement by remote X-ray detectors. The X-ray spectrometers described here will all have established heritage for space missions by 2000. These instruments have previously flown, are being flown as part of the NASA NEAR (Near Earth Asteroid Rendezvous) or Clark SSTI (Small Science and Technology Initiative) missions, or are now under development as part of NASA Facility Instrument Development Program. The instrument package would probably consist of an array of solid state detectors for surface measurements, as well as one which would act as a solar monitor. Calculations of anticipated results have been done for a variety of orbital and instrument configurations, and a variety of lunar soil compositions which could be analogous: anorthositic gabbro bearing soils from lunar highlands (Apollo 16), high-Mg basalt-rich soils from a KREEP-bearing area (Apollo 15), and mare basalt bearing soils (Apollo 12). The mission being considered here should result in maps of abundances of major elements, including Mg, Al, Si, Ca, and Fe, for much of Mercury's surface, with resolutions

ranging from tens to hundreds of kilometers depending on the element, the orbital eccentricity and altitude of the spacecraft. © 1997 Published by Elsevier Science Ltd. All rights reserved

Introduction/scientific objectives

Geochemical study of Mercury is essential in order to address a variety of fundamental questions, and yet, no direct measurements of Mercury's composition exist. Inferences about composition can in principle be drawn from ground-based spectral observations of planetary surfaces, but spectral observations of Mercury are extremely difficult to obtain as well as to interpret. The spin-stabilized Mercury Orbiter proposed for launch in 2011 or later as part of the ESA's Horizon 2000-plus plan could address this problem by including the X-ray spectrometer proposed here. We have already developed such an instrument as part of the NASA Facility Instrument Development Program, and such an instrument is now being flown on the NEAR mission to the asteroid 433 Eros (Trombka *et al.*, 1997). A similar instrument was already proposed for a Mercury mission by a NASA space physics working group in 1990 (Belcher *et al.*, 1991).

Such an XRS experiment would address the problem of Mercury's origin, and by implication, inner solar system history as follows: (1) Mercury is thought to have a complex early volcano-tectonic history. Major element abundance maps provided by this experiment would allow chemical characterization of a range of the more frequently occurring local geological features, such as craters, scarps, curvilinear rays, grabens, and the underlying stratigraphy exposed at the surface. (2) As yet, no clear association between mapped terranes and geochemical boundaries have been observed on Mercury; thus, the nature of geochemical differentiation, the extent of volcanism and the character of major terranes, have all been controversial. Maps of variations on regional scales, as well as compositional signatures for the major terranes would be provided by an orbital XRS instrument. (3) By

RADIATION ENVIRONMENT AT THE SURFACE

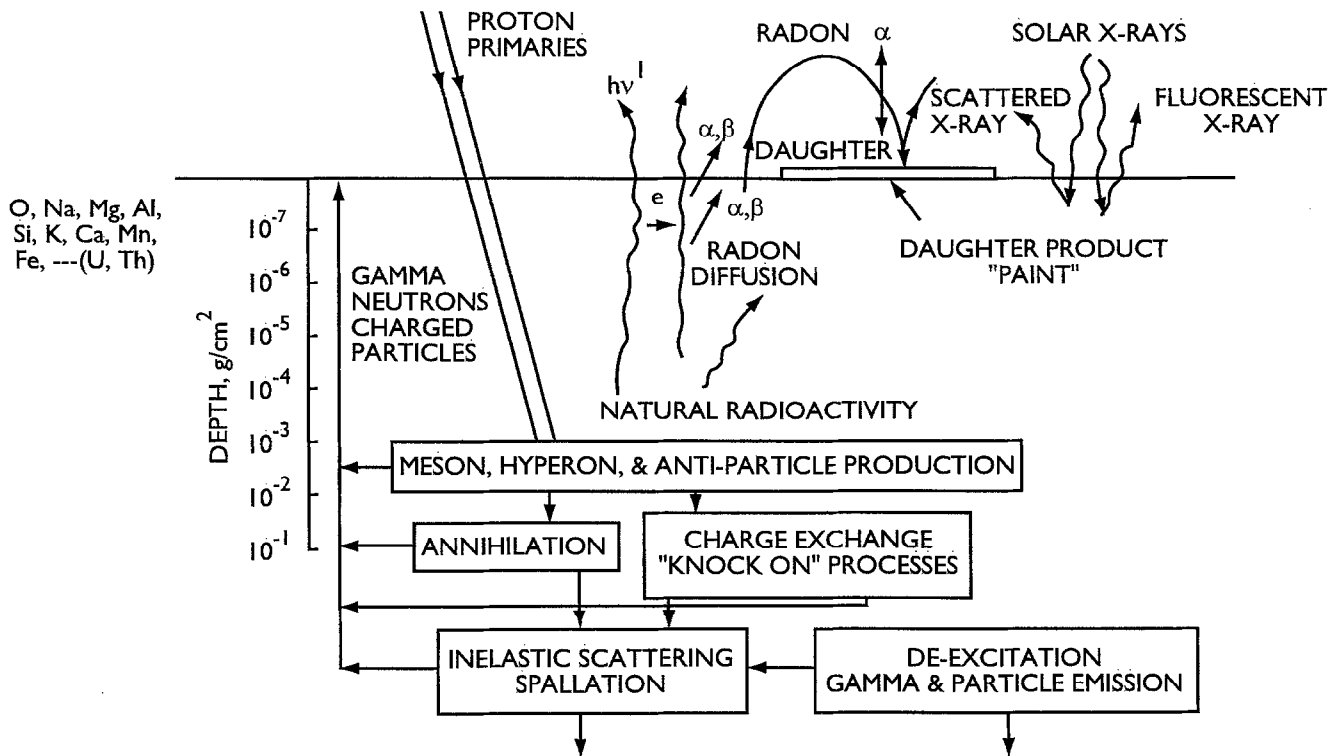


Fig. 1. X-ray and gamma-ray production at the surface of an atmosphereless body. This is a model for the high energy (X-ray and gamma-ray) surface environment for atmosphereless bodies, such as Mercury. Note the gamma-rays are generated at far greater depths (centimeters to meters) than the extremely surficial fluorescent or scattered X-rays (tens of micrometers to millimeters) which are far more readily attenuated

providing global averages for Mg, Al, Si, Ca, Fe abundances, this experiment would be instrumental in establishing which of the proposed models for Mercury's history is most credible, and in developing constraints on any newly considered mechanisms for planetary formation.

Principles of soft X-ray production in the solar system

The solar flux from 1 to 10 keV

X-ray spectrometers act as detectors for the X-ray emission induced by the solar flux incident on planetary surfaces, as illustrated in Fig. 1. This emission is strongly dependent on the chemical composition of the surface as well as on the solar spectrum (Clark and Adler, 1978; Clark, 1979, 1997). Characteristic fluorescent lines, the most prominent being the K-alpha lines for major elements (Mg, Al, Si, Ca, Fe at 1.25, 1.49, 1.75, 3.71, and 6.39 keV, respectively) are of sufficient intensity to allow orbital measurement by detectors such as the one described below. Solar X-rays also induce coherently and

incoherently scattered X-rays at the surface, which are considered background.

The solar flux from 1 to 10 keV, the energy region of interest, is a continuum which can be modeled by a four- to six-order power law (Zombeck, 1990), depending on the level of solar activity. In modeling the solar output, we have used the best estimates of solar output anticipated near the proposed time of launch (> 2011), which should be mid-cycle, ranging from approximately A5 to M1 levels (Clark, 1997). As Fig. 2 illustrates, the solar intensity decreases by three to four orders of magnitude from 1 to 10 keV; thus, fluorescent lines as well as the scatter-induced background have greater intensity at lower energies. As the level of solar activity increases, "hardening" occurs: relatively more output occurs at higher energies, the slope of the spectrum becomes less steep, and the overall magnitude of the X-ray flux increases. As Fig. 3 illustrates, solar output is highly variable, and can change typically by an order of magnitude within minutes, or four orders of magnitude within hours (Crosby *et al.*, 1996). In fact, we depend on periods of higher solar activity to achieve better statistics, shorter integration times, and

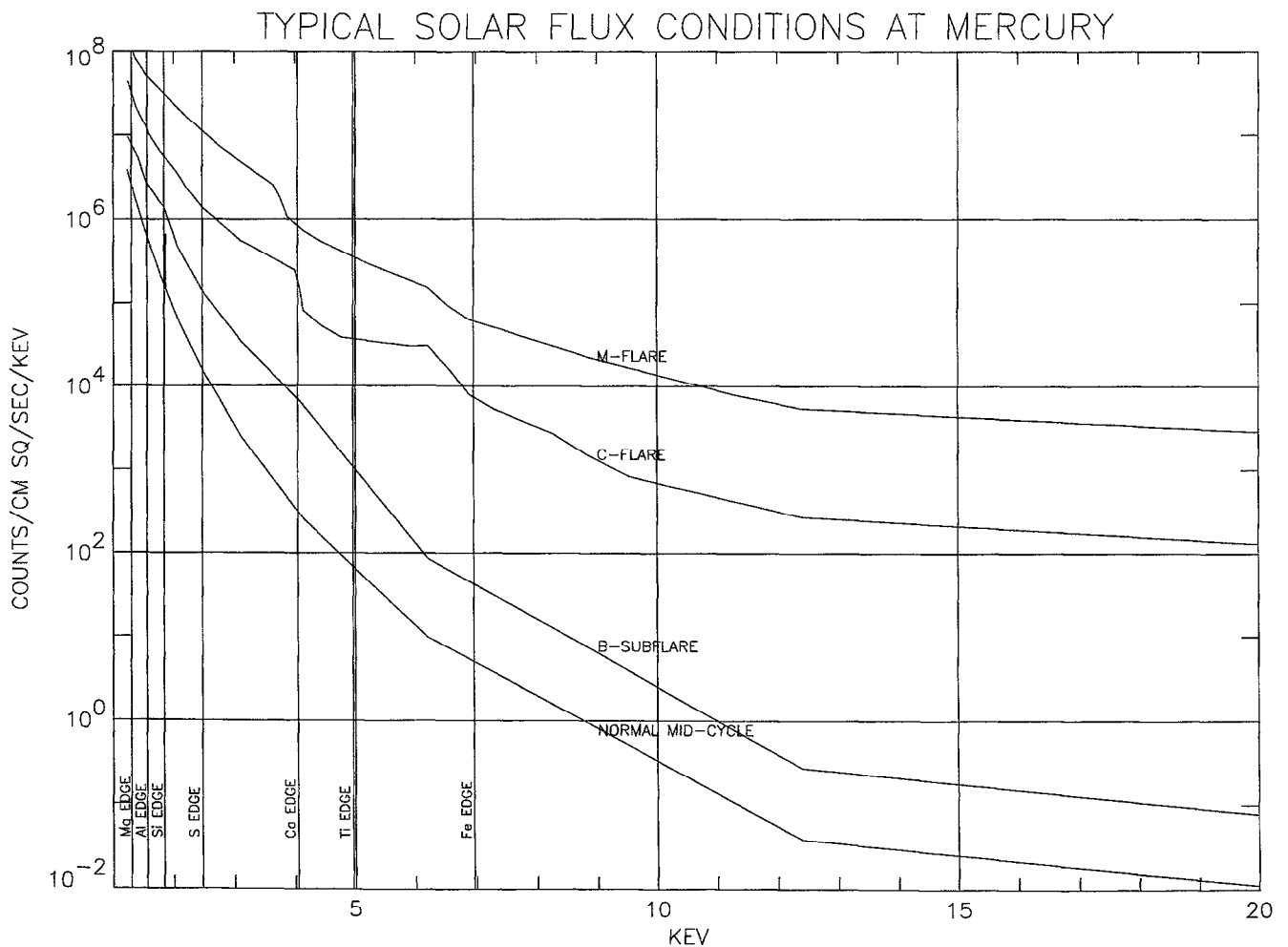


Fig. 2. Range of typical solar spectra at mid-cycle. From highest to lowest average counts s^{-1} these are (1) M1 Flare ($10\text{--}50\text{ yr}^{-1}$), (2) C1 Flare ($50\text{--}500\text{ yr}^{-1}$), (3) B1 Subflare ($> 500\text{ yr}$ to baseline at maximum), (4) A5 Quiescent (baseline at mid-cycle). The absorption edge for each major element, the energy above which solar energy can be absorbed to produce the fluorescent line for that element, is here as well

hence higher resolution maps, especially for the heavier elements such as Fe. Thus, the Sun's output must be monitored whenever surface measurements are made, in order to normalize these surface measurements and thus to obtain quantitative elemental abundance data.

X-ray production at planetary surfaces

We model surface X-ray spectra production to generate theoretical spectra for a variety of targets and to predict the relationship between elemental line intensity and concentration ratios under anticipated solar conditions. Our models take into consideration not only the anticipated solar flux, but the anticipated range of elemental concentrations in the target, as well as relevant cross-section, yield, instrumental, and viewing geometry parameters for both X-ray induced fluorescence and both coherent and incoherent scatter from the surface (Clark, 1979, 1997). This translates into inherently lower integration times to achieve a given sensitivity and thus higher spatial resolution. In this way, we can predict sensitivities, required

integration times, and spatial resolution for a given target and set of mission conditions. Generally, despite a larger background flux at lower energy lines, intensities, and thus sensitivities, will increase for lower energy lines. The results of this modeling for the Mercury Orbiter mission proposed here will be discussed below.

X-ray detector instrumentation

A variety of detectors, the newer ones involving solid state technologies which are under development as remote detectors, can be used to measure X-rays in the 1–10 keV region of interest here (James *et al.*, 1994; Michette and Buckley, 1993). Criteria which have been considered in the selection of X-ray detectors proposed for previous missions, such as the NEAR mission on which we are currently flying X-ray spectrometers, included reliability, cost, and established heritage for space missions. Additional instruments being considered here include, but are not limited to, versions of instruments under development as part of the NASA Facility Instrument Devel-

TIME VARIATION IN SOLAR OUTPUT NEAR SOLAR MAXIMUM

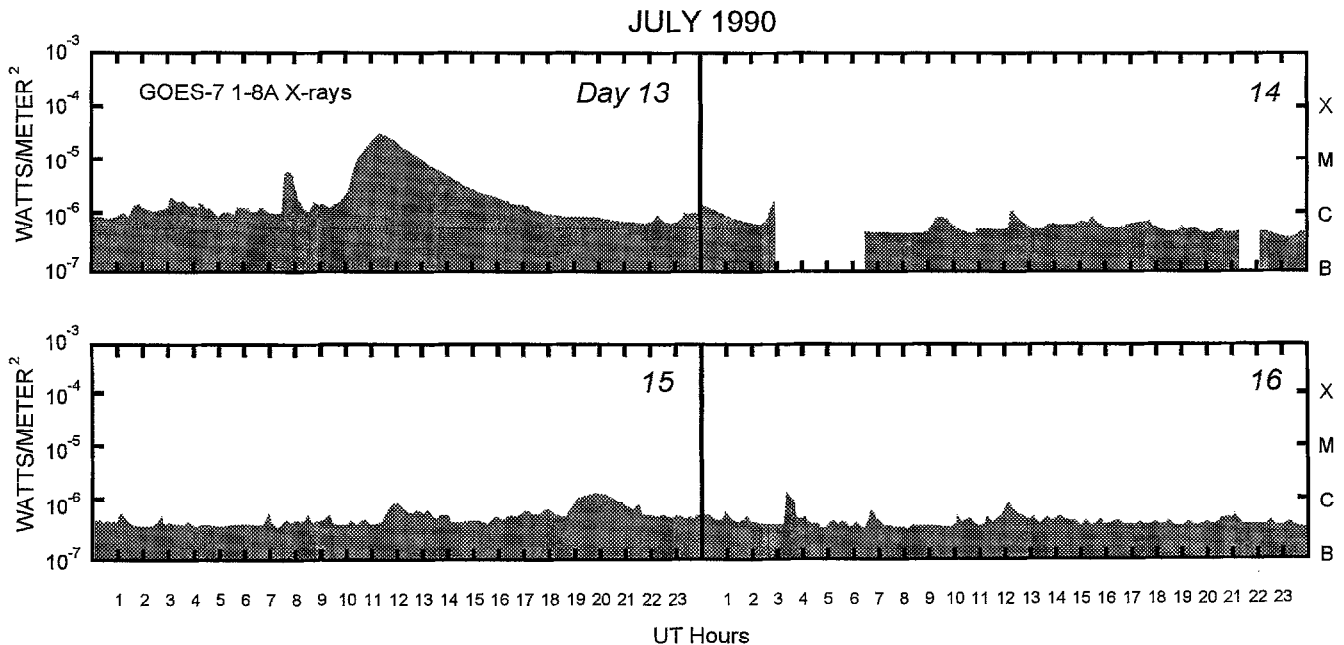


Fig. 3. Minute to minute average solar flux (Solar-Geophysical Data Comprehensive Reports, 1991). Solar variations shown are for May 4 and 14, 1986, just prior to the last solar maximum. Note M Flare and extended rise and fall time typical of large flare on May 4, and repeated occurrences of subflares on May 14

opment Program, and/or presently being flown on the NEAR mission, which was launched on February 17, 1996. Table 1 shows a comparison of the most salient characteristics of detectors which could be considered, including stability, cost, weight, type of heritage, spectral resolution, absorption efficiency, and cooling required. The higher thermal flux environment at Mercury would necessitate selection and design of a detector which could operate at higher temperatures. The X-ray detectors described are the Proportional Counter (PC), High Purity Germanium (HPGe), Lithium Drifted Silicon (Si(Li)), Mercuric Iodide (HgI₂), Cadmium Zinc Telluride (CZT), Silicon Avalanche Photodiode (SiAPD), and Silicon PN (SiPN) detectors.

Considered first will be our “baseline” system, the sealed gas proportional counters (PC) which are currently

being flown on the NASA NEAR mission (Trombka *et al.*, 1997). Potential candidates for a Mercury orbiter X-ray spectrometer will then be compared to the PC detectors which still have the most heritage on planetary flights. Energy resolution on present day sealed gas proportional counters is considerably improved from the time when they were first flown as part of the Apollo program, although they are still unable to resolve cleanly the lower energy Mg, Al, and Si lines which are at 1.25, 1.49, and 1.74 keV, respectively, and thus require a balanced filter system. (These proportional counters have 18% resolution at 5.9 keV at present.) The experiment package consists of a set of three asteroid-pointing proportional counters with 25 cm² windows and differential filtering (one with no filter, one with an Al filter, and one with a Mg filter) to separate Mg, Al, and Si lines. Each detector

Table 1. Comparison of X-ray detector systems

	PC	HPGe	Si(Li)	HgI ₂	CZT	SiAPD	SiPN
Absrptn eff. 1–10 keV	95–40%	99–90%	99–90%	99–90%	99–90%	99%	99%
Energy res. @ 1.25 keV	45%	25%	25%	25%	?	<45%	<45%
Cooling	None	Active	Active	TEC	TEC	TEC	TEC
Stability	Years	w/cool	w/cool	<100°C	?	??	Years
Weight (kg)	5–10	20	20	<5	1–2	1–2	1–2
Power (W)	20	>50	>50	<5	<5	<5	<5

Note: the X-ray detectors described are the Proportional Counter (PC), High Purity Germanium (HPGe), Lithium Drifted Silicon (Si(Li)), Mercuric Iodide (HgI₂), Cadmium Zinc Telluride (CZT), Silicon Avalanche Photodiode (SiAPD), and Silicon PN (SiPN) detectors.

has a thin (1 mil) Be window. This thin Be layer preferentially absorbs the lower energy X-rays. The Be thus prevents the large amount of X-radiation scattered from the surface as a result of the higher solar flux at lower X-ray energies from overwhelming the lower energy fluorescent lines (Mg, Al, and Si) which are generated at the surface, and thus effectively shields these lines. Each detector has a rod with an ^{55}Fe source (which generates a line at 5.9 keV) which is rotated into place for in-flight calibration. Two additional detectors mounted so that the Sun is always in the field of view act as monitors for the Sun, the source of surface-generated X-rays as described above. (The measurements from the solar monitor will be used to normalize surface data for variations in solar output and in solar incidence angle, and thus to obtain absolute elemental abundance data.) One monitor, a proportional counter similar to the asteroid-pointing detectors, has a new feature, a graded shield filter, specially designed to enhance its sensitivity at higher energies where the solar flux is lower. The other monitor is a new solid state detector which just became available, a Silicon PIN detector. Because the solar flux is orders of magnitude more intense than the flux emitted from the planet's surface, only small area (effectively square millimeter) detectors are needed to obtain statistically significant results for the proposed observation times. The package, at 5 kg, is lightweight, and its power requirements, at 20 W, are minimal.

On the other hand, a variety of solid state detectors recently have been developed, including the Silicon PIN, Cadmium Zinc Telluride (CZT), Mercuric Iodide (HgI_2), high purity Germanium (HPGe) and Lithium Drifted Silicon (Si(Li)), as well as Silicon fast avalanche photodiode (APD) detectors. The absorption efficiencies of these detectors are intrinsically higher, the spectral resolution comparable to that of proportional counters at this time. Although Si(Li) and HPGe detectors are capable of operating efficiently in the soft X-ray region, they require cryogenic cooling, and will not be discussed further, because cost, weight, and reliability constraints would rule out this type of detector system. In principle, the other solid state detectors listed operate at room temperature and thus require no active cooling. The big advantage of these detectors (which require only thermal electric cooling, or TEC) is that they are lightweight and have smaller power requirements than proportional counters, and thus are more ideal candidates for smaller, cost-effective missions such as the ESA Mercury mission being discussed here. HgI_2 detectors go through a permanent phase change at higher temperatures, and thus will not be discussed here as candidates for a mission in the high thermal flux environment of Mercury.

Until now, solid state detectors have had no flight qualifications for the long lifetime operation required for a space mission; however, one such detector, a Silicon PIN detector, is being flown and tested as a solar monitor on the NEAR mission. In addition, both CZT and APD detector arrays are about to be flown on NASA's Clark mission in mid-1996. These three detector systems will be compared here, as we consider arrays of these detectors to be top candidates for a Mercury mission. The Si APD is a fast detector which requires less external amplification than other detectors. Although APD detectors appear to

be very sensitive to the environment, and, even after being sealed, may eventually develop degraded performance as a result of exposure to water, they appear to return to their original state after being annealed at 100°C . All solid state detectors have inherently higher and more uniform absorption efficiency in the energy range of interest. We anticipate that spectral resolution will continue to improve. These detectors are manufactured with window areas that are smaller than those for proportional counters, ranging from millimeters to a couple of centimeters across. Currently, these detectors are being flown as linear or two-dimensional arrays. A linear array, differentially filtered, with a total area of a few square centimeters would probably suffice for a nadir-pointing detector at Mercury, where the source flux is an order of magnitude higher than at 1 AU, where a 25 cm^2 , and thus an array of detectors, would be required. A solid state detector with a pinhole window would work well for a solar monitor. As on previous detectors, thin Be filters would be used to cut down on higher flux at lower energies for all detectors. A collimator similar to the ones already flown would also be flown in order to limit the field of view. Weight and power requirements for these solid state detectors would be reduced by a factor of two or more from those requirements for proportional counters. Figure 4 gives diagrammatic views of the detectors described above and compared in Table 4.

Analysis of X-ray spectra

A procedure similar to the one used for reduction of the Apollo and NEAR mission XRF data would be used for the X-ray data. (For a detailed discussion of X-ray data reduction and analysis, see Clark (1979) or Yin *et al.* (1993).) The steps of this process most relevant to a Mercury orbiter mission will be outlined below.

Step 1: Pulse height analysis. In these detectors, each photon detected generates a pulse, the amplitude, or height, of which depends on the energy of the photon. The first step in processing detector output is the conversion of pulse height spectra into energy spectra.

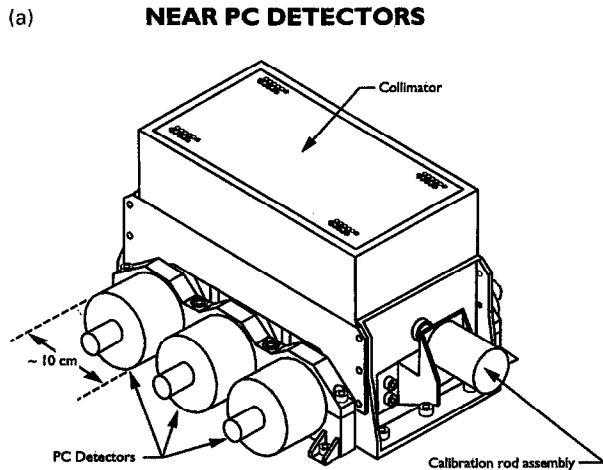
Step 2: Instrumental corrections for each detector. Spectra from each detector would be normalized for gain and drift as necessary from results obtained during in-flight calibration. Background determined from unilluminated hemisphere, a background which results from coherent scattering of sky X-ray sources from the surface and in our experience is fairly constant, would be subtracted.

Step 3: Simultaneous solar and surface flux measurement and normalization for solar variation. The solar flux will be an order of magnitude more intense at Mercury than at the Earth, and the mission will most likely be flown during a part of the solar cycle when the Sun's output is relatively high. Using simultaneously obtained solar monitor data, each characteristic line intensity determined from the nadir-pointing detectors would be normalized to typical solar output as seen in the solar monitor.

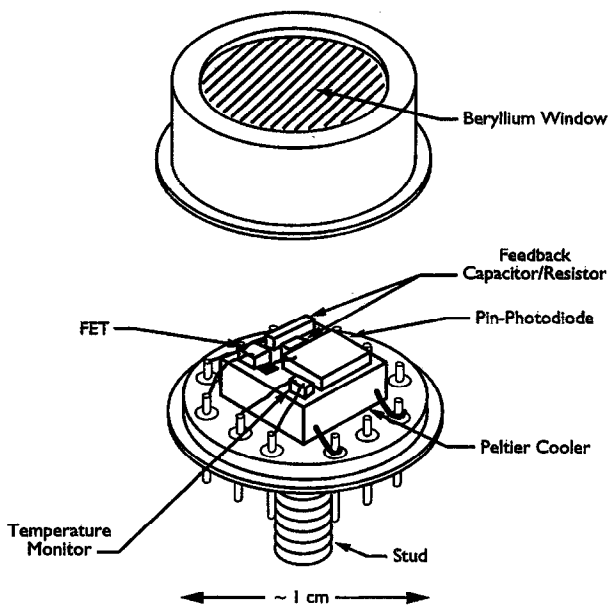
Step 4: Normalization surface measurements for pointing geometry. Line intensities would be further nor-

Table 2. Major element abundances in a range of lunar soils

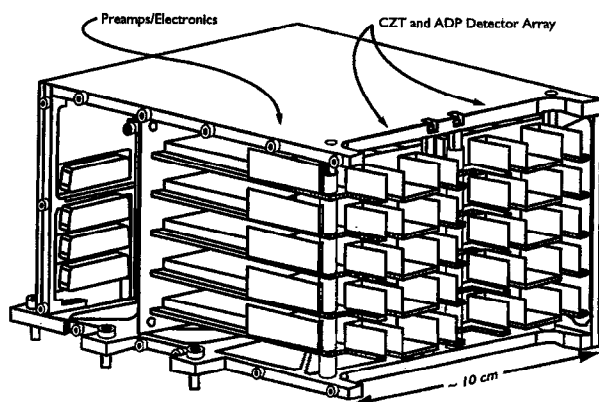
Element	Apollo 12 basalts (%)	Apollo 15 KREEP-rich basalts (%)	Apollo 16 highlands (%)
Fe	12.00	9.00	4.30
Ti	1.60	1.00	0.40
Ca	7.50	8.30	11.10
Si	21.60	21.80	21.00
Al	7.10	9.10	14.10
Mg	5.90	6.30	3.60



(b) **NEAR Si PIN SOLAR MONITOR**



(c) **CLARK CZT AND ADP DETECTOR ARRAYS**



malized according to viewing considerations: altitude variation, spacecraft pointing, and incident solar flux angle.

Step 5: Sum measurements to achieve acceptable signal/noise. Measurements would be summed in overlapping areas of coverage. The amount of summing necessary would depend on integration times required to achieve an acceptable level of accuracy. The resulting spatial resolution will depend on solar output and pointing geometries.

Step 6: Intensity ratioing and elemental abundance maps. Elemental line intensities would be ratioed to Si or other element line intensity to remove matrix effects, where variations in absorption cross-sections vary as a result of gross physical variations in the regolith. Finally, intensity ratios would be converted to elemental concentrations and mapped for Mg, Al, Si, Ca, Fe, and possibly Ti, and S.

Results anticipated from XRS experiment

Calculations of anticipated results have been done for a variety of orbital and instrument configurations, and a range of lunar compositions: anorthositic gabbro bearing soils from lunar highlands (Apollo 16), KREEP-bearing soils (Apollo 15), and more typical mare basalt bearing soils (Apollo 12). Based on albedo and spectral reflectance measurements, Mercury surface soils are likely to fall somewhere in between highland and mare in composition. Table 2 above shows the major element abundances for these compositions.

Modeling of anticipated spectra is essential not only in anticipating our results and planning accordingly, but in the determination of the quantitative relationship between X-ray line intensities, and surface concentrations. Only when this relationship is quantitatively established can absolute elemental concentrations be derived from instru-

Fig. 4. Comparison of X-ray detector systems. The proportional counter system (a) includes three differentially filtered detectors pointed toward nadir, and one similar detector oriented 180° from nadir-pointing detectors acting as a solar monitor. These detectors could be replaced with Silicon PIN detectors (b) shown, or arrays of CdZnTe or APD detectors (c), as shown. All would require a collimator, necessary to limit the field of view on nadir-pointing detectors, which has a honeycomb-like structure and is similar to the one shown for the proportional counter, as well as Be windows

mental measurements. Calculations of expected X-ray emissions from Mercury require modeling the solar spectrum for a range of levels of solar activity weighted for their probabilities of occurrence. In the case of the Mercury mission proposed here, mid-cycle conditions are conservatively anticipated, although if launch is actually in 2011, conditions may be more akin to those at solar maximum, which should occur in approximately 2010. Figure 5a and b show two theoretically modeled X-ray spectra for two lunar regolith compositions considered most analogous for Mercury, Apollo 15 (mixed basalt), and Apollo 16 (basalt/highland mix), as shown above.

The integration time required to achieve 10 and 20% certainty (also defined as sensitivity) on a spectral measurement at a particular altitude (200 km) above Mercury, with the anticipated 5° field of view and 5 cm² detector window are calculated as shown in Table 3. It is also assumed that the instrument is nadir-pointing and at a typical solar incidence angle of 45° (halfway between the subsolar point and the terminator). (Sensitivity is defined here as signal plus background divided by the signal squared and then by the sensitivity squared, where the signal is the fluorescence of the K-alpha line and the background is largely coherent scatter.) As shown below, smaller integration times will be required to achieve these levels of sensitivity during times of even modest flare activity. This is particularly true for the elements (marked with an asterisk) with lines at higher energies where the solar flux is markedly decreased.

Table 4 shows spatial resolution which could be achieved with the required integration times, for the particular orbital trajectory anticipated for the ESA Mercury mission proposed here. The assumptions are made (a) that the spacecraft is spinning at about 10 rev min⁻¹; (b) that the effective ground speed is 3 km s⁻¹ at 200 km periapsis; (c) that this will be a two Earth year mission, translating to about 15 encounters per minimum footprint size, or swath, the minimum footprint size being about 100 km (an effective 30° field of view, with instrument accumulating spectra during about half a second during the planet-pointing part of the spin) by 20 km (due to the minimum field of view plus speed in the non-spin direction) at 200 km altitude. The results for Ti and Fe assume flare conditions during one of those encounters. Longer integration times, and thus larger footprints, are associated with higher energy line elements Fe and Ti. As Table 4 indicates, for the mission being considered here we calculate that, within 10–20° of periapsis, resolutions of 50–100 km are achievable for Mg, Al, Si, and Ca, and 200–650 km for Fe and Ti with a 200 km periapsis two year mission. Spatial resolutions would decrease markedly at greater distances from periapsis. (Spatial resolutions in Table 4 should be multiplied by a factor of 2.5 to approximate 500 km altitude resolution.)

Interpretation of results from XRS experiment

Our current knowledge of Mercury is based almost exclusively on the data received from the Mariner 10 mission on its three flybys of Mercury in 1974–75. This mission, although providing important information on the physical

nature of Mercury's surface and interior, provided no direct information on the inner planet's composition. Mariner 10 color difference data and Earth-based spectroscopic measurements, although they do indicate relative depletion of surface Fe and Ti relative to the Moon, are of poor quality and contradictory in nature. An X-ray and gamma-ray spectrometer package included on a future Mercury orbiter could measure the abundances of Na, Mg, Al, Si, Ca, Ti, Fe, K, and Th at varying resolutions. Such measurements of elemental composition would provide crucial constraints on evolutionary models of Mercury and lead to better understanding of the history of the inner solar system.

Composition maps and the nature of Mercury's surface and interior

Data from the XRF instrument would be used to accomplish a most important mission goal: the geochemical mapping of the regolith, which will provide important constraints on the composition of the crust, mantle, and core, and thus on models for Mercury's history. Differences between Fe data, derived from XRF (measurements down to <1 mm) and GRS (measurements down to tens of cm) experiments should be due to differences in near-surface stratigraphy, and could put constraints on the extent and nature of regolith formation.

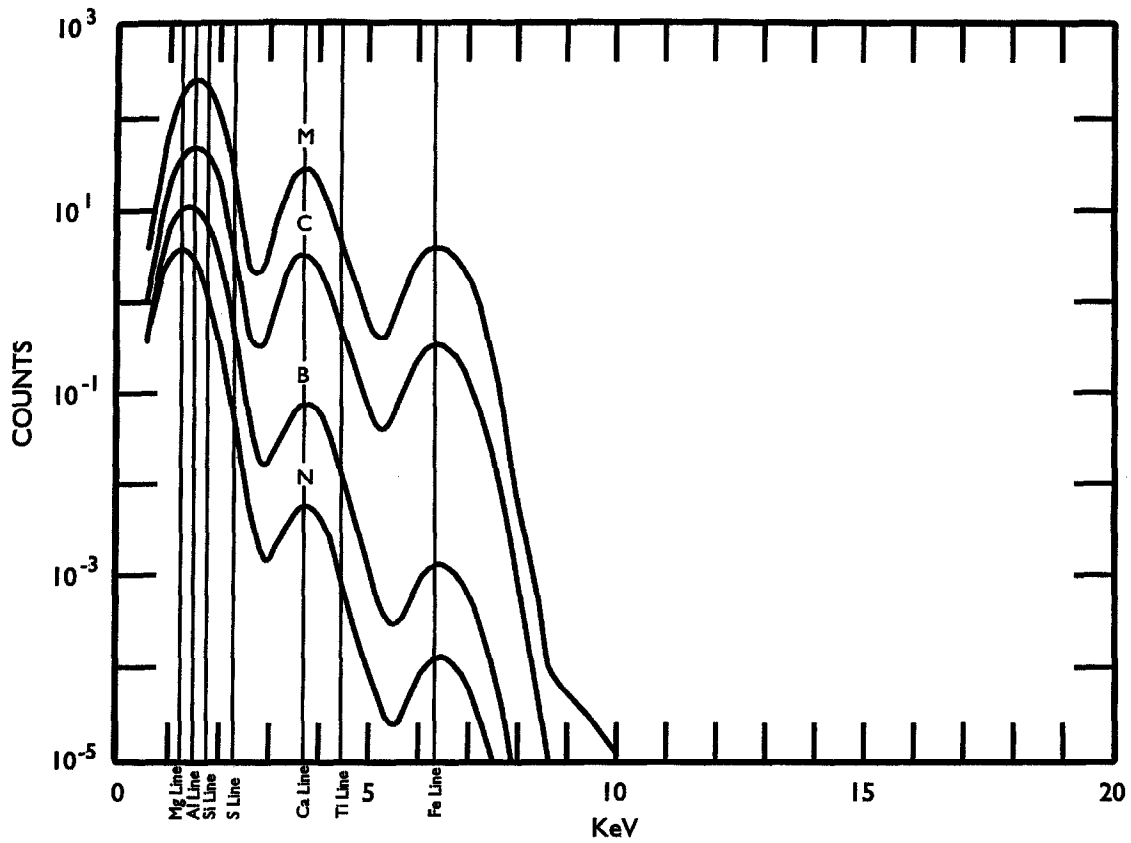
Geochemical terrains and the nature of geochemical differentiation

Element abundance maps would show the extent of surface heterogeneity on the scale of tens of km or more. These maps would indicate whether the three major terrains (intercrater plains, smooth plains, and highlands) have the distinct geochemical signatures that color difference data have implied are lacking. The nature of compositional variations within and between these terrains, along with geochemical differences associated with vertical stratigraphy at impact features, will provide constraints on models for geochemical differentiation, and allow comparisons to other terrestrial planet analogs for these terrains. Does the most extensive terrain, the intercrater plains indicate the presence of a magma ocean comparable to the one proposed for the Moon? The nature of surface heterogeneities could be further characterized by correlation of compositional data with observations, such as magnetic, gravity, or radar ranging data.

Evolution of Mercury and the inner solar system

A variety of models (selective accretion (Weidenschilling, 1978), post-accretion vaporization (Cameron *et al.*, 1988), and giant impact (Wetherill, 1988)) have been proposed to explain the discrepancy between the composition for Mercury indicated by its observed high density, and the composition predicted by equilibrium condensation from the solar nebula (Lewis, 1972). The three models predict different overall compositions; the XRS experiment could

MERCURY PC DETECTORS, APOLLO 15 COMP, 60 SECONDS WITH SPIN



MERCURY PC DETECTORS, APOLLO 16 COMP, 60 SECONDS WITH SPIN

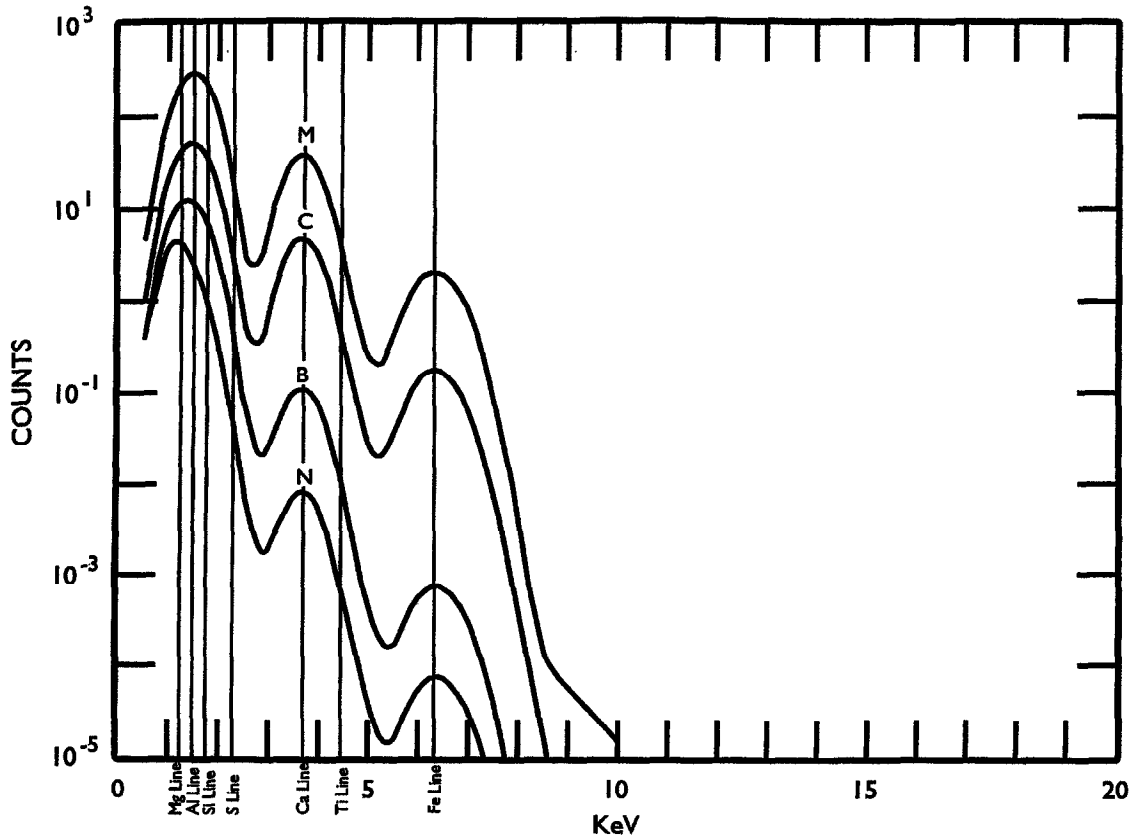


Fig. 5. Theoretical X-ray spectra for Mercury. These two spectra are modeled as discussed in the text for two possible compositions, based on Apollo 15 (mixed basalt) (a) and Apollo 16 (mixed basalt and highland) (b) soils on the Moon

Table 3. Mercury mission integration times required to achieve 10 and 20% sensitivity for major element compositions

Element		Apollo 16 ave soil typical/low flare	Apollo 15 ave soil typical/low flare	Apollo 12 ave soil typical/low flare
Fe*	10%	2.5 h/1.5 min	1.0 h/0.8 min	0.5 h/0.4 min
	20%	0.6 h/0.4 min	0.3 h/0.2 min	0.1 h/0.1 min
Ti*	10%	4.0 h/8.5 min	1.5 h/3.5 min	0.4 h/1.0 min
	20%	1.0 h/2.0 min	0.4 h/0.9 min	0.1 h/0.3 min
Ca	10%	4.0 min	6.0 min	6.0 min
	20%	1.0 min	1.5 min	1.5 min
Si	10%	0.4 min	0.4 min	0.4 min
	20%	0.1 min	0.1 min	0.1 min
Al	10%	0.6 min	1.5 min	2.0 min
	20%	0.2 min	0.4 min	0.5 min
Mg	10%	6.0 min	4.0 min	4.0 min
	20%	1.5 min	1.0 min	1.0 min

Table 4. Mercury mission estimated spatial resolutions (km) for major elements at 20% sensitivity and 200 km altitude

Element	Apollo 16	Apollo 15	Apollo 12
Fe	500	350	200
Ti	650	400	200
Ca	85	100	100
Si	50	50	50
Al	50	60	60
Mg	100	85	85

distinguish between them. Apparently, Mercury has a complex and intense early tectonic history, which involves tidal despinning followed by crustal compression, along with early impact bombardment. Mercury has extensive curvilinear rays, for which no lunar analogs exist. Geochemical characterization of these tectonic features would show their relationship to major terrains formation, and provide constraints on their chronology and extent.

Acknowledgements. We would like to thank Richard Starr for his input and support through his role as Principal Investigator for a solid state X-ray detector experiment on the Clark SSTI mission. Richard Starr, Paul Lowman, Larry Evans, Keith Gendreau, Sam Floyd, and Mike Harrison provided substantive discussions. This work was supported by a NASA Contractual Agreement with Catholic University.

References

- Adler, I. and Trombka, J. (1970) *Geochemical Exploration of the Moon and Planets*. Springer, New York.
- Adler, I., Gerard, J., Trombka, J., Lowman, P., Blodgett, H., Yin, L., Eller, E. and Lamothe, R. (1972) The Apollo 15 X-ray fluorescence experiment. *Proc. Lunar Sci. Conf. Third 3*, 2157–2178.
- Belcher, J., Slavin, J., Armstrong, T., Farquhar, R., Akasofu, S., Baker, D., Cattell, C., Cheng, A., Chupp, E., Clark, P., Davies, M., Hones, E., Kuth, W., Maezawa, J., Mariani, F., Marsch, E., Parks, G., Shelley, E., Siscoe, G., Smith, E., Strom, R., Trombka, J., Williams, D. and Yen, C. (1991)

- Mercury Orbiter: Report of the Science Working Team, NASA TM 4255.
- Cameron, A., Fegley, B., Benz, W. and Slattery, W. (1988) The strange density of Mercury: theoretical considerations. In *Mercury*, pp. 692–708. University of Arizona Press, Tucson.
- Clark, P. (1979) Comparison of theoretically calculated and observed XRF data. In *Correction, Correlation, and Theoretical Consideration of Lunar X-ray Fluorescence Intensity Ratios*, Chap. 6. University of Maryland Dissertation.
- Clark, P. (1997) X-ray fluorescence from planetary surfaces: modeling, data analysis, and future missions, NASA TM (in press).
- Clark, P. and Adler, I. (1978) Utilization of independent solar flux measurements to eliminate nongeochemical variation in X-ray fluorescence data. *Proc. Lunar Planet. Sci. Conf. Ninth 3*, 3029–3036.
- Clark, P. and Hawke, R. (1981) Compositional variation in the Hadley Apennine Region. *Proc. Lunar Planet. Sci. Conf. 12B*, 727–749.
- Crosby, N., Aschwanden, M. and Dennis, B. (1996) Frequency distribution and correlations of solar X-ray flare parameters. *Solar Phys.* (in press).
- James, R., Schlesinger, T., Siffert, P. and Franks, L. (1994) Semiconductors for room-temperature radiation detector applications. In *Materials Research Society Symposium Proceedings*, Vol. 302, Parts I–III, VI–VII, pp. 1–2.
- Lewis, J. (1972) Metal/silicate fractionation in the solar system. *Earth Planet. Sci. Lett.* **15**, 286–290.
- Michette, A. and Buckley, C. (1993) X-ray detectors. In *X-ray Science and Technology*, pp. 207–253.
- Solar-Geophysical Data Comprehensive Reports (1991) #557, Part II. Data for July, 1990. National Geophysical Data Center, Boulder, Colorado, January.
- Trombka, J., Boynton, W., Bruckner, J., Squyres, S., Clark, P., Evans, L., Floyd, S., Starr, R., Gold, R., Goldsten, J. and McNutt, R. (1997) The NEAR X-ray/Gamma-ray Spectrometer. *J. Geophys. Res.* (in press).
- Weidenschilling, S. (1978) Iron/silicate fractionation and the origin of Mercury. *Icarus* **35**, 99–111.
- Wetherill, G. (1988) Accumulation of Mercury from planetesimals. In *Mercury*, pp. 670–691. University of Arizona Press, Tucson.
- Yin, L., Trombka, J., Adler, I. and Bielefeld, M. (1993) Remote X-ray spectrometry. *Remote Geochemical Analysis: Elemental and Mineralogical Composition*, pp. 167–198.
- Zombeck, M. (1990) The solar spectrum (from Malitson, NSSDC). In *Handbook of Space Astronomy and Astrophysics*. Cambridge University Press, London.